

THE UCLA

Undergraduate Science Journal

VOLUME 37 | SPRING 2024



2023-2024 USJ STAFF

Editors-in-Chief

Elise Tran Emily Lin

Logistics Coordinator

Ahmad Ismail

Faculty Advisor

Jorge A. Avila, PhD

Managing Editor of Review

Caroline Sha

Asst. Managing Editors of Review

Jordan Lin	Nyah Zhang
Malvika Iyer	Rachel Ma
Melody Jiang	Raphael Low

Managing Editor of Editorial

Sohan Talluri

Asst. Managing Editors of Editorial

Brendan Sam	Nhi Pham
Isabel Angres	Timothy Liu
Ying yin (Lina) Zhu	

Managing Editor of Layout

Dashrit Pandher

Asst. Managing Editor of Layout

Chelsea Lai

Review Board

Agamroop Kaur
Archi Patel
Caden Chow
Cecilia McCormick
Daniel Bielin
David Mastro
Eliana Bohn
Ethan Hung
Isaac Ramos Reina
Jessica Goeij
Joanna Rhim
Joyce Goh
Mahek Shah
Marissa Li
Miki Matsuoka
Nathan Joshua
Oliver Wang
Raina Bandekar
Ryan Wong

Saanika Joshi
Sai Charan Petchetti
Summer Kelso
Viraj Nigam
Wasila Sun
Yiming Li
Zoe Yeh

Editorial Board

Andrew Wang
Aniket Das
Brynn Beatty
Chahak Gupta
Charlotte Chen
Chloe Nelson-Torakawa
Derek Ren
Kyle Nguyen-Ngo
Lee Zucker-Murray
Marie Yang
Lily Zello

Gia Boisselier
Paul Zhang
Ruthy Shin
Satviki Chaturvedi
Siddhika Naik
Tanisha Lakhanpal
Vivasvaan Aditya Raj
Zachary Lamm

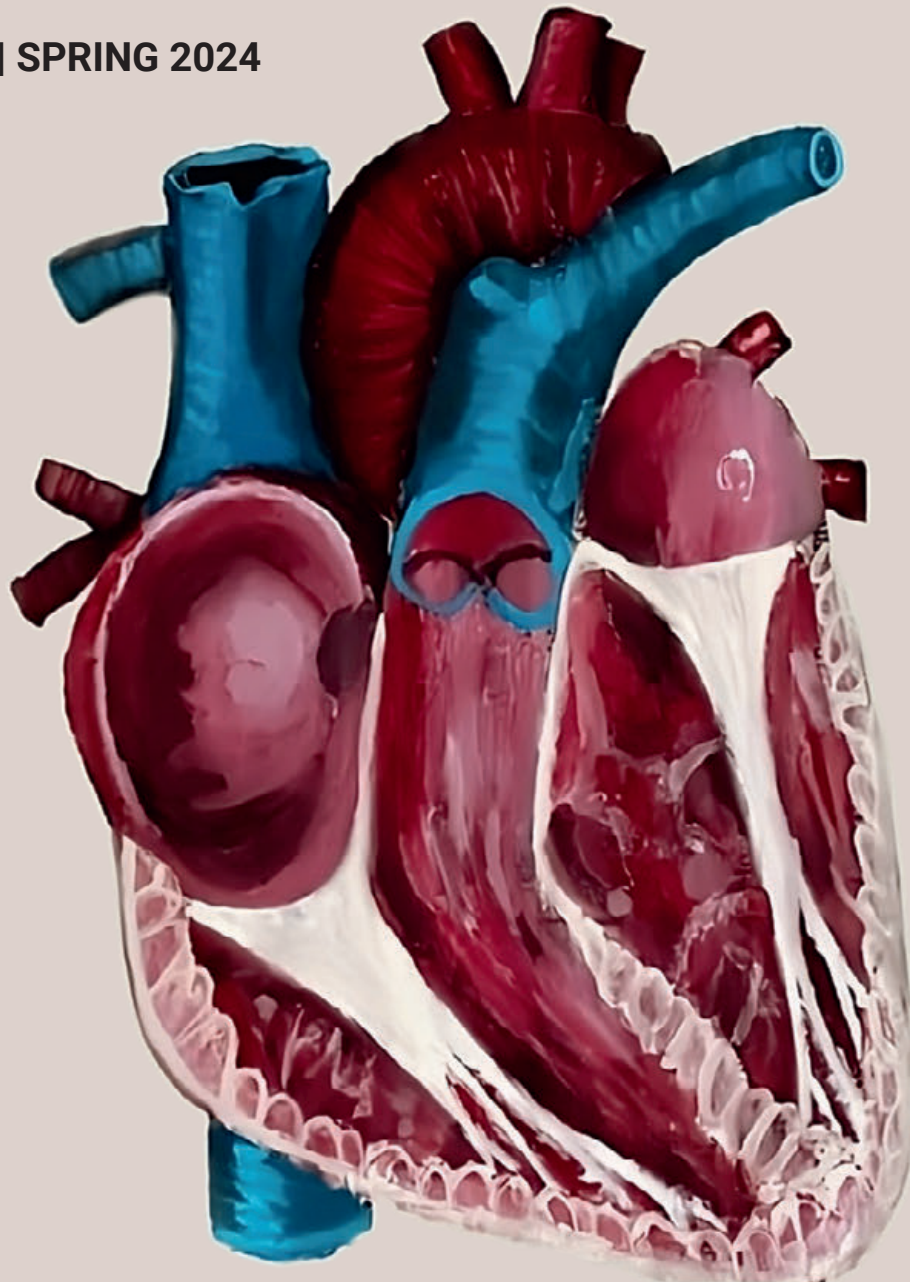
Layout Board

Christy Ma
Danny Zhu
Truman Ma
Zenya Bian



THE UCLA Undergraduate Science Journal

VOLUME 37 | SPRING 2024



Established 1986.

The UCLA Undergraduate Science Journal is an officially recognized student organization at UCLA.
The UCLA Undergraduate Science Journal is entirely managed and produced by students.
Its contributions are the original work of UCLA undergraduates.

FRONT COVER ILLUSTRATION BY CHRISTY MA
INSIDE COVER ILLUSTRATION BY FATIMAH ISMAIL

A Letter from the Editors

Dear Reader,

We are incredibly proud to present to you the 37th Volume of the UCLA Undergraduate Science Journal (USJ). The entirety of this volume is the direct result of undergraduate student effort, from the outstanding manuscripts to the peer review, editing, and layout of the journal. We are truly impressed with the caliber of research conducted by this year's undergraduate authors, as well as the tireless diligence and dedication of the staff members in our Review, Editorial, and Layout Boards. This volume of the USJ includes original research articles ranging from studying dopamine signaling in skin-penetrating parasites to determining how low a spacecraft can reliably fly in Uranus's atmosphere. The articles featured in this journal may only offer a small glimpse into the breadth of research that undergraduates undertake at UCLA, but they are a true representation of the ingenuity and tenacity of our students. We are honored to be a part of this scientific collaboration and we are confident you will see these values exemplified in this year's volume of the USJ.

As Editors-in-Chief (EICs) for the second year in a row, we couldn't be more proud of the growth of USJ throughout our time here. One hallmark of our tenure is the improved coordination between boards. In previous years, Managing Editors (MEs) communicated with their respective boards and reported to the EICs, but did not often directly work with other MEs. Last year, our dual role as MEs and EICs allowed for greater insight into the significance of communication across boards to publish a cohesive and timely journal. As we embarked on our second year as EICs while welcoming a new team of MEs, we made it a priority to ensure consistent and clear communication between our Review, Editorial, and Layout Boards. Rather than three separate boards linked only by the EICs, we learned how to function as a unit throughout the year.

Another major change that we implemented this year was revamping our USJ seminar structure. Every year, USJ staff enroll in a 2.0 unit seminar to learn the reviewing, editing, and layout skills necessary for their role in USJ, as well as to gain insight into the USJ's publication process outside of their board. This year, the leadership team overhauled the course materials and created a new curriculum that was interactive, student-led, and better aligned with the seminar's goals. Our new curriculum allows all members to not only learn about each step of the USJ publication process, but to experience each step for themselves as they craft their Newsbeats, several of which are featured in the USJ. We hope this experience inspires

future leadership teams to not be afraid to effect change for the betterment of both the staff and journal.

As part of the training curriculum for USJ, we also reference a volume of the USJ published over fifteen years ago, which includes staff-written interview articles highlighting UCLA faculty members' journeys and experiences as senior researchers. This year's leadership team was inspired by these articles and wanted to bring them back in the 37th volume of the USJ to specifically feature the research and experiences of the authors and advisors whose research is featured in the journal. These interviews highlight their stories, advice, and understanding of their scientific field to further contextualize their published research, offer insights into the undergraduate research environment at UCLA, and encourage undergraduate students to take advantage of the exciting research opportunities that UCLA has to offer.

This journal would not be possible without the labor and love of our entire team. We would like to especially commend the passion and dedication of all of our USJ staff members who worked with us to make the journal what it is. A huge thank you goes to our MEs, assistant managing editors, and logistics coordinator for the amazing work and long hours you have all dedicated to the USJ. Of course, we would like to express our most heartfelt gratitude to our faculty advisor, Dr. Jorge Avila, who supported us throughout the entire publication process and without whom the USJ would not exist. Dr. Avila has been extremely supportive and encouraging of our new ideas to improve USJ, including completely reworking our class plans. Additionally, we sincerely thank Dr. Tama Hasson, director of the Undergraduate Research Center – Sciences, who provides pivotal support to publish our journal, and the UCLA Clinical and Translational Science Institute for their generous continued support of our annual journal. Finally, we would like to thank ColorNet Press for helping us produce this beautiful journal.

We hope you are inspired while reading about the science featured in this journal, in fields that touch many aspects of our daily lives. This journal stands as a testament to the sheer courage and determination of our UCLA journal staff and undergraduate authors—we could not be more honored to share it with you.

Warm regards,
Elise Tran and Emily Lin



TABLE OF CONTENTS

06 Newsbeats
USJ Staff

INTERVIEW

- 11** Integrating the Past for a Sustainable Tomorrow: The Revolutionary Approach to HIV Treatment with CAR-NK Cells
Charlotte Chen, Isabel Angres, Chahak Gupta, Ahmad Ismail, Emily Lin, Sohan Talluri
- 14** Bringing Gene Therapy to the Public: Increasing Treatment Accessibility and Science Literacy
Ahmad Ismail, Emily Lin, Caden Chow, Chloe Nelson, Lee Zucker-Murray
- 18** Advancements in Skeletal Dysplasia Research: From Genomic Discoveries to Clinical Solutions
Agamroop Kaur, Ahmad Ismail, Emily Lin, Derek Ren, Joanna Rhim
- 20** New Lab? No Problem. An Undergraduate's Journey Towards Finding Her Place In Academia
Elise Tran, Daniel Bielin, Emily Lin, Raphael Low, Siddhika Naik, Vivasvaan Aditya Raj

RESEARCH

- 23** Optimizing Ionizable Lipids in Nanoparticles for Human Bronchial Epithelial Cells
Alicia J. Sanoyca
- 30** Production and Growth of CAR-NK Cells to Treat HIV Infection 
Vincent Le
- 36** Identification of Gender-Based Cyberbullying Tweets with Machine Learning
Shriya Char
- 47** The Effect of a *Trpv4* Mutation on Skeletal Development in Mice 
Derick Diaz
- 57** How Low Can The Uranus Flagship Fly?
Shaya Naimi
- 62** Neural Lineage Reconstruction to Study Neural Networks in *Drosophila* 
Jessica Goeij
- 68** Dopamine Signaling Mediates Skin Penetration by *Strongyloides stercoralis* 
Aracely Garcia Romero

Schooling Guppies Shed Light on Evolution of Social Behavior

Oliver Wang

A key insight into the evolution of social behavior may be hiding in plain sight. While people have long recognized that other animal species form communities, not much is known about the neural and genetic processes that cause this behavior. Researchers sought to identify how sociability is inherited, if at all. To do so, schools of guppy fish were raised and each individual's tendency to stick with the school was measured. Subsequently, the most social fish were bred together for three generations. By the end of the experiment, the most recent generation of fish were found to be more social than their ancestors. Interestingly, researchers also discovered mutations in genes controlling neuron migration in these fish. These findings suggest that those specific genes can be identified as key factors for inheriting sociability, shedding light on the evolution of social behaviors in nature.



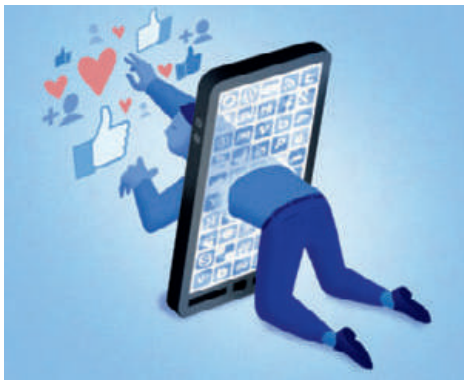
Image: Guppies and other fish species socialize in a hobby aquarium.

Reference: A. Corral-Lopez et al., Functional convergence of genomic and transcriptomic architecture underlies schooling behaviour in a live-bearing fish. *Nat. Ecol. Evol.* **8**, 98–110 (2024). doi: 10.1038/s41559-023-02249-9

Image Source: Photo taken by Selina Lu.

Do My Facebook Friends Really Know Me?

Rachel Ma



According to a recent study, the answer is likely yes. Qi Wang, the Director of the Culture & Cognition Lab at Cornell, exposes the dynamic process of constructing one's digital identity by comparing the self perception of authors with audience's perceptions after viewing Facebook status updates. Large discrepancies were found between these two groups, where the audience generally rated authors as possessing lower self-esteem and higher in being self-revealing than authors' self-perceptions. Moreover, the inclusion of photos and videos enhanced the accuracy of audience assessments. Notably, cultural norms subtly influence perceptions, reflecting offline attitudes regarding gender and ethnicity even when these identities were masked. This investigation underscores how divergent online perceptions due to social media could undermine our social lives and well-being, urging further exploration into the "outsourced meaning-making process" on other social media platforms to ultimately shape the design of interfaces for authentic self-expression.

Image: Chasing positive perceptions online seems to only make our connections less genuine.

Reference: Q. Wang, A. Khuu, M. Jivotovski, The self online: When meaning-making is outsourced to the cyber audience. *PLOS ONE* **18**, e0294990 (2023). doi: 10.1371/journal.pone.0294990

Image Source: Sean David Williams - <https://insights.som.yale.edu/insights/social-media-is-addictive-do-regulators-need-to-step-in>. Licensed under the Creative Commons Attribution.

Can Pregnancy Induce Brain Growth?

Malvika Iyer

The brain and the body have long been studied as separate entities, but recent research has sought to find the connections between these complex systems. A recent longitudinal study showed striking morphological changes in the cortex of pregnant and postpartum women in comparison to their non-pregnant counterparts. These changes, which included increased cortical volume, thickness, and surface area from late pregnancy to early postpartum, were exacerbated in mothers who underwent scheduled C-sections. This study also showed evidence of the effect of immune responses and endocrine cascades on the pregnant person's brain. Overall, these findings suggest that labor may induce neuroplasticity, shedding light on the physiological changes that accompany pregnancy. Studies like these aim to better understand the neurological landscape of pregnancy to provide more support and improved outcomes for pregnant individuals.

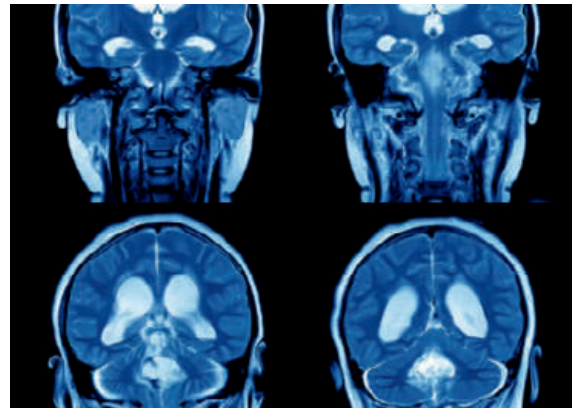


Image: Brain scans that show neuroplasticity of different regions, an ability crucial to how we develop.

Reference: M. Paternina-Die et al., Women's neuroplasticity during gestation, childbirth and postpartum. *Nat. Neurosci.* **27**, 319–327 (2024). doi: 10.1038/s41593-023-01513-2

Image Source: "The malleable brain." www.shutterstock.com

Leaping Into 3D: Efficiently Constructing 3D Scenes From 2D Images

Kuan Heng (Jordan) Lin

Since their invention, photos have captured our precious memories. However, what if with just a few photos, we can reconstruct the scene in 3D to re-experience those memories? For years, though these 3D scene reconstructions were of high quality, they were computationally expensive and time intensive. To address this problem, researchers proposed 3D Gaussian Splatting, a machine learning-based rendering framework that “splats” the scene with rough, sparse points and probabilistically “blurs” them to create mathematical objects called Gaussians that create the perception of detail. Now, with a few images, we can reconstruct the scene they capture in 3D and—for the first time—render it in real-time. This research provides artists and engineers a computationally inexpensive tool to work in 3D, with applications ranging from video game development to scientific records, and even recent augmented reality technologies. More than ever, 3D computing is redefining the way we capture the world around us.

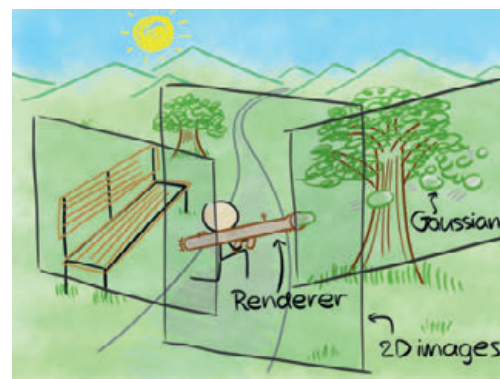


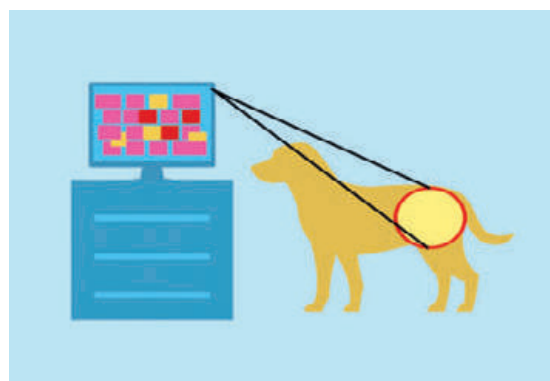
Image: Artistic rendition of splatting the scene with 3D Gaussians from 2D images.

Reference: B. Kerbl, G. Kopanas, T. Leimkühler, G. Drettakis, 3D Gaussian Splatting for Real-Time Radiance Field Rendering. *ACM Trans. Graph.* **42**, 1–14 (2023). doi: 10.1145/3592433

Image Source: Digital illustration by Jordan Lin.

AI as a Tool for Veterinarians: Detecting Tumor Necrosis in Canines

Gia Boisselier



Numerous studies have evaluated the use of artificial intelligence within the field of human oncology, but what about our furry friends? Present day veterinary medicine relies on grading soft-tissue sarcomas (STS) to predict tumor behavior in canine skin and connective tissues. Veterinary pathologists assess STSs manually, integrating scores from mitotic count, tumor necrosis percentage, and cellular differentiation—a procedure that, while thorough, is slow and susceptible to inconsistencies. In a recent study, researchers utilized machine-learning algorithms to identify tumor necrosis in digitized canine STS slides. Annotated necrosis regions were analyzed by a convolutional neural network in phases of training, testing, and validation. Ultimately, the study culminated in a validation accuracy of 92.7% in necrosis detection, suggesting a future where machine-learning can be used as a diagnostic tool for more accurate and efficient tumor grading in our beloved dogs.

Image: A slide-level confusion map indicates areas of necrosis within a sample of canine STS.

Reference: A. Morisi et al., Detection of Necrosis in Digitised Whole-Slide Images for Better Grading of Canine Soft-Tissue Sarcomas Using Machine-Learning. *Vet. Sci.* **10**, 45 (2023). doi: 10.3390/vetsci10010045

Image Source: Nam, S. et al. Active tissue adhesive activates mechanosensors and prevents muscle atrophy. Figure 1. Used with permission from author.

Climate Changes Coastal Communities

Ryan Wong

While carbon emissions continue to exacerbate global warming and threaten our way of life, in other parts of the world, our photosynthesizing friends are feasting on the abundance of carbon. Known as the CO₂ fertilization effect, rising carbon levels have increased photosynthesis around the world, contributing to longer growing seasons. However, recent research suggests that mangrove forests, which are complex intertidal ecosystems, may deviate from this trend. Mangrove forests are highly adapted ecosystems that provide a community for a myriad of species. But because they are so specialized they are also highly sensitive to changes in their environment, including drought and rising sea levels. Still, mangrove forests are highly efficient at sequestering carbon dioxide from the atmosphere, which may be why scientists have observed a greater CO₂ fertilization effect on mangroves than terrestrial forests. They may be the key to stalling climate change.

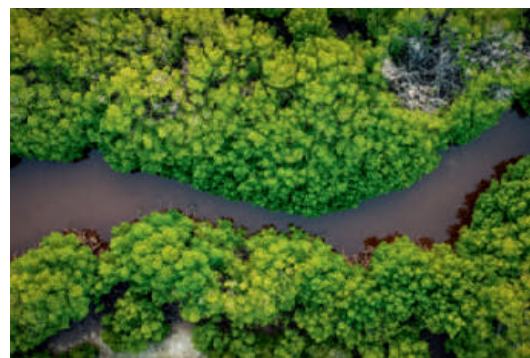


Image: Mangrove forests are complex ecosystems adapted to special environments.

Reference: Z. Zhang et al., Stronger increases but greater variability in global mangrove productivity compared to that of adjacent terrestrial forests. *Nat. Ecol. Evol.* **8**, 239–250 (2024). doi: 10.1038/s41559-023-02264-w

Image Source: Photo by Mohamed Nazeem. Image Free to use under the Unsplash License.

Human Development in a Dish: All About Environment!

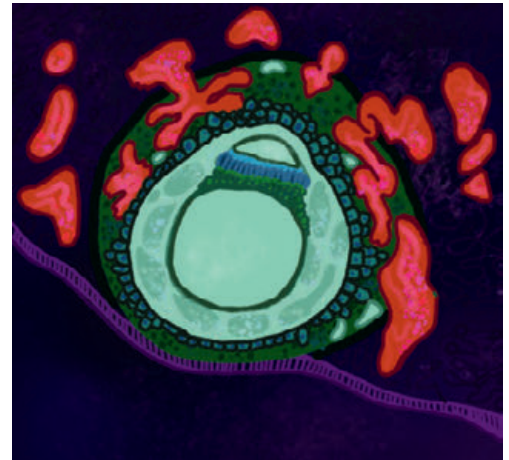
Eliana Bohn

Stem cells have been a hot research topic in recent years, with increasingly complex technologies being developed. The field is now pushing the boundaries of how we can faithfully study human development without the ethical qualms of using real human embryos. A recent discovery has revealed a new, elegant way to approach this effort. Researchers have found that it is possible to model the organization of nearly all known cell lineages and compartments of human embryos within a petri dish. Researchers can simulate development for 14 days after implantation, beginning simply with genetically unmodified human naive embryonic stem cells. The trick? Growing them in the right environment! Although formation efficiency is still low and variability is high, this is a major step in the field as a tool for future ethically conducted studies to better understand human development, associated developmental disorders, and early pregnancy loss.

Image: Artistic rendition of an implanted embryo.

Reference: B. Oldak *et al.*, Complete human day 14 post-implantation embryo models from naive ES cells. *Nature* **622**, 562–573 (2023). doi: 10.1038/s41586-023-06604-5

Image Source: Illustration by Eliana Bohn.



Space's Greatest Mystery: What Lies Between a Neutron Star and Black Hole?

Summer Kelso



The discovery of a rapidly spinning millisecond pulsar (PSR J0514–4002E) within a globular cluster in the Columba constellation, has sent shockwaves through the astronomical community. Globular clusters are dense, gravitationally bound groups of stars that have a high formation rate of millisecond pulsars (rapidly spinning neutron stars). Utilizing L-band and ultrahigh frequency receivers, the MeerKAT telescope was used to scan the area, and it detected faint emissions from the pulsar. Astronomers measured the fluctuations of these pulses, which revealed that the pulsar was part of a binary system. The pulsar's mysterious companion hovered in a mass range between black holes and neutron stars, challenging our current understanding of binary evolution and offering valuable insight into the dynamics of dense stellar environments. Additionally, this research could allow for the testing of gravity theories and unveiling of new insights into nuclear physics.

Image: Image of the Milky Way taken at Point Reyes National Seashore

Reference: E. D. Barr *et al.*, A pulsar in a binary with a compact object in the mass gap between neutron stars and black holes. *Science* **383**, 275–279 (2024). doi: 10.1126/science.adg3005

Image Source: Photo taken by Summer Kelso.

How Allergies Influence Avoidance Behavior

Truman Ma

If you suffer from a shellfish allergy, the mere scent of seafood may trigger an instinctive aversion. This raises an intriguing question: is this reaction rooted in past experiences or is it a part of the allergic response? Researchers at Yale suggest that these antigen-specific avoidance behaviors may be the result of a complex series of interactions between the immune and nervous systems. To study this phenomenon, the researchers induced an allergy in mice by the injection of ovalbumin (an egg protein) and an adjuvant. These mice, now allergic to ovalbumin, demonstrated an aversion to ovalbumin feeding solutions, whereas nonallergic mice strongly preferred the ovalbumin solution. Interestingly, knockout mice that lacked IgE antibodies (a potent allergenic mediator) did not display this aversion. These findings suggest that immune system signaling can modify behaviors, indicating that the immune system's relationship to the nervous system may be far more intricate than previously thought.



Image: Mice are common model organisms for immunological research due to their physiological similarity to humans

Reference: E. B. Florsheim *et al.*, Immune sensing of food allergens promotes avoidance behaviour. *Nature* **620**, 643–650 (2023). doi: 10.1038/s41586-023-06362-4

Image Source: Photo by Pixabay: <https://www.pexels.com/photo/brown-rat-eating-peanuts-206627/>. Free to use under CC0.

Old Tire Crumbs? Use it to Improve Earthquake-Resistant Building Technology

Joyce Goh

Earthquake-resistant building technology, such as seismic isolation, has long been researched to reduce the number of lives lost during these unpredictable natural disasters. However, the implementation of current technology is heavily limited given its high cost, with developed countries also struggling to ensure continued financing. Recently, a multi-institutional research team utilized a series of simulations to uncover that adding recycled materials—specifically tire crumbs—into the seismic load of the isolation technology can help to not only increase the shear strength of the building and reduce inter-story drift, but also to reduce the cost of the technology. Results point towards a 30% mixture providing optimal effects, increasing the shear strength of the soil by 30% and reducing inter-storey drift by 40-50%. This research opens the door for developing countries to adopt more earthquake-resistant building technology, serving as a cost-effective and sustainable way to protect human lives.

Image: UCLA's Powell Library under construction to improve seismic resilience.

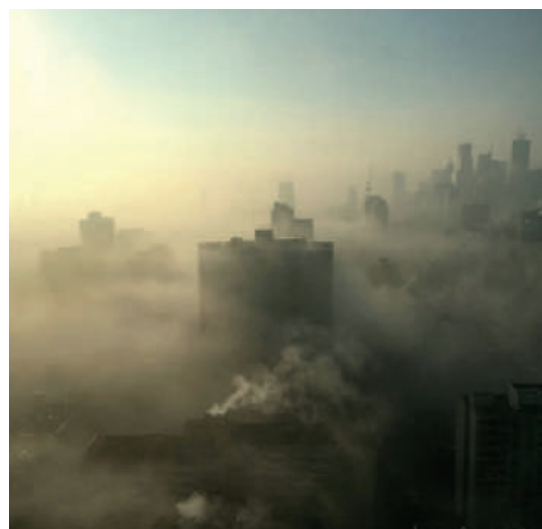
Reference: J. C. J. Raj et al., Numerical modelling on geotechnical features of soil mixture using recycled tire crumb to strengthen the seismic isolation in building. *Sci. Rep.* **14**, 225 (2024). doi: 10.1038/s41598-023-50741-w

Image Source: Photo by Joyce Goh.



Unmasking Air Pollution's Impact on our DNA

Lily Zello



As rapid urban growth and increased industrialization compromise air quality, research has delved into air pollution's impact on our health. A recent study aims to unravel how particulate matter (PM), one of the most complex environmental pollutants, affects the epigenome—the subtle switches that regulate gene expression without altering the underlying DNA sequence. By analyzing relevant molecular biology research from the past several years, including studies involving DNA methylation profiling and histone modification analysis, researchers scrutinized how exposure to PM induces changes to the molecular mechanisms that drive human disease. The results revealed evidence of epigenomic damage contributing to serious health problems such as cancer, fibrosis, neurodegeneration, and metabolic diseases like diabetes. This study offers valuable insights into the toxicity of PM at the epigenomic level and underscores the urgent need for global pollution reduction. Future research involving sequencing technology is crucial for developing targeted interventions to address this complex issue.

Image: Air pollution can damage the epigenome and contribute to serious health problems.

Reference: D. Gavito-Covarrubias et al., Epigenetic mechanisms of particulate matter exposure: air pollution and hazards on human health. *Front. Genet.* **14**, 1306600 (2024). doi: 10.3389/fgene.2023.1306600

Image Source: Photo by Kristen Morith. Image Free to use under the Unsplash License.

Predicting Attraction Through Physiological Responses

Ying yin (Lina) Zhu

The fundamental need for meaningful connections has driven individuals worldwide to partake in blind dating in hopes of finding mutual attraction. Factors that have historically been associated with attraction include general conversation, eye gaze, facial expressions, and body posture. Additionally, individuals on blind dates often report experiencing a “gut feeling of connection” that contributes to their attraction. However, this feeling has traditionally been challenging to quantify. Researchers from Leiden University addressed this by measuring physiological responses among blind date participants using eye-tracking glasses, cameras, and sensors. Findings revealed physiological synchrony, including matching heart rates and similar levels of electrical conductance in the skin, highlight a role of unconscious physiological alignment when fostering romantic connections. This research underscores the potential of physiological synchrony as a metric for relationship compatibility and paves the way for future technologies to monitor and understand the subconscious aspects of romantic attraction and human connections.

Image: Blindfolded man and woman engage in a first date

Reference: E. Prochazkova et al., Physiological synchrony is associated with attraction in a blind date setting. *Nat. Hum. Behav.* **6**, 269–278 (2022). doi: 10.1038/s41562-021-01197-3

Image Source: “Blind date in silhouettes.” Image Free to use under the iStock License.



Serum-Free Media Efficiently Produces Lab-Grown Muscle Cells

Zachary Lamm

Traditional livestock-based meat has a large carbon footprint, making it a major contributor to global warming. A novel alternative is cultivated meat, or meat grown via animal cell culture. However, most cultivated meat is grown in animal-based media containing fetal bovine serum (FBS) from cow embryos. In light of ethical and commercial considerations, researchers at the University of California, Davis compared the growth and metabolic rates of mouse myoblast (muscle cell) samples in either FBS-based media or serum-free media without FBS. Using cell imaging and spent media analysis, the researchers found that cell growth rates were similar across both media, but the cells required slightly less amino acids and glucose in serum-free media than FBS-based media, highlighting differences in metabolic requirements. By optimizing the nutrients and growth conditions of serum-free media, progress can be made towards scalable, animal-free, and affordable cultivated meat production.



Image: A platter with cultivated meat sausages, an example of a potential cultivated meat product.

Reference: E. N. O'Neill et al., The effect of serum-free media on the metabolic yields and growth rates of C2C12 cells in the context of cultivated meat production. *Future Foods* **7**, 100226 (2023). doi: 10.1016/j.fufo.2023.100226

Image Source: "Ivy Farm." Image Free to use under the Unsplash License.

Vegan Diet Offers Protective Cardiometabolic Advantages

Kyle Nguyen-Ngo



Vegan diets have become an increasingly popular alternative to the typical American diet, which is rich in meat, processed foods, and saturated fats. Researchers designed a randomized twin study to compare the impact of an omnivorous versus a vegan diet on key measures of cardiometabolic health, including low-density lipoprotein cholesterol (LDL-C) concentration. While LDL-C serves numerous physiological functions, raised LDL-C levels are associated with increased risk of coronary disease, stroke, and atherosclerosis. After the 8 week study, participants assigned to the vegan diet experienced a greater reduction in LDL-C concentration in comparison to their omnivorous counterparts. Furthermore, vegan participants also experienced a greater decrease in fasting insulin levels, suggesting lower susceptibility to developing diabetes. The study's use of twin participants reduced potential genetic and environmental variability, offering further support for the documented cardiometabolic benefits of a plant-based diet.

Image: Vegan diets are linked to reduced low-density lipoprotein cholesterol levels.

Reference: M. J. Landry et al., Cardiometabolic Effects of Omnivorous vs Vegan Diets in Identical Twins: A Randomized Clinical Trial. *JAMA Netw. Open.* **6**, e2344457 (2023). doi: 10.1001/jamanetworkopen.2023.44457

Image Source: Image available under public domain.

World's First Functional Nanoscale DNA Electromotor

Chahak Gupta

Synthetic nanorobots working within a cell's molecular processes might seem like something straight from the pages of a science fiction novel, but recent advances have blurred the line between reality and fiction. Researchers have designed the world's first functioning nanoscale electromotor made of DNA strands, and it utilizes a cell's electrochemical potential to produce torque when driven by the flow of solvent through a nanopore. The authors manipulated the direction of the turbine's rotation by toying with the chirality of the blades and the ionic strength of the buffer. Despite its small size of approximately 27 nm, the turbine can produce mechanical force comparable to that of natural motor proteins, like ATP synthase, without constant manual intervention. These turbines could link mechanical rotation with chemical synthesis, providing self-powered biocompatible engines at the nanoscale.

Image: The turn of a DNA strand modeled by wooden blocks.

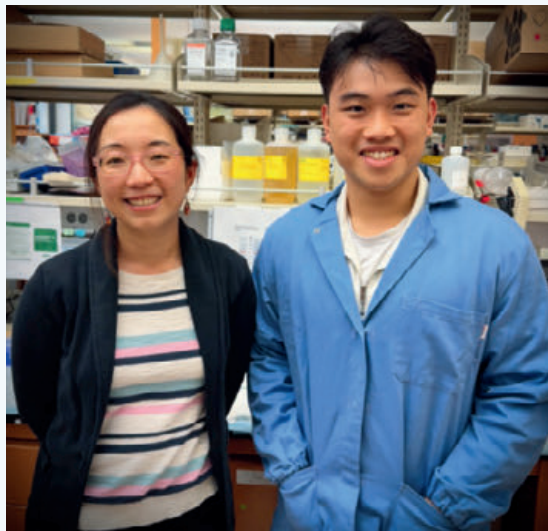
Reference: X. Shi et al., A DNA turbine powered by a transmembrane potential across a nanopore. *Nat. Nanotechnol.* **19**, 338–344 (2024). doi: 10.1038/s41565-023-01527-8

Image Source: "DNA Turbine" by FLICKR user Nikolai Vassiliev. Licensed under CC BY-NC-SA 2.0.



Integrating the Past for a Sustainable Tomorrow: The Revolutionary Approach to HIV Treatment with CAR-NK Cells

by Charlotte Chen, Isabel Angres, Chahak Gupta, Ahmad Ismail, Emily Lin, Sohan Talluri



Principal Investigator & Student
Anjie Zhen, PhD & Vincent Le
 Department of Medicine,
 David Geffen School of Medicine

Immunotherapy is an innovative medical paradigm that leverages the body's own immune system to recognize and combat disease from within, as opposed to treating disease via external interventions such as medication or surgery. These therapies have transformed the ongoing effort to combat cancer, autoimmune disorders, and infectious diseases such as human immunodeficiency virus (HIV) that were previously deemed untreatable. Since the emergence of HIV in the US in the early 1980s, research into the virus has faced significant obstacles, largely due to the misconceptions and fear surrounding the disease. This stigma, combined with the complex virology of HIV, poses difficulties for researchers by limiting the availability of funding and public health initiatives dedicated to studying and treating the disease.

Undeterred by these challenges, Dr. Anjie Zhen and her mentee Vincent Le are currently working on a novel immunotherapy approach using chimeric antigen receptor-natural killer (CAR-NK) cells to tackle HIV. This strategy modifies NK cells to express chimeric antigen receptor (CAR) proteins that enable them to specifically target and eliminate HIV-infected cells. NK cells are a type of lymphocyte that play a key role in the innate immune system by recognizing and destroying cancerous or infected cells, including those infected by HIV. CAR-NK cell therapy stands

out for its ability to harness the innate power of the immune system against a disease where traditional treatments such as antiretroviral therapies have fallen short, reflecting a significant advancement in the fight against HIV.

Despite her achievements in the immunotherapy field, Dr. Zhen did not start off intending to pursue immunology, let alone medical research. As an assistant professor in the Department of Hematology and Oncology at the UCLA David Geffen School of Medicine, Dr. Zhen's journey to becoming an independent investigator was shaped more by genuine passion than strategic planning. Dr. Zhen majored in Biological Sciences at Tsinghua University in Beijing and got her doctoral degree from the Department of Molecular Microbiology and Immunology at Johns Hopkins, where she studied HIV virology and viral-host interactions. She subsequently became interested in HIV immunology and gene therapy and pursued postdoctoral training with Dr. Scott Kitchen at UCLA, who was then a new assistant professor. Dr. Zhen received offers from more established and well-known PIs from other prestigious institutes, but she ultimately chose UCLA to follow her research passion. In particular, Dr. Zhen was drawn to HIV research not only because of the field's culture of openness and acceptance, which offered her a nurturing environment for personal and professional growth, but also by the opportunity to contribute towards healthcare advancements, stating, "I wanted to be involved in something that could have an impact on society."

Reflecting on her academic and professional journey, Dr. Zhen acknowledges that her unconventional approach, guided by raw interest rather than job security, has strongly influenced her career. She admits that she was not the "typical science prodigy" and often made career-related decisions based on her emotional connection to her work rather than the conventions of the field. She offers encouragement to those uncertain about their career paths, asserting that true fulfillment comes from pursuing one's passions rather than adhering to predetermined careers chosen for their prestige or wealth. Dr. Zhen also recognizes that "there may be ups and downs," but that this applies to anything worth pursuing.

The heart of Dr. Zhen's current research lies at the intersection of gene therapy and the interpretation of immune responses. Utilizing hematopoietic stem cells as a vessel, she is developing gene therapies to generate long-lasting immunity against chronic diseases such as HIV. Her work also delves into the analysis of cellular behaviors underlying chronic diseases, leading to critical insights in the fight against these conditions. Additionally, Dr. Zhen contemplates the improved but incomplete state of

HIV treatment, recognizing that despite the progress made with antiretroviral therapy, people living with HIV still suffer from chronic inflammation. As a result, her research also aims to elucidate these complex inflammatory responses, which sometimes elude even the most promising engineered therapeutic strategies, in order to develop novel treatments for HIV. Dr. Zhen points out that the challenge lies not only in the diseases themselves but also in improving the efficacy of current therapies. Her approach to science is rooted in continuous learning and adapting to the insights gleaned from each new finding.

Dr. Zhen's commitment to learning extends her involvement in the HIV field beyond the laboratory into teaching, as she also serves as an assistant adjunct professor and teaches several classes at UCLA. In one of these classes, she met Vincent Le, a current fourth-year student at UCLA majoring in Psychobiology. Le's interest in immunotherapy was sparked in his first year after taking Dr. Peiyun Lee's course "Stem Cell Biology, Politics, and Ethics: Teasing Apart Issues." Le was particularly fascinated by the engineering of stem cells using CRISPR-Cas9, and this motivated his desire to work in a lab that specializes in cell engineering. Combined with his burgeoning interest in HIV and virology, this inspired him to join Dr. Zhen's lab, marking the beginning of his own journey into immunotherapy research.

After three months of training in cell culture and viral transduction techniques, Le began working on the CAR-NK cell project. This project was based on a novel strategy to utilize NK cells to enhance immune functionality, instead of the traditional approach, which targets the HIV viruses themselves. Le's two years of research in the lab culminated in developing functional CAR-NK cells from healthy donors, which show promise in targeting HIV-infected cells. Le's findings highlight the superior efficacy of the Miltenyi Biotec NK MACS Medium—a specific nutrient solution that supports NK cell proliferation—and the successful transduction of NK cells with the D1D2-CAR-41BB lentivirus, a genetically engineered virus that carries a blueprint for a CAR protein designed to target HIV-infected cells, leading to the production of fully functional CAR-NK cells.

For Le, the research process delved deep into uncharted territory, as only limited information on CAR-NK cell clinical trials exists worldwide. As a result, Le had to tackle a steep learning curve as he explored the complexities of cell culture and transduction. After overcoming challenges including inconsistent donor NK cell responses and suboptimal transduction efficiency, Le found that the NK MACS medium, combined with specific concentrations of the cytokine signaling molecule interleukin-2 (IL-2), yielded promising results for NK cell expansion. Le also investigated whether CAR-NK cells could address the limitations of other immunotherapies against HIV. The innate ability of CAR-NK cells to bypass the complications of graft-versus-host disease (GvHD) positions them as a preferable candidate to CAR-T cell therapies. Additionally, the ability of NK cells to directly target and kill infected cells without the need for prior sensitization and lower likelihood of initiating severe immune responses offers a safer alternative for immunotherapy.

Inspired by his current progress, Le is set on translating the successes achieved with CAR-NK cells in the lab (*in vitro*) into

tangible results in living organisms (*in vivo*). Recognizing the current limitations in the efficiency of CAR-NK cell transduction, Le plans to refine this process by exploring whether different CAR constructs will work better in different primary NK cells. Le then aims to use humanized mice to test the *in vivo* efficacy of his research, as he views implementation in mouse models as the next step towards clinical translation. In particular, he intends to collaborate with the UCLA Center for AIDS Research (CFAR) Humanized Mouse Core Laboratory directed by Dr. Scott Kitchen to test the efficacy of CAR-NK treatment *in vivo* using humanized mouse models of HIV infection. The potential significance of Le's work transcends the boundaries of HIV treatment, setting the stage for CAR-NK cells to ultimately be tailored to tackle a broad range of chronic or terminal diseases. Given the global impact of HIV, Le envisions a one-time, off-the-shelf CAR-NK-based treatment, and with the promising shift towards more accessible therapies, this may soon become a reality—a stark contrast to the lifelong antiretroviral regimens that dominate current HIV therapeutic strategies.

Relatedly, Le is exploring the impact of cannabis, specifically the compounds tetrahydrocannabinol (THC) and cannabidiol (CBD), on immune functions. This new avenue investigates how these substances may affect the efficacy of CAR-NK and other immunotherapies by potentially modulating the inflammation caused by HIV. This research is particularly relevant given the recent legalization of marijuana in California and the increasing recreational and medicinal usage of cannabis, prompting exploration of holistic and comprehensive approaches to immunotherapy.

Le's research journey has been more than simply an academic endeavor; it is also deeply personal. His immunotherapy research only expanded his interest in medicine, and he will begin attending medical school in July, where he intends to continue his biomedical research. Le's determination to deliver improved patient outcomes through translational research is not only a career choice but a "lifelong interest" in bringing the power of discovery from the microcosm of petri dishes to the macrocosm of patient care.

Beyond spearheading scientific studies, both Le and Dr. Zhen place significant emphasis on the importance of communicating their findings to the public in order to encourage young students to learn and break down the ivory tower of academia. In particular, Dr. Zhen credits the growth of the immunotherapy field to effective communication resulting in increased youth and general public engagement. In her eyes, a good scientist should be able to "describe [their] research to a seven year old." The ability to explain complex research in simple terms is not only a communication skill—it is reflective of a scientist's depth of understanding, and to win both the attention and comprehension of a seven-year-old would demonstrate a researcher's ability to convey the significance of their work to a general audience. She encourages students and young researchers to engage in community outreach for this reason, and also to connect their research with its broader social implications.

Dr. Zhen and Le's venture into CAR-NK therapy for HIV exemplifies a commitment to exploring unconventional paths

in a field that not only requires incisive scientific acumen but also empathy and an understanding of societal nuances. Their research both advances immunotherapy and also encourages the reevaluation of research priorities within the field of higher academia. By embracing novel research methods, their approach has the potential to lead to significant breakthroughs, especially in areas previously hindered by scientific and social challenges. Dr. Zhen and Le's collaboration underlines the importance of integrating translational research with public health efforts to develop sustainable HIV treatments. It also exemplifies how constant inquiry and embracing diverse perspectives are crucial in driving healthcare innovation.

Vincent Le & Anjie Zhen are authors of "Production and Growth of CAR-NK Cells to treat HIV Infection" on page 30.

Bringing Gene Therapy to the Public: Increasing Treatment Accessibility and Science Literacy

by Ahmad Ismail, Emily Lin, Caden Chow, Chloe Nelson, Lee Zucker-Murray



Principal Investigator
Steven J. Jonas, MD, PhD
 Department of Pediatrics,
 University of California, Los Angeles



Student
Alicia J. Sanoyca
 Department of Microbiology, Immunology, and Molecular Genetics,
 University of California, Los Angeles

Gene therapy lies at the intersection of biological research and genetic engineering—it is a rising medical technology where disease-causing genetic mutations are either replaced with healthy copies of a gene or are altered using gene editing tools to treat genetic diseases, cancers, and other pathologies. The increasing prevalence of gene therapy comes with concerns regarding equal accessibility and public scientific literacy, particularly as these approaches enter clinical practice. Understanding these concerns, author Alicia Sanoyca and her advisor Dr. Steven J. Jonas have worked towards developing a more accessible mode of delivery for gene therapies.

Sanoyca is a fourth-year undergraduate student at UCLA majoring in Microbiology, Immunology and Molecular Genetics and minoring in Biomedical Research. Following graduation, Sanoyca plans to pursue a PhD before working in the biological research industry. Sanoyca had always been fascinated by the process of scientific inquiry, and was particularly interested in gene therapy research during college. As part of her Biomedical Research minor, Sanoyca created a list of research topics that she would be interested in exploring and a counselor from the minor identified Dr. Jonas's work as a good match for Sanoyca's interests in human cell culture and nanoparticles. Sanoyca joined Dr. Jonas's lab during her third year.

Prior to working with Dr. Jonas, Sanoyca explored her research interests across a wide variety of fields. During high school,

Sanoyca participated in the California State Summer School for Mathematics and Science (COSMOS), a four-week summer program at UC San Diego where she researched gene editing in algae. After coming to UCLA, she continued to diversify her research interests, conducting ecological research related to birds as well as bioinformatics research into machine learning algorithms for cell sorting. Over the past two summers, she worked at the Carnegie Institute researching microscopic organisms called cyanobacteria that live in the hydrothermal vents of Yosemite National Park, studying their movement in response to light.

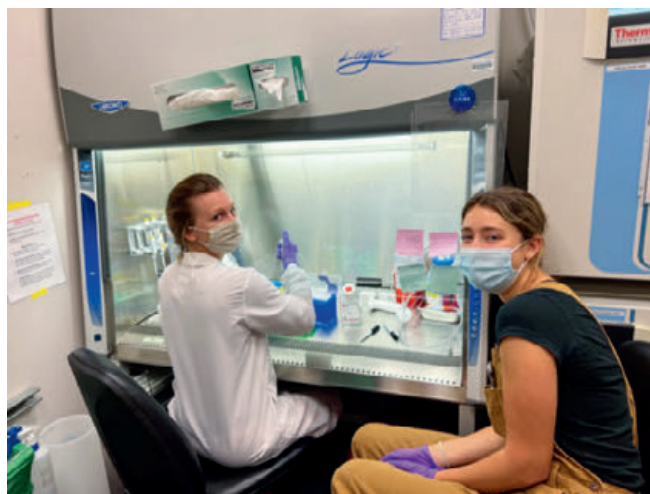
When Sanoyca first met Dr. Jonas, she was intrigued by his discussion of accessible vehicles for gene therapy delivery. The price tag of many pharmaceutical drugs poses significant barriers for low-income patients, and Sanoyca was excited to contribute to developing more accessible therapeutics. Dr. Jonas is an expert in this field, having received his MD-PhD in Materials Science and Engineering at UCLA under the supervision of Dr. Bruce Dunn, and later completing his residency in Pediatrics and fellowship training in Pediatric Hematology/Oncology at UCLA. In his lab, Dr. Jonas uses his expertise in materials engineering and overseeing the medical care of children with cancers and blood diseases to develop nanotechnologies for safe, cost-effective, and efficient delivery of gene therapies to immune and stem cells. Dr. Jonas designs his therapeutics for precision pediatrics, which he describes as a patient-tailored approach, particularly for childhood cancer and other rare diseases.

Dr. Jonas's lab specifically focuses on reducing the costs and increasing the efficiency of pre-existing therapies to expand the accessibility of such life-saving treatments. He mentions how his research group aims to contribute to a portfolio of gene therapy delivery approaches, as he does not believe there is a "silver bullet" that will work for all diseases and patients. His lab works to "make [gene] therapies more accessible to others [using] engineering tools and principles," particularly aiming to reduce the cost of treatment. Sanoyca's work specifically seeks to optimize the formulation of lipid nanoparticles (LNPs), which are spherical delivery vehicles made of fat molecules. LNPs can provide a more sustained and controlled release of cargo, resulting in a cheaper mode of delivering gene therapy machinery compared to traditional approaches that use modified viral vectors.

Cystic fibrosis (CF) is a rare genetic disorder that harms multiple organs of the body, particularly in the digestive and respiratory system. This disorder affects a membrane transport protein in cells that normally produce mucus, sweat, and digestive fluids. In normal patients, these secretions are thin and slippery, but for patients with CF, they are much thicker. CF is a progressive disease that requires patients to have constant care, impeding regular daily activities. Sanoyca decided to focus her research on CF due to the multiple mutations that can give rise to this condition. Given that CF is a single-gene disorder, Sanoyca says that "it could theoretically be solved by a single gene insertion." Based on the Pfizer and Moderna COVID-19 vaccines in which mRNA is delivered via LNPs, Sanoyca and her graduate student mentor Ruth Foley wanted to use LNPs to directly target bronchial epithelial stem cells. In developing these LNPs, Sanoyca used lipids that have been clinically tested in other therapeutic LNPs, but that are also easily accessible to lower the resource burden.

When scaling drug models from the lab setting into the hands of physicians, many considerations related to efficacy and effectiveness need to be made. Sanoyca highlighted the importance of consistency in laboratory results in order to minimize variability when moving to larger sample sizes. The strategy would also have to consistently maximize the transfection rate, which is a measure of how efficiently therapeutic cargoes are delivered to the cell, in order to optimize the treatment for *in vivo* testing. Furthermore, existing literature on the topic reveals that poor particle integrity causes inflammation when used *in vivo* in patients. Sanoyca points out that the use of LNPs as a drug already introduces foreign materials in the body that could potentially trigger immune responses. Therefore, particle integrity and biodegradability would be key to minimizing serious side effects, including severe inflammation.

No research project is without challenges, and Sanoyca's project is not an exception. In terms of the project's scope, Sanoyca notes that gene delivery to specific target cell populations is difficult, since LNPs are inherently nonspecific as a drug. She aims to deal with this challenge by utilizing antibodies that are specific to epithelial cells and attaching them to the surface of the LNPs. When the LNPs are introduced *in vivo*, the epithelial-specific antibodies will only attach to cells in the target tissue, effectively delivering the LNP. Without this specific targeting, the LNPs could potentially end up in other parts of the body, such as the liver, where they would not be of much use as a treatment for CF.



While it may be challenging, exposure to independent research provides many foundational skills for students seeking to pursue a career in science. Dr. Jonas emphasizes that searching for a lab to join as an undergraduate student is about finding your community and an environment that will teach you the vocabulary of science: "As you build up your vocabulary, you can start to string two words together. If you can string two or three words together, you've got a sentence. If you can put together a sentence you can put together a question."

At a large research institution like UCLA, undergraduate students have the opportunity to gain exposure to many different levels of the scientific research process. Sanoyca mentions independent research has allowed her to become more cognizant of experimental methodology and design. When working on her independent project, she is responsible for the research from start to finish. As such, Sanoyca also created her own research design based on existing literature. Close evaluation of existing papers revealed gaps in the field, so Sanoyca has been searching for alternatives with the plethora of resources available at UCLA. Working on her own project has offered her greater control over her research, allowing her to grow as an independent researcher more than when she participated in a more guided approach.



For undergraduate researchers, the challenges often stretch beyond the projects themselves and extend to logistical and academic hurdles. In blunt terms, Sanoyca states that one of her greatest limitations is that she “is a student and has classes.” Currently, Sanoyca spends more time in her lab than in her classes. Nevertheless, Sanoyca constantly has to schedule experiments around her classes and other commitments, including her jobs and her participation in a club sports team that competes at the national level. Sanoyca says that her fragmented experimentation schedule can be frustrating at times. In the lab setting, she describes how “sometimes, you might conduct an experiment, have it fail, and then realize that you need to change something.” The difference between a normal lab setting versus her project as a student researcher is the time Sanoyca needs to wait before restarting the experiment. For Sanoyca, this waiting period can last multiple days as she schedules around classes, exams, and projects.

Although Sanoyca’s research focuses on the delivery of gene therapy for CF, Dr. Jonas specializes in pediatric cancers, blood diseases, and regenerative medicine. “[The] last time I took care of someone with cystic fibrosis was in residency, but Dr. Gomperts is a close colleague of ours who’s also a pediatric oncologist and a really big expert in the cells of the airway,” says Dr. Jonas. Despite newly entering the field, Dr. Jonas was quickly adopted into the CF research community, an experience he has found very fulfilling. In doing so, he also found the wonderful collaborators Dr. Brigitte N. Gomperts and Dr. Donald B. Kohn to bring their knowledge and experience to Sanoyca’s project. This reflects Dr. Jonas’s philosophy that values collaboration in asking questions and devising solutions in his research.

Dr. Jonas’s emphasis on the importance of collaboration in research was influenced by his postdoctoral advisor, Dr. Paul S. Weiss, as well as his time working both in research and clinical medicine at a collaborative institution like UCLA. In particular, Dr. Weiss’s comment that “UCLA is a big vortex of collaboration” has stuck with Dr. Jonas. Throughout his career, Dr. Jonas has greatly benefited from both working with his collaborators and working at such a large research and medical institution, which, despite its size, still has researchers and physicians so proximal to one another. “I can be across the street, rounding with my patients, and then I can walk across the street to the lab, and on that walk over, I

could see people who might be experts in the question that popped in my head seeing a patient,” says Dr. Jonas, then remarking on the willingness of scientists at UCLA to explore big problems.

The formulation of LNPs can extend beyond Sanoyca’s use for the delivery of CF therapies to all gene therapies. This cost-effective, materials-based focus, Dr. Jonas believes, is the next step in gene therapy development. The existing gold standard of gene therapy is to utilize natural viral vectors and manipulate them to enact the necessary genetic modifications, but there is still much to be desired in the field, explains Dr. Jonas. In particular, current gene therapies are limited by size (i.e. how much cargo can fit in one vehicle), insertional mutagenesis, immunogenicity, and cost. Cost, in particular, is a large concern for Dr. Jonas and his lab, as they focus on accessible technologies. Unfortunately, the drug development pipeline is very expensive, in part because of the necessary compliance to regulations that require costly cleanrooms for manufacturing, as well as very specific and fine-tuned formulations of the drug itself. Furthermore, the nature of gene therapy is that every minor change to the cargo and editing machinery requires large reengineering—almost starting from scratch—which greatly adds to the cost. As a result, another project in Dr. Jonas’s lab focuses on answering the question: How cheap can you make cell transfection? Cell transfection is necessary for research and application of gene therapies that must infiltrate the cell in order to edit the DNA inside, but not all facilities have access to the best, most expensive tools for transfection. Dr. Jonas’s lab has found a way to successfully transfect gene editing machinery and edit target genes for as low as \$7. “If folks had access to those types of tools, they’d be able to have more freedom of creativity scientifically, or get more people to engage in the conversation,” he says.

Despite these challenges in gene therapy, Dr. Jonas is optimistic, stating that “it’s [in its] early days, but it’s reached the zeitgeist at this point. It’s evolving rapidly.” In 2012, the first patent for CRISPR/Cas9 (the gene editing gold standard technology) was filed; in 2020, Emmanuelle Charpentier and Jennifer Doudna were awarded the Nobel Prize in Chemistry for their work on CRISPR/Cas9; and in late 2023, the FDA approved Casgevy, the first CRISPR-based gene editing therapy to treat sickle cell disease. With the increased development of gene editing technologies, Dr. Jonas looks towards addressing the ethical and accessibility concerns of this technology through not only his research, but also by improving scientific literacy.



Given the amount of misinformation during the recent coronavirus pandemic, Sanoyca stresses the importance of scientific communication with the public. As a member of the public herself, she remarks that absent a pandemic, scientists are not making much of an effort towards outreach and education. Specifically, she explained that the COVID-19 pandemic showed that many people are scared of science, partially due to difficult technical jargon and partially to the high cost of access. This high cost is due to monopolies in scientific publication, which result in science being hidden behind a paywall and often force the public to trust a middleman source. She further recalls how, even before the pandemic, some people were already hesitant of vaccines, but their skepticism was not addressed. However, she also remarks that the Centers for Disease Control and Prevention (CDC) did take steps towards increasing public scientific literacy during the pandemic through their weekly debriefings with Dr. Anthony Fauci. Although Sanoyca is not convinced that this is sustainable during a time outside of a pandemic, she believes that these efforts demonstrate the need for more digestible pieces of scientific information.

Similarly, Dr. Jonas has been working towards public scientific literacy, but he is doing so through his dual role as a physician-researcher, which allows him to address such concerns on a

patient level. An MD-PhD “gives you a different perspective on how you treat medicine [and] how you treat your patients,” he states, recounting how his PhD provides him with a different perspective on which scientific questions to ask, while his MD helps him contextualize his research—it has helped him become “scientifically multilingual.” In particular, his fundamental science and engineering knowledge has helped him logically think through problems in the clinic that he otherwise may have panicked over. Furthermore, Dr. Jonas has seen the impact that diseases—diseases that he aims to treat through his research—have had on his patients. Thus, he believes that researchers have a duty to at least explore gene therapy avenues, especially for diseases with a large impact on life expectancy and quality of life, such as CF, sickle cell disease, and childhood cancers.

Because gene therapy is such a broad area, Dr. Jonas stresses that it will take concerted efforts from many different disciplines to devise new strategies and tools to improve their accessibility and efficiency, as well as provide patients suffering from currently incurable genetic diseases with a definitive, curative approach using gene therapy. He concludes, “Hopefully our lab is one example at UCLA that is going to make a tiny little contribution to all that moving forward.”



Alicia J. Sanoyca & Steven J. Jonas are authors of “Optimizing Ionizable Lipids in Nanoparticles for Human Bronchial Epithelial Cells” on page 23.

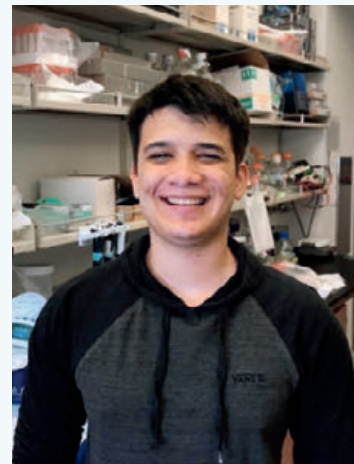
Advancements in Skeletal Dysplasia Research: From Genomic Discoveries to Clinical Solutions

by Agamroop Kaur, Ahmad Ismail, Emily Lin, Derek Ren, Joanna Rhim



Principal Investigator
Daniel Cohn, PhD

Department of Molecular, Cell, and Developmental Biology,
University of California, Los Angeles



Student
Derick Diaz

Department of Molecular, Cell, and Developmental Biology,
University of California, Los Angeles

Dr. Daniel Cohn is a professor of Molecular, Cell, and Developmental Biology and Orthopaedic Surgery at UCLA. He joined the UCLA faculty in 2011, having previously taught medical and graduate school students through his appointment at the Cedars-Sinai Medical Center. Currently, his lab aims to change how patients understand their disease diagnosis based on the fundamental biological findings they discover.

As a Principal Investigator, Dr. Cohn's lab focuses on investigating the molecular basis of inherited disorders that affect skeletal development, growth, and maintenance by conducting genomic analyses in families with skeletal dysplasias—genetic disorders that cause abnormal development of bone and cartilage. He explains, “[in the lab] we study people—these are people with genetic conditions—and we want to help them... even if it's just to better understand the disorder and what their prospects for the future are.”

In 2007, Dr. Cohn began a research project focusing on a family with spondylometaphyseal dysplasias (SMDs), a group of short-stature disorders found to result from activating mutations in the *TRPV4* gene. While searching for a means of treating the family's condition genetically, Dr. Cohn's lab came across a unique finding that showed promise to address the cause of the skeletal disorder: a mutation in a gene that codes for Ca^{2+} channels results in overactivated mutant channels. Ca^{2+} channels are an important focus as the channels control the influx of Ca^{2+}

into cartilage and other cells. This finding opened the door for further analysis into the connection between abnormally high calcium levels and disrupted skeletal development.

Dr. Cohn describes studying this disease as “opportunistic,” in that the lab was in the unique spatial and temporal position to have access to samples from patients with the disease and the ability to characterize the genetic underpinnings of the disorders from the samples. Unfortunately, a common limitation in genetic research is that the diseases are so rare that there are only a few affected people in the world. To address this issue, Dr. Cohn, together with his colleague Dr. Deborah Krakow, directs the International Skeletal Dysplasia Registry, which partners with clinics and hospitals to collect material from patients with skeletal diseases across the globe. In addition to developing the Registry, Dr. Cohn has taken advantage of technological advancements in genetic analysis that have allowed researchers to circumvent the limitations of small sample sizes. Innovations from the Human Genome Project (HGP) have led to the creation of automated software that compares people's genomes and reduces the need for large families in order to study the basis of rare diseases. Thanks to the broad coverage provided by modern genome sequencing, the field of skeletal dysplasia has shifted research towards exploring curative possibilities.

“It's time to start making people's lives better through treatment and not just diagnostic testing.” -Dr. Cohn

Translational advancements in the field are crucial, since research often races against disease progression in individuals. While Dr. Cohn's previous work has focused on fundamental biological findings, the current trajectory of his lab has veered toward a more bench-to-bedside approach. The aim now extends beyond the mere acquisition of knowledge about the disease to focus on the development of therapeutics that could tangibly improve the lives of those affected.

Derick Diaz joins Dr. Cohn in this new direction. Diaz is a fourth-year undergraduate studying Biology at UCLA and is a first-generation student who met Dr. Cohn through the Biomedical Science Enrichment Program (BISEP). Diaz's research journey began with the Program for Excellence in Education and Research in the Sciences (PEERS) during his freshman year, which supported his scientific interest in physiological disorders through professional development opportunities, eventually leading him to skeletal dysplasias and developmental biology. Under the mentorship of Dr. Cohn, Diaz has immersed himself in the complexities of genetic analysis and learned experimental techniques including radiography and conducting quantitative and qualitative assessments of development in mouse models, contributing to his growth as a researcher and to the lab's findings as a whole.

As prior research in the Cohn Lab determined that mutations in the *TRPV4* gene produced a spectrum of skeletal dysplasias, Diaz has worked to extend this research into understanding whether the overactivity of the Ca^{2+} channels can be "turned off" via a targeted therapeutic. To test for the consequences of TRPV4 protein overactivity, Diaz studied a mouse model generated from the lab to validate that it recapitulates the human TRPV4 skeletal disorder phenotype. Comparing mice with the mutant *TRPV4* gene to those with the wildtype gene elucidated the impact of the mutation on skeletal development.

Diaz highlights reproducibility as a key challenge of his research, as well as maintaining consistency when measuring vertebral bodies, stating, "What's the correct way to measure them? What's the most consistent [way to measure bones] because not every bone is the same? Sometimes they have abnormal shapes."

Both Diaz and Dr. Cohn point to the need for trial and error, as well as patience, when measuring bones based on radiographs of the mice and conducting retrials as necessary to ensure reproducibility and statistical significance. Their work eventually led to the validation of the mouse model that presented skeletal abnormalities consistent with the SMD Kozlowski type disorder observed in human patients. The use of *in vivo* mouse models is pivotal for therapeutic development, as it allows for the simulation of disease progression and evaluation of treatments under conditions that closely mimic those in human pathophysiology.

Currently, Dr. Cohn and his team are focused on preparing for clinical trials of potential therapeutics, bolstered by the confidence from their mouse models. One crucial aspect of this preparation involves conducting a retrospective chart review of cases with *TRPV4* mutations available in the Registry. This meticulous process involves combing through birth records, pre- and post-

diagnosis medical records, X-rays, growth curves, and other patient data. While navigating the extensive data from numerous individuals may seem daunting, Dr. Cohn remains optimistic about the potential insights to be gleaned, emphasizing how many cases can come together to create a holistic understanding of the disease. "We can think of 100 cases as 100 individual cases, or we can think of 100 cases as 1 case and how [a disease] can develop over time," said Dr. Cohn.

As his laboratory transitions toward advancing the treatment of skeletal dysplasia, Dr. Cohn reflects on what could be improved in the research process, while recognizing there's a collective ambition to enhance the quality, affordability, and efficiency of research in the field. A key aspect of achieving faster results is the accessibility of information from a scientific perspective, which not only aids the researchers but also benefits patients. These next steps call for a collaborative approach, involving both private and public partnerships. Such alliances are crucial in marshaling the necessary resources, expertise, and technology to accelerate research and development. Furthermore, these advancements will depend on the support from philanthropic organizations, government entities, and the technology sector, creating a collective will to push the boundaries of what is possible in medical science.

"Science builds on [the] success of people who came before them," said Dr. Cohn. As Dr. Cohn and Diaz continue to build upon prior research efforts, they embody the convergence of knowledge, mentorship, and the relentless pursuit of medical advancement. Their journey, marked by innovation and the desire to improve lives, serves as an inspiration for aspiring researchers. Reflecting on his own growth and contributions, Diaz encourages others to "give 120% of yourself and just go out there, meet people, don't be shy. I devoted 120% of myself to those programs and what I'm studying."

Derick Diaz & Daniel Cohn are authors of "The Effect of a TRPV4 Mutation on Skeletal Development in Mice" on page 47.

New Lab? No Problem. An Undergraduate's Journey Towards Finding Her Place In Academia

by Elise Tran, Daniel Bielin, Emily Lin, Raphael Low, Siddhika Naik, Vivasvaan Aditya Raj



Principal Investigator
Elissa Hallem, PhD

Department of Microbiology, Immunology, and Molecular Genetics,
University of California, Los Angeles



Student

Aracely Garcia Romero

Department of Molecular, Cell, and Developmental Biology,
University of California, Los Angeles

Undergraduate students at UCLA place a lot of emphasis on finding a lab that fits their academic interests. Aracely Garcia Romero, a fourth-year undergraduate student at UCLA majoring in Molecular, Cell, and Developmental Biology, discovered that finding a supportive lab environment was far more rewarding than sticking to her initial research interests.

When Romero first became involved with research, her excitement for science quickly dulled due to the environment created by a previous research mentor. Any time she made a mistake, she felt embarrassed, rather than being encouraged to treat it as a learning opportunity. At one point, her mentor even suggested that she try a different career outside of STEM. The constant stress and pressure led to feelings of nervousness and anxiety, making it difficult to perform experimental procedures correctly. Romero was stuck in a perpetual cycle of anxiety leading to poor performance, which then intensified her anxiety. This hindered both her progress in the lab and the development of her scientific acumen.

Throughout this experience, Romero kept all of her thoughts, feelings, and struggles to herself. It wasn't until several months later, during her third year in college, that she found the courage to speak to others about her experiences. It was through these conversations with her friends and supportive lab members that Romero decided to take the initiative to advocate for herself. Romero attributes her resilience to having trusted peers

supporting her every step of the way as she overcame the barriers she faced in research.

"Feeling comfortable to at least try to get the support you need [is important] because, at the end of the day, that's really what's gonna help. I know it's easier said than done, but [being] able to reach out with the help of my support system, like my friend group, changed the trajectory of my scientific career," said Romero.

Her previous negative experiences pushed her to search for better mentorship. This led her towards a novel research path as she began working under the tutelage of Dr. Elissa Hallem and a postdoctoral fellow in the Hallem lab, Dr. Ruhi Patel. Romero began working directly with Dr. Patel on understanding the sensory-driven behaviors of parasitic worms—a significant shift from the cancer research she initially wanted to pursue. Romero's new environment was filled with peers and mentors who were open and understanding. In particular, Dr. Patel believed in guiding Romero's first attempts at unfamiliar procedures with reassurance and constructive insights. This positive atmosphere saw Romero's anxiety ebb away and her confidence and love for science return. It further enabled Romero to learn molecular biology techniques such as plasmid cloning and gel electrophoresis more efficiently than she would have imagined. Her knowledge of molecular biology also grew as she felt increasingly comfortable asking questions. Rather than harboring a fear of asking the

“wrong” questions, she learned to embrace the value of curiosity in academia through the support of her lab mates. Now, she is a confident budding scientist with a first-author paper published in the Undergraduate Science Journal at UCLA.

A case in point is the experience Romero had with Dr. Patel when she first learned to perform skin penetration assays, the main behavioral assay of her paper. Skin penetration assays consist of many moving parts and require memorization of a complex procedure, attention to detail, and a steady hand. From performing intricate behavioral measurements multiple times to understanding the different rates of penetration for various species, the procedure felt overwhelming for Romero to carry out. Despite this, Romero learned to persevere through mistakes and undesirable results. Romero credits the positive experience to the environment Dr. Patel cultivated, where instead of disparaging her mistakes, she empowered Romero to ask why something went wrong and how she could improve.

“[Dr. Patel] allowed me to ask her anything, like why this [experiment produced this result], and because I felt more comfortable to ask people questions, the breadth of my knowledge increased... I’m not fearful of talking to others. I know they actually want to help me, so I definitely saw big progress and how I [could] do things because of the way I felt,” said Romero.

Romero’s experience with Dr. Patel and her own growth in the lab have inspired her to serve as a mentor for others in the future. In particular, Romero hopes to play her part in reducing the obstacles that aspiring scientists experience within academia. Her goal is to ensure that future mentees feel comfortable talking to her about matters both inside and outside the lab, and by doing



so, help them develop confidence in themselves and their abilities to achieve their career goals. For Romero, science is fascinating and an integral part of her life, but she has also learned that mental health plays a critical role in achieving a fulfilling career. As a mentor, she hopes to help people recognize that mental health should take precedence in one’s scientific journey.

Romero said, “I learned [that] you do have to really take care of yourself and make sure that you’re advocating for yourself, and I learned that from [my] experience... I’ve definitely learned all of these things [at UCLA] and I want to give back to others, because what good is it to learn all these great things if you can’t share it back to the future generations?”

Although Romero is not a mentor in academia just yet, she has nevertheless found a way to instill confidence and curiosity in young, aspiring scientists. In her first year, Romero joined Little Librarians, a student organization at UCLA dedicated to teaching STEM to underrepresented students in the Los Angeles area. Seeing the joy in her students’ eyes as she teaches them scientific principles has solidified Romero’s love for helping others. The experience has also been beneficial for Romero, as she has garnered a greater sense of patience and a deeper understanding of the range of knowledge that young scientists possess.

As a first-generation Latina college student, Romero resonated with the students she taught through Little Librarians, and they also helped her combat her feelings of imposter syndrome. Romero entered UCLA in 2020 when classes were fully remote. Naturally, staying focused during classes in her first year was a struggle. Romero faced difficulties in challenging lower division STEM courses while, in her mind, her peers excelled. Romero’s feelings of imposter syndrome were further exacerbated after



hearing some of her peers make comments on how her life science classes were easy. Although she now knows that many students have gone through that same experience, she notes that part of imposter syndrome is feeling like everyone else is succeeding while you're sinking.

Romero also found support throughout her scientific journey via research programs such as the Maximizing Access to Research Careers (MARC) program. MARC is a two-year program funded by the National Institutes of Health that works to diversify the biomedical science field via research training, mentorship, and networking opportunities. The program is aimed at providing training for students from groups who are underrepresented in science, including students who identify as Hispanic/Latiné, who want to pursue a PhD or dual MD/PhD degree. As one of the longest-standing MARC programs in the nation, the program at UCLA is a well-oiled machine, with weekly journal clubs, an extensive scientific network, and abundant support.

The directors and mentors in MARC provide constant support and feedback with applications to other programs, including Romero's manuscript submission to the UCLA USJ. Their willingness to help Romero as she developed her scientific and critical thinking skills painted a picture of an ideal supervisor in Romero's mind, one she aspires to emulate in the future. MARC and the experiences she gained through her research ultimately solidified her passion for the biomedical sciences and her goal of pursuing a PhD. In the future, Romero aims to become a professor running her own parasitology lab and contribute to improving public health in under-resourced communities while serving as a trusted mentor for future generations of scientists.

As Romero reflected on her last year of undergraduate studies at UCLA and her journey as a young biomedical scientist, she emphasized the significance of choosing a lab based on the environment rather than a specific scientific field. Before joining the Hallem Lab, she thought her heart was set on cancer research, but the experiences she gained from stepping outside of her comfort zone introduced her to a new field and helped her shape a different, brighter future. For Romero, UCLA and college in general is a stage where one doesn't have to be committed to one specific research topic or scientific field. Instead, it can be an opportunity to explore, learn, and try things one wouldn't experience otherwise.

Romero concluded, "Choosing the mentorship and the environment over the brand or the specific science is really great because you're going to learn a lot more and have a holistic [experience]. Don't be afraid to do research on something you wouldn't expect to have done because you're going to learn a lot."

Aracely Garcia Romero & Elissa Hallem are authors of "Dopamine Signaling Mediates Skin Penetration by *Strongyloides stercoralis*" on page 68.

Optimizing Ionizable Lipids in Nanoparticles for Human Bronchial Epithelial Cells

Alicia J. Sanoyca¹, Ruth A. Foley², Ruby A. Sims³, Steven J. Jonas³

¹Department of Microbiology, Immunology, and Molecular Genetics, University of California, Los Angeles. ²Department of Bioengineering, University of California, Los Angeles. ³Department of Pediatrics, University of California, Los Angeles.

ABSTRACT

Cystic fibrosis (CF), a monogenic disorder associated with chronic pulmonary infections and reduced lifespans, is a promising target for gene therapy. However, efficient delivery of genetic cargo to airway basal stem cells remains challenging. Lipid nanoparticle (LNP) technologies are a promising method of delivering biomolecular cargo, offering modularity and clinical precedence. This study aimed to optimize the ionizable lipid component of LNPs to achieve maximal cell transfection while maintaining nanoparticle biocompatibility for increased success in clinical applications. LNPs were synthesized with eight different ionizable lipid candidates and were evaluated based on particle size, stability, and transfection ability in an immortalized human bronchial epithelial cell line. Overall, utilizing varying ionizable lipid candidates yielded LNPs with diameters around 200 nm, polydispersity indexes of around 0.2, and mRNA encapsulation efficiencies of around 95%. While LNPs synthesized with the ionizable lipid C12-200 had the highest transfection efficiency (80.5%), its lack of biodegradability *in vivo* led to the selection of Lipid 5 as the best candidate (59.8% transfection). By screening ionizable lipids for delivery to human bronchial epithelial cells, this study contributes to the development of a new scalable and clinically translatable LNP delivery platform tailored for future CF genetic therapies.

INTRODUCTION

Cystic fibrosis (CF) is a monogenic disorder, making it an ideal target for LNP-based gene therapies. The pathology of CF stems from mutations in the cystic fibrosis transmembrane conductance regulator (CFTR) gene that results in disrupted ion transport in epithelial tissues, dehydrated mucus formation, and progressive respiratory injury (1, 2). Current CF treatments include CFTR protein modulators or potentiators; however, patient lifespans remain significantly reduced with a median age of survival between 44 to 53 years (3, 4). Further, roughly 10% of CF patients have mutations not amenable to correction with modulators, with a disproportionate burden on patients from minority backgrounds (5), highlighting the need for mutation-agnostic therapies (6). Current uses of the Clustered Regulatory Interspaced Short Palindromic Repeats (CRISPR)/Cas9 gene editing system in CF treatment still require expensive recurrent treatment (7). CRISPR-based whole-gene insertion into airway basal stem cells would enable permanent correction of the CF phenotype in long-lived progenitor cells (8). An effective CF gene therapy would therefore require reliable and efficient delivery of CRISPR/Cas9 biomolecules to these cells *in vivo*.

Lipid nanoparticle (LNP) technologies are a promising means for delivering biomolecular cargo into cells. The success of COVID-19 vaccines from Pfizer-BioNTech (BNT162b2, Comirnaty®) (9) and Moderna (mRNA-1273, Spikevax®) (10) established the precedent for the large scale clinical deployment of mRNA therapeutics. This study focuses on the optimization of

LNP formulas for the future goal of developing an aerosol-based LNP system to deliver materials to make a site-specific integration of the full CFTR gene (Figure 1). Furthermore, delivery of genetic cargo via nebulized LNPs has been demonstrated (11), but the bioavailability of ionizable lipid components has not been considered, leaving room for improvement regarding biocompatibility *in vivo*.

LNP components include phospholipids, cholesterol, polyethylene glycol (PEG) lipids, and ionizable lipids, which all influence LNP function and structure (12). Phospholipids and cholesterol, which function as helper lipids, improve the encapsulation and cellular delivery of negatively charged genetic material (13). PEG lipids influence nanoparticle structure and stability (14), aggregation, and circulation time *in vivo* (15). This study investigates the role of ionizable lipid moieties, which maximize the encapsulation of negatively charged nucleic acids and facilitate genetic cargo release via endosomal escape (16, 17). Ionizable lipid structure plays an important role in the efficacy of LNP delivery (Table 1). Amine-head groups, for example, undergo protonation from the pH shift caused by the maturation of endosomes to lysosomes, enabling fusion with the lysosomal membrane and subsequent escape (18, 19). Furthermore, ester linkages allow for hydrolysis, triggering self-degradation, nanoparticle collapse, and subsequent cargo delivery (19).

By screening ionizable lipid components, this study aimed to identify LNPs with the highest rates of transfection, or successful mRNA integration into cells, without sacrificing cell viability. LNPs synthesized via hand-mixing underwent initial quality control to

ensure consistent particle sizes and high encapsulation rates to maximize the delivery of genetic cargo. Overall, LNP formulations yielded nanoparticles with diameters on the order of 200 nm, polydispersity indexes (PdIs) ca. 0.2, and mRNA encapsulation efficiencies around 95%. After establishing that ionizable lipid identity influenced transfection rates, LNP formulas were optimized to maximize successful delivery of green fluorescent protein (GFP) mRNA into human basal epithelial cells (HBEs). Low transfection rates and lack of ester linkages, structures linked to biodegradability *in vivo* (20), ruled out some lipids. Lipids associated with the highest transfection rates and biocompatibility included SM-102, Lipid A6, and Lipid 5, which all have similar chemical structures (Table 1). While C12-200 displayed the highest transfection efficiency (80.5%), its lack of biodegradability led to the selection of Lipid 5 as the best candidate, which had a transfection efficiency of 59.8%. The modular nature of LNPs offers optimization avenues for various targets, and this study offers insight into developing an LNP platform tailored for CF gene therapies.

METHODS

Materials

16HBE14o- Human Bronchial Epithelial Cell Line (16HBE), Trypsin-EDTA, L-Glutamine, and human fibronectin were purchased from Millipore Sigma, Sigma-Aldrich (Burlington, MA). Ionizable lipids SM-102, CKK-e12, C12-200, 306Oi10, ALC-0315, Lipid A6, and Lipid 5 were obtained from Echelon Biosciences (Salt Lake City, UT), and OF-02 from MedChem Express (Monmouth Junction, NJ). DOPE, DC-Cholesterol, and DOPE-PEG 1,000 were acquired from Avanti Polar Lipids (Alabaster, AL). Trypan Blue Stain (0.4%), eBioscience™ 7-AAD Viability Staining Solution, and Gibco™ Penicillin-Streptomycin were purchased from Thermo Fisher Scientific (Waltham, MA). CleanCap® Enhanced Green Fluorescent Protein (eGFP) mRNA was purchased from TriLink Biotechnologies, Maravai LifeSciences (San Diego, CA). Minimum Essential Medium Eagle (MEM), with Earle's salts and sodium bicarbonate, without L-glutamine, liquid, sterile-filtered, suitable for cell culture, and PureCol Collagen were obtained from Sigma-Aldrich (Burlington, MA). Bovine Serum Albumin (BSA) Fraction

V was acquired from Roche (Indianapolis, IN). Heat-inactivated Fetal Bovine Serum (FBS) was obtained from Omega Scientific, Inc. (Tarzana, CA).

Cell Culture

E10 cell culturing media was prepared by combining MEM with 10% FBS, 1% penicillin-streptomycin, and 20 mM L-glutamine. Flasks were coated with an extracellular matrix (ECM) mixture composed of α -MEM with 10 μ g/mL human fibronectin, 100 μ g/mL BSA, Fraction V, and 30 μ g/mL PureCol Collagen. 16HBE cells were cultured in E10 at 37°C in ECM-coated flasks. Passages were performed when cells exhibited >80% confluence through incubation with 0.25% Trypsin-EDTA at 37°C for 8 min, then quenched with E10.

LNP Formulation and Characterization

LNPs were synthesized via hand-mixing of an aqueous phase with an organic lipid phase at a flow rate of 3:1. The organic phase consisted of a lipid film resuspended in ethanol to achieve a concentration of 65 mM ionizable amines. Lipid films comprised 50 mol% ionizable lipid, 10 mol% DOPE, 38.5 mol% DC-Cholesterol, and 1.5 mol% DOPE-PEG1k. Ionizable lipids tested included SM-102, CKK-e12, C12-200, 306Oi10, ALC-0315, OF-02, Lipid A6, and Lipid 5. Each ionizable lipid was tested on at least two separate days, with SM-102 held constant among each batch. Following resuspension, the solution was vortexed for 1 min and sonicated for 5 min. The aqueous phase contained eGFP mRNA, a representative reporter cargo for mRNA-based therapeutics, suspended in citric acid buffer (50 mM, pH 4) to maintain a nitrogen to phosphate (N/P) ratio of 7. Mock LNPs were synthesized without mRNA. eGFP mRNA cargo was chosen as a proxy for mRNA therapeutics because it demonstrates the successful delivery of functional mRNA cargo into cells by LNPs. Additionally, GFP is an established reporter system, relatively inexpensive, and readily available. All LNP solutions were diluted 1:3 with phosphate-buffered saline (PBS). Benchmarks for LNP quality included diameters below 400 nm, PdI values below 0.3, and encapsulation efficiency of eGFP mRNA above 80%.

A 1:300 LNP:PBS solution was used for dynamic light scattering

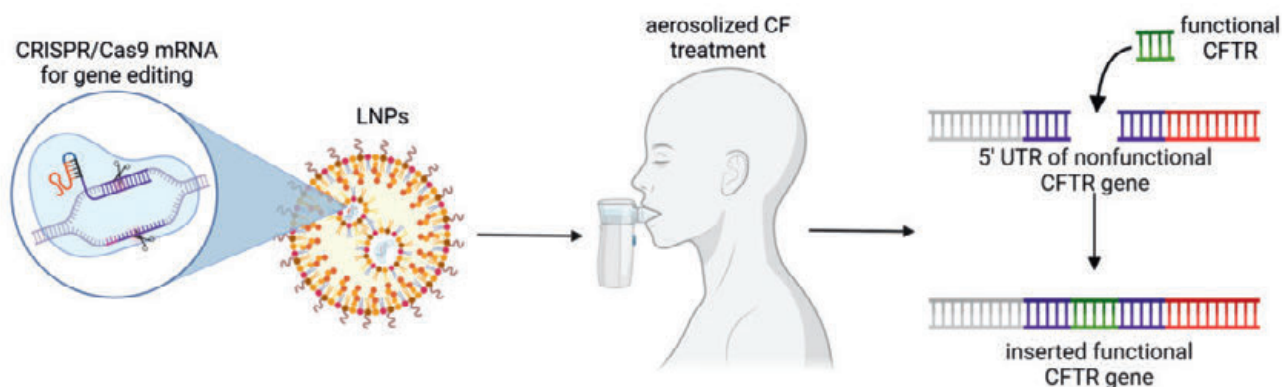


Figure 1: Schematic diagram of the proposed design of aerosolized cystic fibrosis (CF) treatment.

Lipid nanoparticles (LNPs) containing mRNA that encode for the Cas9 nuclease of the Clustered Regulatory Interspaced Short Palindromic Repeats (CRISPR) system and a template of the functional cystic fibrosis transmembrane regulator (CFTR) gene will be introduced to patients as a nebulized treatment. Upon reaching the target cell's surface, the LNPs will be taken up and undergo endosomal escape to release the genetic cargo into the cytosol. There, the cell's internal machinery will use the mRNA to synthesize the necessary components of the CRISPR/Cas9 system. The CRISPR/Cas9 system will then make a targeted insertion of the CFTR gene in the 5' untranslated region (UTR) of the patient's nonfunctional CFTR gene.

(DLS) analysis to quantify diameter and polydispersity (21). For DLS analysis, samples were analyzed using a Malvern Zetasizer at the Nano and Pico Characterization Lab at the California NanoSystems Institute. The diameter of LNPs was measured as a Z-average (Z-avg) score, indicating the intensity weighted mean of particle distribution, and polydispersity was quantified by PdI, denoting the normalized width of the Gaussian distribution (22). Two rounds of five-measurement averages were collected for each sample. The Quant-iT™ RiboGreen™ RNA Assay (Invitrogen) was used to evaluate the percentage of mRNA successfully taken into the LNPs, or encapsulation efficiency. RiboGreen measurements were taken on a Varioskan LUX Multimode Microplate Reader and data was collected via SkanIt Microplate Reader Software.

All results were processed and analyzed using GraphPad Prism. A Shapiro-Wilk test ($\alpha=0.05$) confirmed the normality of distribution among diameters and PdIs of the different ionizable lipids. Brown-Forsythe and Welch ANOVA tests ($\alpha=0.05$) were used to evaluate differences in diameter and PdI values among the lipid panel ($\alpha=0.05$), and a Dunnett's T3 multiple comparisons test ($\alpha=0.05$) was run to determine the relationships between ionizable lipid pairs. Differences between encapsulation efficiency means were evaluated using a Kruskal-Wallis ANOVA test ($\alpha=0.05$).

Cell Plating and Treatment

16HBEs cultured in flasks underwent a 2x PBS rinse before being trypsinized with 0.25% trypsin-EDTA for 8 min at 37°C. A Countess II FL Automatic Cell Counter from Invitrogen, Thermo Fisher Scientific was used to determine the concentration of the solution, and an average of two measurements was used in further calculations for seeding well plates. 16HBEs were seeded in 96-well plates coated with an extracellular polymeric substance (EPS) matrix at a concentration of 20,000 cells per well and a volume of 100 μ L per well. For each ionizable lipid being tested, three wells were seeded for the experimental group and three wells were seeded for the mock LNP group. An additional three wells were seeded every round for the untreated control group, which would not be exposed to LNPs. The plate was then incubated at 37°C for one day before being treated with LNPs.

One day following initial plating, the old E10 was removed from each well and replaced with 100 μ L of fresh E10. Each well was then treated with 50 μ L of a solution made from 2.29 μ L LNP solution and 197.7 μ L PBS to achieve a final GFP concentration of 1 ng/ μ L. Cells were incubated for 24 hours before GFP expression analysis.

Flow Cytometry

Expression of GFP by cells was measured one day after treatment through Flow Cytometry. Cells were detached from well plates using 0.25% Trypsin-EDTA, quenched with E10, and then spun down at a relative centrifugal force (RCF) of 500 for 5 min. The supernatant was removed, and cells were resuspended in 200 μ L flow buffer, which was produced by mixing 1x PBS with 20% E10 medium. 7-AAD dye was added to each sample before they were passed through filtered-cap flow cytometry tubes. The tubes were then placed on ice until being run on a BD Biosciences LSR II at the UCLA Broad Stem Cell Research Center Flow Cytometry Core. Data collected was processed on FlowJo and plotted using GraphPad Prism.

All GFP fluorescence measurements were compared to mock and untreated cells, as dead cells exhibit slight autofluorescence

Ionizable Lipid	Structure
SM-102	
Lipid 5	
ALC-0315	
Lipid A6	
C12-200	
CKK-e12	
OF-02	
306Oi10	

Table 1: Structures of ionizable lipid candidates.

Amine head groups, indicated by blue boxes, play a significant role in mRNA delivery. Ester linkages, indicated by red boxes, allow for hydrolysis and subsequent cargo delivery. Ionizable lipids SM-102 and Lipid 5 have nearly identical structures, differing only in the placement of one ester linkage, and ALC-0315 contains an additional hydrocarbon chain. Lipid A6 is the only ionizable lipid with a triple bond within its hydrocarbon chain. Ionizable lipids C12-200, CKK-e12, and OF-02 all lack ester linkages, contain a central ring structure, and possess higher numbers of amine groups compared to other candidates. Lipid 306Oi10 contains the highest combined number of amines and ester linkages with three and four groups, respectively.

(23). All results were processed and analyzed using GraphPad Prism. A Shapiro-Wilk test ($\alpha=0.05$) confirmed the normality of distribution. When applicable, results were confirmed with a Kolmogorov-Smirnov test ($\alpha=0.05$). Brown-Forsythe and Welch's ANOVA tests were used to evaluate statistical differences among means ($\alpha=0.05$), and a Dunnett's T3 multiple comparisons test ($\alpha=0.05$) was run to determine the relationships between ionizable lipid pairs.

Fluorescence Microscopy

One day after treating the cells, an Echo Revolve Microscope was used to take fluorescence microscopy images of each well at 4x and 10x magnifications. Brightfield images of the cells and their fluorescence were taken and overlaid to depict which cells expressed GFP. For each well, one 4x and two 10x images were taken of randomly selected regions with >60% confluence.

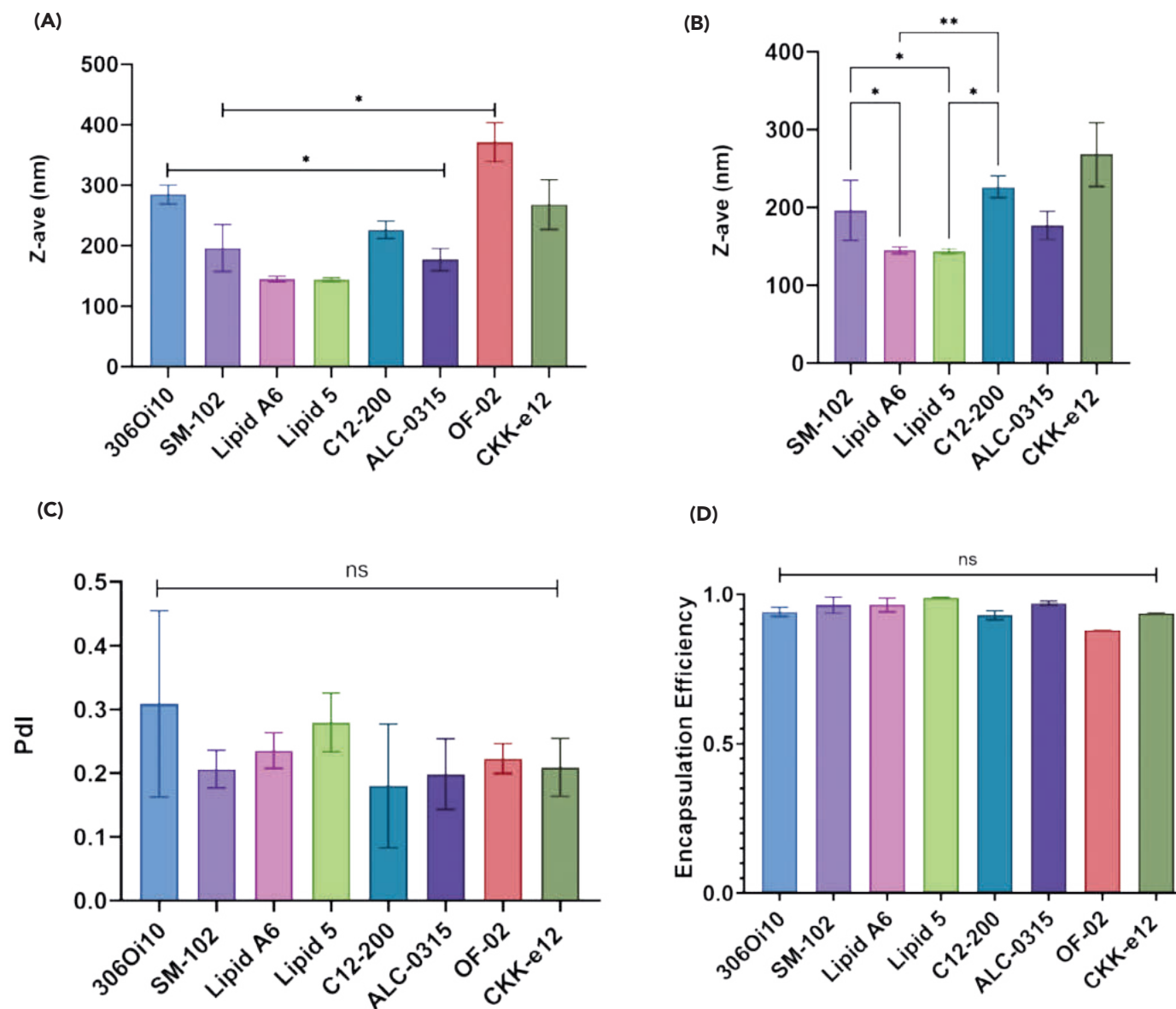


Figure 2: The impact of ionizable lipids on LNP morphology.

Liquid nanoparticles formulated with one of eight ionizable lipid candidates were synthesized via hand mixing and evaluated in terms of particle size, polydispersity, and encapsulation efficiency. Means of two or more biological replicates were plotted with standard deviations. Unbound lines represent comparisons of all ionizable lipids with each other via Brown-Forsythe and Welch's ANOVA test ($\alpha=0.05$), and bound lines indicate pairwise comparisons of the outermost lipids. Asterisks indicate the statistical significance of Dunnett's T3 multiple comparisons test ($\alpha=0.05$), one or two stars representing $p<0.05$ and $p<0.01$ respectively, and ns denoting not statistically significant. **(A)** The mean diameters (Z-ave) of the ionizable lipid panel show statistically significant differences, suggesting a link between lipid choice and diameter. **(B)** Pairwise comparisons of a subsection of the lipid panel are highlighted. **(C)** The mean Polydispersity Index (Pdl) values and **(D)** mean encapsulation efficiencies, measured by fluorescence-based RiboGreen encapsulation assays, do not show a dependence on ionizable lipid choice.

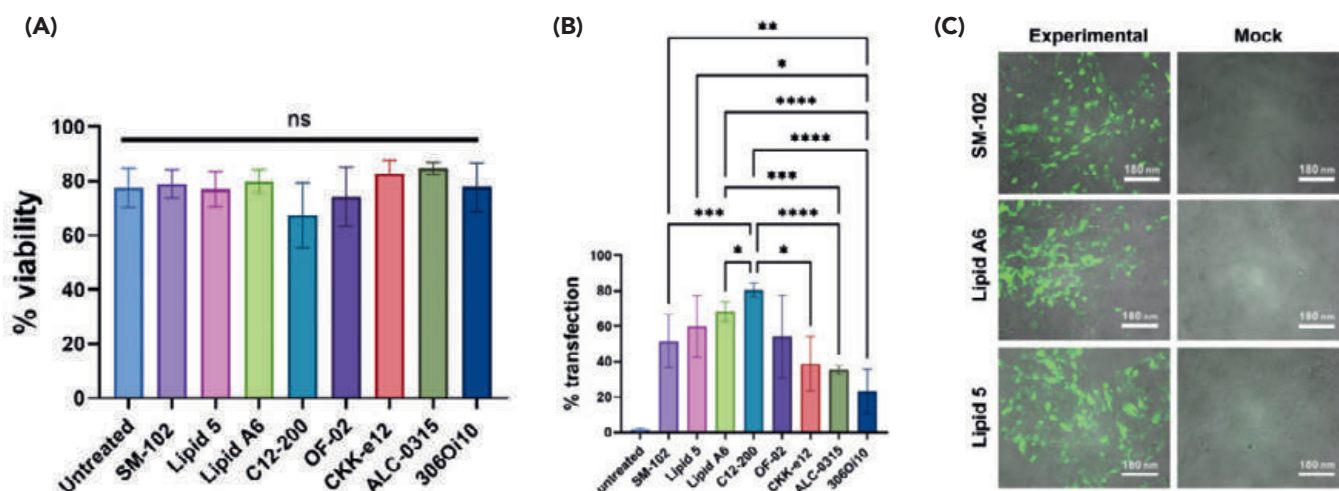


Figure 3: Impact of ionizable lipids on cell viability and LNP transfection efficiency.

LNP transfection of 16HBE14o- Human Bronchial Epithelial Cells (16HBEs) was quantified using green fluorescent protein (GFP) expression through flow cytometry and fluorescence microscopy. **(A)** The mean viabilities, or percent of single cells that are alive, are plotted with standard deviations. None of the viabilities were statistically significantly different from one another. **(B)** The mean transfection levels, or percent of live cells with GFP expression, are plotted with standard deviations, showing the impact of ionizable lipid choice. Bound lines indicate pairwise comparisons of the outermost lipids. Asterisks indicate the statistical significance of Dunnett's T3 multiple comparisons test ($\alpha=0.05$), one to four stars representing $p<0.05$, 0.01, 0.001, and 0.0001 respectively. The untreated control is included but was not used for statistical analysis. **(C)** Fluorescence microscopy images overlaid on brightfield images of HBEs treated with mock and experimental LNPs. Scale bars 180 nm.

RESULTS

Ionizable Lipid Choice Affects LNP Size

The diameters of lipids 306Oi10 (284.2 nm) and OF-02 (371.7 nm) were both statistically significantly larger than SM-102 (196.5 nm), Lipid A6 (145.3 nm), Lipid 5 (144.3 nm), C12-200 (226.7 nm), and ALC-0315 (177.3 nm) with a p -value of at least $p<0.05$ (Figure 2A). The diameter of CKK-e12 was not statistically significantly different from any other lipid. The diameter of SM-102 was statistically significantly larger than Lipid A6 and Lipid 5 (both $p=0.0389$). There was no significant difference between the diameters of ALC-0315, Lipid A6, and Lipid 5. Lipid 5 had the smallest coefficient of variation at 1.9%, followed by Lipid A6 at 2.9%. All other coefficients of variation were between 5% and 20%, with the highest being SM-102 at 19.5% (Figure 2B).

There was no statistically significant difference among mean PDI values ($p=0.2642$ for Brown-Forsythe ANOVA test and $p=0.3216$ for Welch's ANOVA test). PDI values ranged from a low of 0.18, associated with C12-200, to a high of 0.31, associated with 306Oi10. 306Oi10 and C12-200 had the largest coefficients of variation, with 47.2% and 53.7% respectively (Figure 2C). There was no statistically significant difference among the mean encapsulation efficiency values of any ionizable lipids ($p=0.0958$). Encapsulation efficiencies ranged from a low of 88%, associated with OF-02, to a high of 99%, associated with Lipid 5 (Figure 2D).

Flow Cytometry Reveals Ionizable Lipid Choice Affects Transfection of 16HBEs with LNPs

No statistically significant difference was observed among cell viabilities. C12-200 had the lowest percent viability at 67.4%, followed by OF-02 at 74.1%. The cells not treated with LNPs had a percent viability of 77.5%. Cells treated with LNPs synthesized with OF-02 and C12-200 had the highest coefficient of variations

at 14.8% and 18.0% respectively. Cells treated with all other conditions showed coefficients of variation between 2% and 9% (Figure 3A).

A statistically significant difference was observed among mean GFP expression levels ($p<0.0001$). C12-200 had statistically significantly higher GFP expression than SM-102 ($p=0.0003$), CKK-e12 ($p=0.0103$), 306Oi10 ($p<0.0001$), ALC-0315 ($p<0.0001$), and Lipid A6 ($p=0.0378$). C12-200 had 80.5% transfection, SM-102 had 51.7%, CKK-e12 had 38.8%, 306Oi10 had 23.3%, ALC-0315 had 35.4%, and Lipid A6 had 68.5%. Compared to C12-200, the only ionizable lipid with no statistically significant difference in eGFP expression was Lipid 5, which had a mean transfection of 59.8%. Cells treated with Lipid A6 did not have statistically significantly higher GFP expression in comparison to cells treated with SM-102 or Lipid 5 LNPs. Overall, cells treated with 306Oi10 and ALC-0315 LNPs had significantly lower GFP expression, while cells treated with C12-200 LNPs had the highest transfection rates. Cells treated with C12-200 LNPs had the lowest coefficient of variation at 5.1%, followed by ALC-0315 and Lipid A6 LNPs at 7.3% and 8.1% respectively. The cells treated with LNPs synthesized with the remaining ionizable lipids had higher variances of above 29% (Figure 3B).

Fluorescence Microscopy Reveals Successful Transfection of 16HBEs with LNPs

Each of the ionizable lipid candidates expressed GFP fluorescence that aligned with cell borders, suggesting successful transduction of cells (Figure 3C). Mock and untreated cells were also imaged as controls, which showed little to no fluorescence.

DISCUSSION

Substitution of different ionizable lipids did not significantly impact the encapsulation efficiency or PDI of LNPs (Figures

2C, 2D). Diameter, however, was impacted as 306Oi10 and OF-02 LNPs exhibited with significantly larger diameters than the other tested lipids, ruling these candidates out for ionizable lipid selection (Figure 2A). Clathrin-mediated endocytosis, a mechanism of LNP uptake by cells, has been shown to have an upper limit of 200-300 nm, with smaller nanoparticles showing increased cellular uptake (24). Size restrictions for endocytic uptake into cells necessitate investigation into optimizing LNP formulas to ensure consistent production of the smallest LNP diameters. Overall, the smallest LNPs were generated by ALC-0315, Lipid A6, and Lipid 5, among which there was no statistically significant difference in size (Figure 2B).

Because cell viability did not exhibit statistically significant change compared to the untreated controls, cell death was not correlated with LNP treatment (Figure 3A). Therefore, transfection efficiency was the main metric for determining which ionizable lipid would be favored in future LNP formulations. The goal was to design a delivery vehicle that would have the highest efficacy *in vivo*, focusing on high transfection ability so fewer LNPs would need to be synthesized and delivered to patients, reducing costs and manufacturing burdens. Fluorescent microscopy provided visual confirmation that LNPs were able to successfully transfect 16HBEs, as the cells were able to internalize and express the encapsulated eGFP mRNA (Figure 3C). Flow cytometry analysis revealed that C12-200 LNPs displayed the highest transfection based on percent GFP expression in single, live cells (Figure 3B). However, further considerations were made before determining the best ionizable lipid candidate.

Biodegradability *in vivo* is important to ensure that LNP components are not circulating within the body for long periods after performing their intended function, potentially triggering a prolonged immune response (25). One factor affecting biodegradability is the presence of ester linkages within lipid structures (20). Studies comparing more bioavailable ionizable lipids, such as 306Oi10, to C12-200 have shown decreased immune activation *in vivo* for ionizable lipids that contain multiple ester linkages (26). Ester linkages are chemically stable at physiological pH but can be hydrolyzed by esterase or lipase when present in tissues or cells (27, 28). Cleavage of ester linkages results in hydrophilic products more readily degraded within physiological conditions, reducing the circulation time of LNP components following the successful delivery of genetic cargo (28). Of the screened ionizable lipids, C12-200, CKK-e12, and OF-02 do not contain degradable ester linkages (Table 1). Due to concerns regarding potential immune system stimulation *in vivo* (25), C12-200 would not be recommended for use in clinical applications despite the high associated transfection ability, prompting considerations of the next best lipids.

Focusing on ionizable lipids with ester linkages, flow cytometry revealed that some candidates exhibited transfection efficiencies on par with the C12-200 LNPs. In particular, Lipid 5 prevailed as a strong candidate for ionizable lipid selection because Lipid 5 LNPs did not have a statistically significantly lower transfection efficiency than C12-200 LNPs (Figure 3B), and Lipid 5 contains two ester linkages (Table 1). SM-102, the ionizable lipid with clinical precedence in Moderna's COVID-19 vaccine (29), has almost an almost identical structure to Lipid 5, differing only in the placement of one ester linkage (Table 1). Furthermore, cytotoxicity tests evaluating Lipid 5 have shown minimal immune activation and rapid lipid clearing from tissue (30). These

favorable characteristics made Lipid 5 a promising ionizable lipid candidate, as LNP formulations incorporating it offer adequate cell transfection with advantageous features such as increased bioavailability and minimal cytotoxicity.

Limitations of this study included small sample size, as most lipids only contained two biological replicates which were three technical replicates each. Small sample sizes resulted in high standard deviations of measurements, which affected statistical significance testing. Furthermore, hand mixing introduced variability in lipid quality that may have affected diameter and PDI values. Thus, future experiments will utilize microfluidic chip mixing which will ensure sustained flow rates, decreasing particle diameters and PDIs (31).

CONCLUSION

The goal of this undergraduate research project was to screen ionizable lipid components and evaluate which candidates would yield LNPs with the highest transfection while maintaining particle integrity and cell viability. It was observed that Lipid 5 was the best candidate for maximizing LNP transfection efficiency while maintaining biodegradability *in vivo* through the inclusion of ester linkages.

Current LNP delivery systems that target lung epithelia include selective organ targeting (SORT) nanoparticles, but mediation of CRISPR-based whole-gene insertion is yet to be achieved (32). Aerosol-based delivery would directly deposit gene editing molecules to the airway epithelium, limiting off-target editing in comparison to systemic delivery; however, the destructive nebulization may cause damage to sensitive cargoes (33). High PEG concentrations and sitosterol have shown increased aerosol stability and transfection ability (34). Future directions include optimization of the other components of LNP formulation, including cholesterol and PEG-lipid constituents. Once the optimal LNP formulations are identified, the effects of LNP nebulization will be studied to determine particle stability during aerosolization. Air-liquid interface (ALI) cultures will enable direct testing of nebulized LNP suspensions. While delivery of genetic cargo via nebulized LNPs had been demonstrated (11), the bioavailability of ionizable lipid components had not been considered. By accounting for biodegradability in ionizable lipid selection, this project offers alternative LNP formulations that can be tested in *in vivo* systems.

Furthermore, site-specific integration of the full CFTR gene has not yet been achieved, and targeting specific progenitor cell populations remains a challenge. The overarching goal is to design a nebulized gene therapy solution where a functional CFTR gene is inserted at the 5' untranslated region of a CF patient's dysfunctional CFTR gene (Figure 1). Future experiments will transition from eGFP-encoding mRNA cargoes to CRISPR/Cas9 gene editing reagents, as the end goal is to develop an optimized vehicle for the delivery of therapeutic gene editing cargo for the treatment of CF.

ACKNOWLEDGMENTS

I acknowledge the Nano and Pico Characterization Lab at the California NanoSystems Institute, and the Eli and Edythe Broad Center of Regenerative Medicine and Stem Cell Research UCLA Flow Cytometry Core Resource. Funding was provided by the National Institutes of Health (NIH) Common Fund through an NIH Director's Early Independence Award co-funded by the National

Institute of Dental and Craniofacial Research and Office of the Director, NIH Grant DP5OD028181 (S.J.J.); the Cystic Fibrosis Foundation, Grant JONAS20XX0; and the Cystic Fibrosis Research Institute New Horizons Award program. A.S., R.A.F., R.A.S., and S.J.J. do not have any conflicts of interest.

EDITORS

This article was received by Archi Patel, Cecilia McCormick, Ethan Hung, Jessica Goeij, and Summer Kelso, edited by Ruthi Shin and Tanisha Lakhanpal, and laid out by Zenya Bian.

REFERENCES

1. A. L. Cooney, P. B. McCray, P. L. Sinn, Cystic Fibrosis Gene Therapy: Looking Back, Looking Forward. *Genes*. **9** (2018). doi: 10.3390/genes9110538.
2. A. Berical *et al.*, Challenges Facing Airway Epithelial Cell-Based Therapy for Cystic Fibrosis. *Front Pharmacol.* **10**, 74 (2019). doi: 10.3389/fphar.2019.00074.
3. R. H. Keogh, S. Stanojevic, A guide to interpreting estimated median age of survival in cystic fibrosis patient registry reports. *J. Cyst. Fibros.* **17**, 213–217 (2018). doi: 10.1016/j.jcf.2017.11.014.
4. V. Scotet, C. LHostis, C. Férec, The Changing Epidemiology of Cystic Fibrosis: Incidence, Survival and Impact of the CFTR Gene Discovery. *Genes*. **11**, 589 (2020). doi: 10.3390/genes11060589.
5. M. E. McGarry, S. A. McColley, Cystic Fibrosis Patients of Minority Race and Ethnicity Less Likely Eligible for CFTR Modulators Based on CFTR Genotype. *Pediatr. Pulmonol.* **56**, 1496–1503 (2021). doi: 10.1002/ppul.25285.
6. E. Kramer-Golinkoff, A. Camacho, L. Kramer, J. L. Taylor-Cousar, A survey: Understanding the health and perspectives of people with CF not benefiting from CFTR modulators. *Pediatr. Pulmonol.* **57**, 1253–1261 (2022). doi: 10.1002/ppul.25859.
7. C. Graham, S. Hart, CRISPR/Cas9 gene editing therapies for cystic fibrosis. *Expert Opin. Biol. Th.* **21**, 767–780 (2021). doi: 10.1080/14712598.2021.1869208.
8. A. Akinc *et al.*, Targeted delivery of RNAi therapeutics with endogenous and exogenous ligand-based mechanisms. *Mol. Ther.* **18**, 1357–1364 (2010). doi: 10.1038/mt.2010.85.
9. F. P. Polack *et al.*, Safety and Efficacy of the BNT162b2 mRNA Covid-19 Vaccine. *New Engl. J. Med.* **383**, 2603–2615 (2020). doi: 10.1056/NEJMoa2034577.
10. L. R. Baden *et al.*, Efficacy and Safety of the mRNA-1273 SARS-CoV-2 Vaccine. *New Engl. J. Med.* **384**, 403–416 (2021). doi: 10.1056/NEJMoa2035389.
11. A. Y. Jiang *et al.*, Combinatorial development of nebulized mRNA delivery formulations for the lungs. *Nat. Nanotechnol.* Epub ahead of print. PMID: 37985700. (2023). doi: 10.1038/s41565-023-01548-3.
12. C. H. Albertsen, J. A. Kulkarni, D. Witzigmann, M. Lind, K. Petersson, J. B. Simonsen, The role of lipid components in lipid nanoparticles for vaccines and gene therapy. *Adv. Drug Deliv. Rev.* **188**, 114416 (2022). doi: 10.1016/j.addr.2022.114416.
13. J. A. Kulkarni, D. Witzigmann, J. Leung, Y. Y. C. Tam, P. R. Cullis, On the role of helper lipids in lipid nanoparticle formulations of siRNA. *Nanoscale*. **11**, 21733–21739 (2019). doi: 10.1039/c9nr09347h.
14. K. J. Kauffman *et al.*, Optimization of Lipid Nanoparticle Formulations for mRNA Delivery in Vivo with Fractional Factorial and Definitive Screening Designs. *Nano Lett.* **15**, 7300–7306 (2015). doi: 10.1021/acs.nanolett.5b02497.
15. T. Suzuki *et al.*, PEG shedding-rate-dependent blood clearance of PEGylated lipid nanoparticles in mice: Faster PEG shedding attenuates anti-PEG IgM production. *Int. J. Pharm.* **588**, 119792 (2020). doi: 10.1016/j.ijpharm.2020.119792.
16. K. A. Hajj, K. A. Whitehead, Tools for translation: non-viral materials for therapeutic mRNA delivery. *Nat. Rev. Mater.* **2**, 1–17 (2017). doi: 10.1038/natrevmats.2017.56.
17. M. Schlich *et al.*, Cytosolic delivery of nucleic acids: The case of ionizable lipid nanoparticles. *Bioeng. Transl. Med.* **6**, e10213 (2021). doi: 10.1002/btm2.10213.
18. F. Ding, H. Zhang, J. Cui, Q. Li, C. Yang, Boosting ionizable lipid nanoparticle-mediated in vivo mRNA delivery through optimization of lipid amine-head groups. *Biomater. Sci.* **9**, 7534–7546 (2021). doi: 10.1039/D1BM00866H.
19. H. Tanaka *et al.*, Self-Degradable Lipid-Like Materials Based on “Hydrolysis accelerated by the intra-Particle Enrichment of Reactant (HyPER)” for Messenger RNA Delivery. *Adv. Funct. Mater.* **30**, 1910575 (2020). doi: 10.1002/adfm.201910575.
20. M. A. Maier *et al.*, Biodegradable Lipids Enabling Rapidly Eliminated Lipid Nanoparticles for Systemic Delivery of RNAi Therapeutics. *Mol. Ther.* **21**, 1570–1578 (2013). doi: 10.1038/mt.2013.124.
21. F. Babick, “Dynamic light scattering (DLS)” in *Characterization of Nanoparticles: Measurement Processes for Nanoparticles*, (Elsevier, 2020), pp. 137–172.
22. R. Ragheb, U. Nobbmann, Multiple scattering effects on intercept, size, polydispersity index, and intensity for parallel (VV) and perpendicular (VH) polarization detection in photon correlation spectroscopy. *Sci. Rep.* **10**, 21768 (2020). doi: 10.1038/s41598-020-78872-4.
23. A. A. Kozlova, R. A. Verkhovskii, A. V. Ermakov, D. N. Bratashov, Changes in Autofluorescence Level of Live and Dead Cells for Mouse Cell Lines. *J. Fluoresc.* **30**, 1483–1489 (2020). doi: 10.1007/s10895-020-02611-1.
24. M. S. de Almeida, E. Susnik, B. Drasler, P. Taladriz-Blanco, A. Petri-Fink, B. Rothen-Rutishauser, Understanding nanoparticle endocytosis to improve targeting strategies in nanomedicine. *Chem. Soc. Rev.* **50**, 5397–5434 (2021). doi: 10.1039/d0cs01127d.
25. K. A. Whitehead *et al.*, Degradable lipid nanoparticles with predictable in vivo siRNA delivery activity. *Nat. Commun.* **5**, 4277 (2014). doi: 10.1038/ncomms5277.
26. A. Khalid *et al.*, A Potent Branched-Tail Lipid Nanoparticle Enables Multiplexed mRNA Delivery and Gene Editing In Vivo. *Nano Lett.* **20**, 5167–5175 (2020). doi: 10.1021/acs.nanolett.0c00596.
27. D. Gilham, R. Lehner, Techniques to measure lipase and esterase activity in vitro. *Methods* **36**, 139–147 (2005). doi: 10.1016/j.ymeth.2004.11.003.
28. H. Wong, M. C. Schotz, The lipase gene family. *J. Lipid Res.* **43**, 993–999 (2002). doi: 10.1194/jlr.r200007-jlr200.
29. L. Zhang *et al.*, Effect of mRNA-LNP components of two globally-marketed COVID-19 vaccines on efficacy and stability. *npj Vaccines*. **8**, 1–14 (2023). doi: 10.1038/s41541-023-00751-6.
30. S. Sabnis *et al.*, A Novel Amino Lipid Series for mRNA Delivery: Improved Endosomal Escape and Sustained Pharmacology and Safety in Non-human Primates. *Mol. Ther.* **26**, 1509–1519 (2018). doi: 10.1016/j.ymthe.2018.03.010.
31. D. M. S. Petersen, N. Chaudhary, M. L. Arral, R. M. Weiss, K. A. Whitehead, The mixing method used to formulate lipid nanoparticles affects mRNA delivery efficacy and organ tropism. *Eur. J. Pharm. Biopharm.* **192**, 126–135 (2023). doi: 10.1016/j.ejpb.2023.10.006.
32. Q. Cheng *et al.*, Selective organ targeting (SORT) nanoparticles for tissue-specific mRNA delivery and CRISPR-Cas gene editing. *Nat. Nanotechnol.* **15**, 313–320 (2020). doi: 10.1038/s41565-020-0669-6.
33. H. Zhang, J. Leal, M. R. Soto, H. D. C. Smyth, D. Ghosh, Aerosolizable Lipid Nanoparticles for Pulmonary Delivery of mRNA through Design of Experiments. *Pharmaceutics* **12**, 1042 (2020). doi: 10.3390/pharmaceutics12111042.
34. J. Kim *et al.*, Engineering Lipid Nanoparticles for Enhanced Intracellular Delivery of mRNA through Inhalation. *ACS Nano*. **16**, 14792–14806 (2022). doi: 10.1021/acsnano.2c05647.

Production and Growth of CAR-NK Cells to Treat HIV Infection

Vincent Le¹, Anjie Zhen¹

¹Department of Medicine, David Geffen School of Medicine.

ABSTRACT

The ability of natural killer (NK) cells to destroy virally infected cells makes them a viable option for treating human immunodeficiency virus (HIV). Cell therapy through NK cells is of significant interest because NK cells do not require human leukocyte antigen (HLA) matching, making it possible to use NK cells to produce a readily available treatment. Chimeric antigen receptors (CAR) are synthetic receptors that can engineer immune cells to recognize and bind to specific antigens. This paper aims to investigate the potential of chimeric antigen receptor natural killer (CAR-NK) therapy as a potential cure for HIV. An optimized CAR lentivirus, named D1D2-CAR-41BB, can effectively kill HIV-infected cells. D1D2-CAR-41BB is used to investigate the growth and functional ability of CAR-NK cells. The methods involved producing CAR lentivirus, expanding and maintaining NK cell cultures, transducing NK cells with CAR lentivirus, and performing cytokine assays to assess CAR-NK functionality. The experiments demonstrated that functional CAR-NK cells can be produced from healthy donors' peripheral blood mononuclear cells (PBMC) by culturing them in NK cell expansion media with cytokines. The experiments compared two culture media and found that the Miltenyi Biotec NK MACS Medium significantly outperformed the ImmunoCult NK cell expansion kit in inducing primary NK cell proliferation and lentiviral transduction. The successfully transduced and expanded NK cells secrete IFN- γ when co-incubated with HIV envelope positive expression cells, indicating potential therapeutic use against HIV. To further optimize CAR-NK function, future experiments should involve the use of stimulators of interferon genes protein (STING) agonists to promote stronger immune responses against HIV by activating the STING pathway. This paper aims to give insights and further the developments in cell and gene therapy for the treatment of HIV.

INTRODUCTION

Human immunodeficiency virus (HIV) is a retrovirus that disrupts the biological mechanisms of the body's immune cells by targeting CD4⁺ T cells, which are important for fighting diseases and infections. HIV binds to CD4⁺ T cells and destroys them, leading to acquired immunodeficiency syndrome (AIDS) (1). Despite the development of antiretroviral therapies that mitigate the effects of HIV infection, HIV remains prevalent globally as there is no cure for the disease (2).

Current efforts to combat HIV involve chimeric antigen receptors (CAR). CARs are created in the lab to engineer immune cells that combat specific antigens, such as HIV (3). The CAR viral vectors are packaged into lentiviruses and inserted into the genomes of desired immune cells, which then recognize and bind to cells that present the target antigens. The Zhen Lab at the UCLA AIDS Institute optimized a chimeric antigen receptor lentivirus, named D1D2-CAR-41BB, that can kill HIV-infected cells in animal models and be used with natural killer (NK) cells to develop a potential cure for HIV (Figure 1) (4). D1D2-CAR-41BB is a truncated variant of the full-length CD4 CAR. It does not interact non-specifically with Interleukin 16 (IL-16) and does not mediate HIV infection by CD4.

NK cells are white blood cells in the innate immune system that are crucial to killing virally infected and tumorigenic

cells. NK cells can eliminate infected cells through direct cell cytotoxicity or the production of pro-inflammatory cytokines, including interferon-gamma (IFN- γ) (5). CD107a is a distinctive degranulation marker for NK cells and acts as an indirect measure of cytotoxic activity (6). CD56 is a phenotypic marker for NK cells (7) and interleukin 2 (IL-2) is an important cytokine that stimulates the proliferation of NK cells (8). Engineering NK cells is of particular interest due to their ability to recognize and eliminate virally infected cells even without previous exposure to the virus.

Chimeric antigen receptor natural killer (CAR-NK) cells are engineered NK cells that express CAR through genetic modification. CAR-NK cell therapy presents potential advantages over other CAR cell therapies due to its improved safety in both autologous and allogeneic settings, along with multiple mechanisms of activating cytotoxicity (9). Moreover, stimulators of interferon genes protein (STING) agonists like cyclic guanosine adenosine monophosphate (cGAMP) were found to effectively enhance CAR-NK cell function against pancreatic cancer (10). These findings suggest STING agonists may enhance the functionality of CAR-NK cells against HIV. BDW is a recently discovered STING agonist that is structurally different from cGAMP. BDW's binding mechanism allows it to work on the natural STING 230A variant, whereas cGAMP works on both wild-type STING and STING 230A (11). Currently, the furthest developments of CAR-NK

cell therapies are in the clinical trial phase for the treatment of hematological malignancies and tumors (12). HIV is a reasonable extension of the ongoing research for CAR-NK therapy because HIV has distinct markers that are identifiable by an anti-HIV CAR inserted in NK cells, similar to how CAR-NK cells are engineered to recognize and eliminate cells with tumor markers.

Current HIV treatments require lifelong antiretroviral medication use, which only inhibits HIV activation and replication. CAR-NK cell therapy can offer a viable approach to cure HIV by directly targeting and eradicating HIV-infected cells, eliminating the lifelong need for HIV medication. Furthermore, CAR-NK cell therapy does not require human leukocyte antigens (HLA) matching, a process where cell antigens must align between a donor and recipient for a transplant to occur. This allows CAR-NK cell therapy to be an accessible product and eliminate the one-donor, one-patient limitation (13). This paper aims to advance CAR-NK cell therapy as a cure for HIV by investigating its feasibility (Figure 2). This paper hypothesizes that functional CAR-NK cells can be produced from primary healthy donors' peripheral blood mononuclear cells (PBMCs) by culturing PBMCs in NK cell expansion media with cytokines.

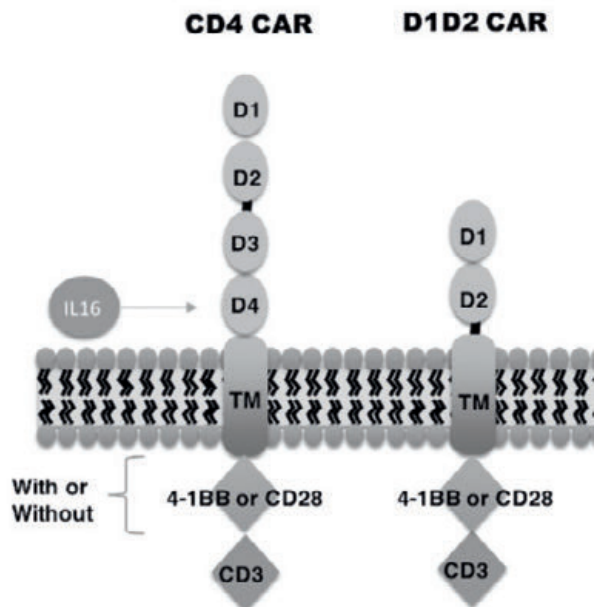


Figure 1: Comparison of CD4 Chimeric Antigen Receptor (CAR) and D1D2-CAR-41BB molecules.

A schematic review of CD4CAR and truncated D1D2-CAR-41BB molecules is shown. The CD4CAR will be present on the immune cell membrane after the genome has been inserted. The truncated D1D2-CAR-41BB is an optimized variant of the full-length CD4CAR which does not interact non-specifically with IL16 and does not mediate human immunodeficiency virus (HIV) infection by CD4. The D1D2-CAR-41BB was shown to more effectively suppress HIV infection *in vivo*. This figure was adapted from a publication by A. Zhen *et al.*, with authorized permission for its utilization (4).

METHODS

Lentivirus Production

The GFP control vector and CAR vectors, which are both lentivirus-based, were produced in 293FT cells using the Lipofectamine 2000 reagent (Invitrogen). The 293FT cells were co-transfected with

CAR vectors that include pCMVΔR8.2Δvpr packaging construct and the pCMV-VSV-G envelope protein plasmid. This process was done to produce more lentiviral vectors that would be later used to transduce NK cells. The supernatant was collected from 293FT cells 48 hours after transfection, filtered using a 0.45 μm sterile filter, and concentrated by ultracentrifugation using a Beckman SW32 rotor at 30,000 rpm at 4°C. The medium was aspirated and the pellet was resuspended with PBS and stored at -80°C.

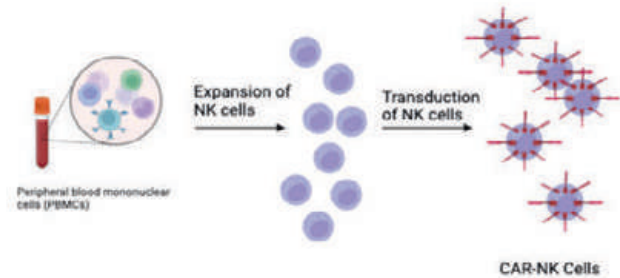


Figure 2: Experimental design for the production of chimeric antigen receptor natural killer (CAR-NK) cells from peripheral blood mononuclear cells (PBMCs).

PBMCs are obtained from a healthy donor and expanded. Insertion of a D1D2-CAR-41BB lentivirus facilitates transduction into CAR-NK cells.

NK Cell Expansion and Transduction

In the initial trial to optimize media selection for NK cell expansion, 500,000 fresh PBMCs from donors were cultured in the NK MACS Basal medium (Miltenyi Biotec) and ImmunoCult NK Cell Basal Medium (STEMCELL technologies) with recombinant human IL-2. To determine the optimal cytokine concentration that would enhance NK cell expansion, two different concentrations of IL-2 were tested for maximum efficacy in NK cell expansion: 50 ng/ml and 500 ng/ml. To derive and expand NK cells, PBMCs were cultured in the NK MACS Basal medium with 50 ng/ml recombinant human IL-2 because the two concentrations did not exhibit a reasonable difference. NK cells were treated with retronectin the day before transduction, and transduction with Zhen Lab's D1D2-CAR-41BB CAR lentivirus occurred seven days after the initial expansion of the NK cells.

Cytokine Assay

NK cells were tested for their functional ability against ACH-2 HIV envelope-positive (Env+) cells. ACH2 cells contain a latent single integrated copy of the HIV-1 strain LAI, which is used as a model for chronic HIV-1 infection (14). The ACH-2 cells that were stimulated with phorbol 12-myristate 13-acetate (PMA) and ionomycin to reactivate latent HIV became HIV Env+ cells, whereas non-stimulated ACH-2 cells were HIV envelope negative (Env-) cells. ACH-2 cells were stimulated with PMA and ionomycin 24 hours prior to co-incubation in order to activate the HIV-1 expression and make these cells HIV Env+. To investigate functionality, 1.0×10^5 CAR-NK cells in 100 μL media were co-incubated with either 1.0×10^5 HIV Env+ or HIV Env- cells in 100 μL media overnight, followed by treatment of 0.2 μL GolgiPlug (Fisher Scientific) and 0.2 μL GolgiStop (Fisher Scientific) for six hours. Afterwards, cells were surface stained through immunofluorescence with the following antibodies: anti-human CD3 BV605 (Biolegend), anti-human CD56 BV711 (Biolegend), NKG2A BV510 (BD Biosciences), CD314 (NKG2D) BV785 (Biolegend), CD335 (NKp6) APC

(Biolegend), anti-human CD16 PerCP Cy5.5 (Biolegend), CD107a PE-Cy5 (Invitrogen), IFN- γ PE-Cy7 (Biolegend), GFP (Biolegend), and Zombie Yellow (Biolegend) and analyzed by flow cytometry. In subsequent trials, STING agonists BDW and cGAMP were used to stimulate CAR-NK cells during co-incubation to determine if STING agonists could improve CAR-NK killing ability. The flow cytometry data was analyzed through the FlowJo software. To determine the statistical significance of results, unpaired two-tailed t-tests assuming normality were performed on Microsoft Excel with an alpha level of 0.05.

RESULTS

Miltenyi Biotec NK MACS Medium Demonstrated Superior Efficacy in the Expansion of NK Cells

NK cells expanded from PBMCs cultured in the Miltenyi Biotec NK MACS medium exhibited a fold growth of 58.59 after 20 days (Figure 3). NK cells expanded from PBMCs cultured in the ImmunoCult NK Cell Medium exhibited an NK cell fold growth of 3.59 after 20 days. An unpaired t-test assuming normality and a threshold of 0.05 between the two conditions resulted in a t-value of 38.8909 and a p-value of less than 0.0001, indicating a significant difference in NK cell fold growth between the two media after 20 days of expansion. The CAR-NK cells cultured in NK MACS medium with 500 ng/ml IL-2 showed a one to two-fold increase in growth over CAR-NK cells cultured in NK MACS medium with 50 ng/ml IL-2 (Figure 4). An unpaired t-test assuming normality and a threshold of 0.05 between the two conditions resulted in a t-value of 0.4596 and p-value of 0.6620, indicating that there is no significant difference between the two concentrations. On day 24 of NK cell expansion, 64.8% of cells in the NK MACS Medium were CD56+, whereas 3.85% of cells in the ImmunoCult NK Cell Medium were CD56+. An unpaired t-test assuming normality and a threshold of 0.05 between the two conditions resulted in a t-value of 91.0966 and a p-value of less than 0.0001, indicating a significant difference in NK cell growth between the two media.

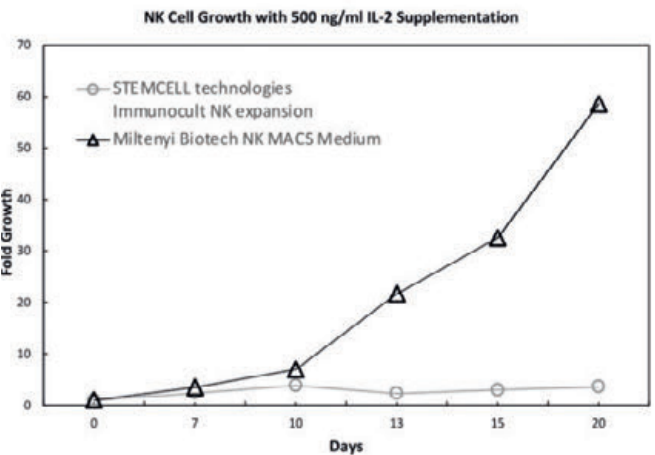


Figure 3: Media selection optimization for expansion of natural killer (NK) cells from healthy donor peripheral blood mononuclear cells (PBMCs).
The graph represents NK cell fold growth with 500 ng/mL IL-2 supplementation over a 20-day expansion period. Expansions for both mediums started with 5 x 10⁵ PBMCs, and fold growth was calculated based on this initial cell count.

Successful Transduction of NK Cells Produced CAR-NK Cells that Exhibited Functionality Upon Co-Incubation with HIV Envelope-Positive Cells

Among the cells transduced on day seven in 500 ng/ml IL-2 MACS Medium, 8.62% of NK cells expressed signs of successful CAR transduction. In the control group of PBMCs, there were no observable indications of CAR transduction among NK cells. An unpaired t-test assuming normality and a threshold of 0.05 between the PBMC control and the transduced NK cells resulted in a t-value of 11.2289 and a p-value of less than 0.0001, indicating a significant difference in the amount of transduced CAR-NK cells. The CAR-NK cells that were co-incubated with HIV Env+ cells exhibited expression of CD107a and IFN- γ . The CAR-NK cells in the HIV Env- cell condition showed minimal to no expression of CD107a and IFN- γ (Figure 5). An unpaired two-tailed t-test assuming normality and a threshold of 0.05 for the expression of both CD107a and IFN- γ between HIV Env- and HIV Env+ conditions resulted in a t-value of 5.6639 and a p-value of 0.0013, indicating a significant difference in the expression of CD107a and IFN- γ among CAR-NK cells with HIV Env+ compared to HIV Env- cells.

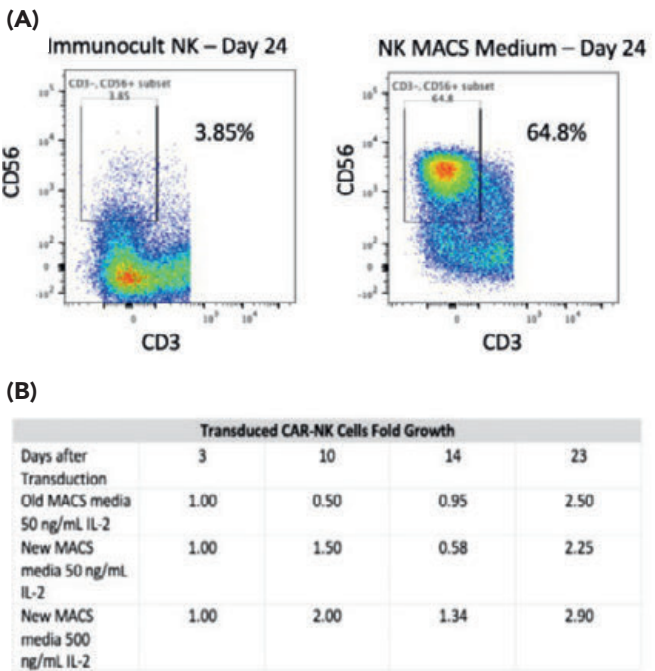


Figure 4: Media selection and interleukin 2 (IL-2) cytokine optimization for transduction of natural killer (NK) cells from healthy donor peripheral blood mononuclear cells (PBMCs).
(A) Immunocult NK and NK MACS mediums were used to expand NK cells from healthy donor PBMCs. 500,000 fresh PBMCs were initially cultured for each medium. After 24 days, a sample of 1.5 x 10⁵ NK cells was taken from each culture and analyzed through flow cytometry. Phenotypic markers for NK cells were gated to observe the percentage of NK cells within the PBMCs after 24 days of NK expansion. The gatings reflect NK cell phenotypic markers, as the gatings represent the CD56+ and CD3- populations within the culture. 64.8% of cells in the NK MACS Medium were CD56+, whereas 3.85% of cells in the ImmunoCult NK Cell Medium were CD56+. (B) The table shows the expansion of CAR-NK cells after ten days of transduction at different concentrations of IL-2. The values represent the fold growth of the cell cultures under the three conditions.

CAR-NK Stimulation with STING Agonist led to Greater Cell Death Upon Co-Incubation with HIV Envelope-Positive Cells

Among the live cells, of which 54.4% are CAR-NK cells, co-incubated with HIV Env⁻ cells, stimulation with the STING agonist cGAMP resulted in 32.3% cell death among all live cells. The mock condition, where no STING agonist was used, resulted in 26.6% cell death. However, an unpaired two-tailed t-test assuming normality and a threshold of 0.05 comparing the cell death between mock and cGAMP conditions resulted in a t-value of 0.0403 and p-value of 0.9692, indicating that the difference is not significant. Among the CAR-NK cells co-incubated with HIV Env⁺ cells, stimulation with the two STING agonists cGAMP and BDW resulted in 78.3% and 69.8% cell death, respectively. The mock condition resulted in 66.8% cell death (Table 1). However, an unpaired two-tailed t-test assuming normality and a threshold of 0.05 resulted in a p-value of 0.9378 for mock vs cGAMP and 0.9838 for mock vs BDW, indicating no significant differences. No improved cytokine production in the CAR-NK cells was observed for cells incubated with STING agonists.

Donor	Coincubation	Live cells	% NK cells
3	mock + Env ⁻ ACH2	73.4%	56.3%
3	BDW + Env ⁻ ACH2	79%	54.9%
3	cGAMP + Env ⁻ ACH2	67.7%	54.4%
3	mock + Env ⁺ ACH2	33.2%	57.7%
3	BDW + Env ⁺ ACH2	30.2%	53.4%
3	cGAMP + Env ⁺ ACH2	21.7%	45%

Table 1: Percentage of live natural killer (NK) cells from peripheral blood mononuclear cells (PBMCs) with stimulators of interferon genes protein (STING) agonist stimulations.

NK cells were expanded from a healthy donor's PBMCs for seven days. After seven days, NK cells were transduced with CAR lentivirus that contains D1D2-CAR-41BB. After 15 days since the first day of transduction, chimeric antigen receptor natural killer (CAR-NK) cells were co-incubated with HIV envelope positive (Env⁺) and HIV envelope negative (Env⁻) cells overnight. After co-incubation overnight under six different conditions, the cells were analyzed through flow cytometry. The table shows the percentage of all live cells from the PBMCs, as well as the percentage of NK cells from the percentage of live cells.

DISCUSSION

This study aims to evaluate and investigate the therapeutic potential of CAR-NK cells for treating HIV infection. The current treatment for HIV, antiretroviral therapy, presents major challenges in ensuring that patients take their anti-HIV medications daily and in controlling repercussions from interactions with other drugs. Though there is still widespread uncertainty on the viability of gene and cell therapy as a cure for HIV, this study addresses the possibilities of expanding NK cells, transducing NK cells, and using CAR-NK cells as an anti-HIV treatment.

The first part of the study determined media selection and optimized growth conditions for the expansion of NK cells. The Miltenyi Biotec NK MACS medium was more effective in the expansion of NK cells compared to the STEMCELL technologies ImmunoCult NK Cell Medium. There was a greater percentage of CD56⁺ cells with the NK MACS medium compared to the ImmunoCult NK Cell medium. The NK cells that were cultured in MACS medium were used to determine the optimal amount of recombinant human IL-2. Although 500 ng/mL of recombinant human IL-2 with the MACS medium showed a one to two-fold

increase in growth of NK cells by day ten of expansion, there was minimal difference between the concentrations of 50 ng/mL and 500 ng/mL IL-2. In subsequent cultures, the NK cells were cultured in the NK MACS medium with 50 ng/mL of IL-2 supplementation.

Having established the efficacy of NK cell expansion media, the study further aimed to determine if transducing NK cells with CAR lentivirus was possible. Green fluorescent protein (GFP) was utilized as the expression label for CAR. GFP-positive cells were observed after transduction, which indicates that CAR was successfully expressed in those cells. In comparison to the control condition, the transduction condition showed a statistically significant increase in the expression of CAR. Additionally, the experiments investigated the functionality of NK cells through the expression of CD107a and the release of IFN- γ . The expression of CD107a in CAR-NK cells and the release of IFN- γ in the HIV Env⁺ condition indicates that the transduced CAR-NK cells do release cytokines and are thus functional when co-incubated with HIV env⁺ cells. The successful transduction shown in the study is an important first step in evaluating the feasibility of developing CAR-NK cell therapy, in the context of HIV infection as well as other disease processes. It sets a strong foundation for continuing research in gene and cell therapy for the treatment of HIV.

Finally, the effects of the STING agonists cGAMP and BDW were investigated on CAR-NK cells. There was an 11.5% increase in cell death among CAR-NK cells when co-incubated with HIV Env⁺ cells in the STING agonist conditions in comparison to the mock condition. The study observed that STING agonists exhibit cytotoxic effects, which induced greater cell death in CAR-NK cells. This indicates that further optimization of CAR-NK functionality with STING agonists is needed, including exploring different STING agonists and altering concentrations of STING agonists. Data did not support a significant difference in the expression of CD107a or release of IFN- γ between the STING agonist and mock conditions.

Overall, specific culture conditions that promote the rapid expansion of NK cells were identified by adjusting media conditions and cytokine treatments. After optimizing growth conditions for NK cells, the experiments successfully modified NK cells with CAR lentivirus and showed that these CAR-NK cells were functional in killing HIV envelope-expressing target cells. These results are consistent with the findings of Lim *et al.*, who developed CAR-NK cells and showed that they recognized and killed mimic HIV-infected cell lines (15). These results further expand on the reports of Albinger *et al.*, who reported successful CAR-NK functionality in treating malignant tumorigenic cells, to the functionality of CAR-NK cells in the context of HIV (12). The alignment of the data with the results of other studies supports the functionality of CAR-NK therapy *in vitro*.

However, some limitations within the study should be considered. First, while the data indicates that transduction of NK cells is possible, transduction needs to be further optimized to achieve a higher yield of CAR-NK cells. The current transduction in this study yielded a low percentage of CAR-NK cells, suggesting that investigation into the transduction process is needed. Next, while this study showed that CAR-NK cells were able to secrete proinflammatory cytokines in the presence of HIV Env⁺ cells, no improvement in cytokine production was observed when CAR-NK cells were stimulated *in vitro* with STING agonists.

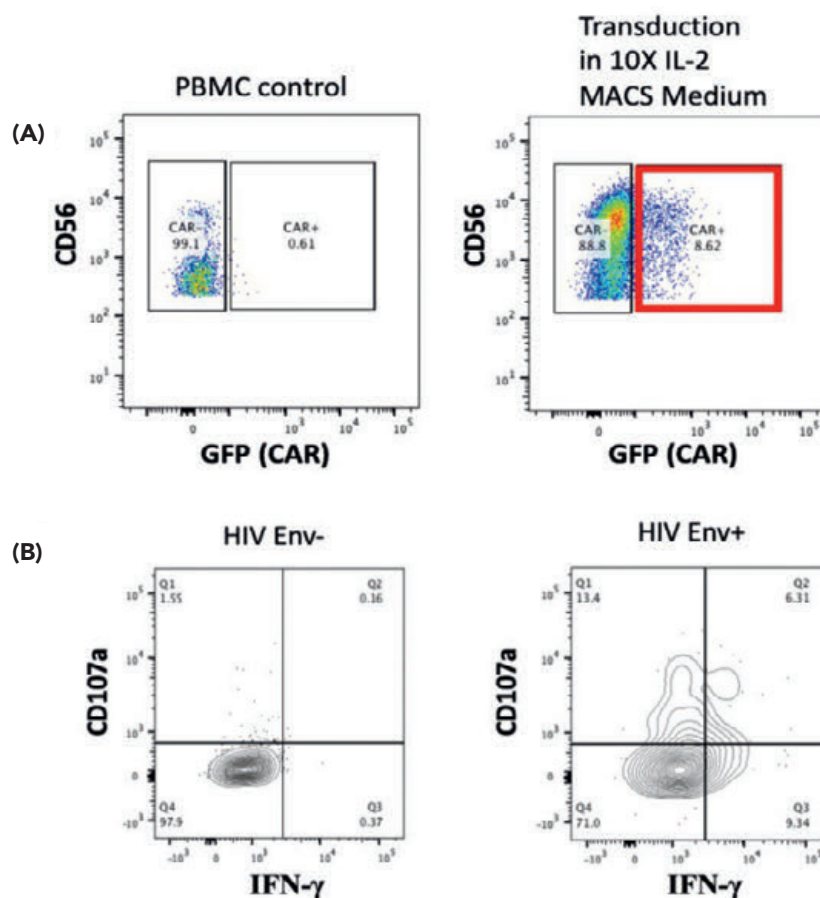


Figure 5: Percentage of successful chimeric antigen receptor natural killer (CAR-NK) transduction after expansion of natural killer (NK) cells from peripheral blood mononuclear cells (PBMCs) and assessment of CAR-NK functionality through cytokine assay.

(A) Green fluorescent protein (GFP) was used to label transduced NK cells that express the CAR. The graph to the left shows the percentage of GFP negative and GFP positive cells among the PBMC control while the graph on the right shows the aforementioned percentages among transduced NK cells. **(B)** The graphs show percentages of CAR-NK cells that express CD107a, express IFN- γ , express both CD107a and IFN- γ , or neither. The left and right graphs show CAR-NK cells co-incubated with HIV envelope negative (Env-) cells and HIV envelope positive (Env+) cells.

This contrasts with Da *et al.*, who found that the STING agonist cGAMP directly activated NK cells and enhanced the sensitivity of NK cell cytotoxicity on pancreatic cancer cells, suggesting further investigation of the use of STING agonists with NK cells in the context of HIV may be needed (10). There are various possible reasons why the data does not align with Da *et al.* First, this study used CAR-NK in the context of HIV-infected cells, whereas Da *et al.* used them in the context of pancreatic cancer cells. Also, this study used the D1D2-CAR-41BB CAR lentivirus whereas Da *et al.* used a second-generation Mesothelin-targeting CAR. Finally, variation between the PBMCs obtained from different donors is another limitation of the study because there could have been different amounts of cells that may interfere with the transduction process. Follow-up investigations into the aforementioned areas are needed to properly power the study.

Gene and cell therapies have emerged as promising advancements in medical treatments. This study starts from the cellular level and shows the possibility of CAR-NK cell therapy as a cure for HIV. The continuous optimization of the transduction of NK cells contributes to the progression of CAR-NK studies from bench to bedside. With minimal literature on the *in vitro* expansion of NK cells, the data aids in determining the optimal

growth conditions to expand NK cells. Moreover, the study shows CAR-NK functionality at a preliminary level, which serves as proof of concept for the *in vivo* efficacy of CAR-NK cell therapy for HIV. Based on the results of this experiment's data, the next feasible steps include improving transduction and incorporating STING agonists to enhance CAR-NK function. This research will serve as a strong foundation for future *in vivo* experiments of CAR-NK cell therapy with mice models, with hopes to bridge the gap between preclinical investigation and clinical trials. This study's findings underscore the potential of CAR-NK cell therapy as a novel approach to HIV treatment, which could complement or even replace the need for lifelong antiretroviral therapy.

CONFLICT OF INTEREST

Author declares that they have no conflicts of interest.

EDITORS

This article was reviewed by Cecilia McCormick, Caden Chow, Eliana Bohn, Joanna Rhim, Zoe Yeh; edited by Andrew Wang, Siddhika Naik; and laid out by Danny Zhu and Dashrit Pandher.

REFERENCES

1. V. Simon, D.D. Ho, Q.A. Karim, HIV/AIDS epidemiology, pathogenesis, prevention, and treatment. *Lancet*. **368**, 489-504 (2006). doi:10.1016/S0140-6736(06)69157-5.
2. E. Kumah, D.S. Boakye, R. Boateng, E. Agyei, Advancing the global fight against HIV/AIDS: Strategies, barriers, and the road to eradication. *Ann. Glob. Health*. **89**, 83 (2023). doi:10.5334/aogh.4277.
3. C.H. June, M. Sadelain, Chimeric Antigen Receptor Therapy. *N. Engl. J. Med.* **379**, 64-73 (2018). doi:10.1056/NEJMr1706169.
4. A. Zhen *et al.*, Robust car-T memory formation and function via hematopoietic stem cell delivery. *PLOS Pathog.* **17**, 1-20 (2021). doi:10.1371/journal.ppat.1009404.
5. G. Xie *et al.*, Car-NK Cells: A promising cellular immunotherapy for cancer. *EBioMedicine*. **59**, 102975, 1-10 (2020). doi:10.1016/j.ebiom.2020.102975.
6. G. Alter, J.M. Malenfant, M. Altfeld, CD107A as a functional marker for the identification of Natural Killer Cell activity. *J. Immunol.* **294**, 15-22 (2004). doi:10.1016/j.jim.2004.08.008.
7. S. Ziegler *et al.*, CD56 is a pathogen recognition receptor on human natural killer cells. *Sci. Rep.* **7**, 1-13 (2017). doi:10.1038/s41598-017-06238-4.9.
8. K.S. Wang, D.A. Frank, J. Ritz, Interleukin-2 enhances the response of natural killer cells to interleukin-12 through up-regulation of the interleukin-12 receptor and STAT4. *Blood*. **95**, 3183-3190 (2000). doi:10.1182/blood.V95.10.3183.
9. R. Elahi, A.H. Heidary, K. Hadiloo, A. Esmailzadeh, Chimeric antigen receptor-engineered natural killer (CAR NK) cells in cancer treatment; recent advances and future prospects. *Stem Cell Rev.* **17**, 2081-2106 (2021). doi:10.1007/s12015-021-10246-3.
10. Y. Da *et al.*, Sting agonist CGAMP enhances anti-tumor activity of car-NK cells against pancreatic cancer. *OncolImmunology*. **11**, 1-12 (2022). doi:10.1080/2162402x.2022.2054105.
11. J. Zhao *et al.*, Cellular Target Deconvolution of Small Molecules Using a Selection-Based Genetic Screening Platform. *ACS Cent. Sci.* **8**, 1424-1434 (2022). doi:10.1021/acscentsci.2c00609.
12. N. Albinger, J. Hartmann, E. Ullrich, Current status and perspective of CAR-T and CAR-NK cell therapy trials in Germany. *Gene Ther.* **28**, 513-527 (2021). doi:10.1038/s41434-021-00246-w.
13. E.L. Heipertz *et al.*, Current perspectives on “off-the-shelf” allogeneic NK and car-NK cell therapies. *Front. Immunol.* **12**, 1-21 (2021). doi:10.3389/fimmu.2021.732135.
14. J.H. Kim *et al.*, Consequences of human immunodeficiency virus type 1 superinfection of chronically infected cells. *AIDS Res. Hum. Retroviruses*. **9**, 875-882 (1993). doi:10.1089/aid.1993.9.875.
15. R.M. Lim, L. Rong, A. Zhen, J. Xie, A Universal CAR-NK Cell Targeting Various Epitopes of HIV-1 gp160. *ACS Chem. Biol.* **15**, 2299-2310 (2020). doi:10.1021/acscmbio.0c00537.

Identification of Gender-Based Cyberbullying Tweets with Machine Learning

Shriya Char¹, Henry Austin²

¹Department of Computer Science, University of California, Los Angeles. ²Department of Computer Science, Harvard University.

ABSTRACT

In recent years, cyberbullying has emerged as a prevalent issue and has even overtaken traditional bullying, which typically involves direct physical and verbal abuse. Cyberbullying occurs on a multitude of social media sites, including Twitter. Twitter serves as an ideal research focus due to its public platform and the diversity of its users. Previous studies have examined different features of Twitter, such as user information and past Twitter activity, in combination with a tweet's content to identify cyberbullying; however, no studies have focused solely on gender-based cyberbullying. To enhance online safety and tackle gender-based bullying, this study aims to accurately classify gender-based cyberbullying instances and to survey machine learning algorithms in their ability to accurately classify tweets as instances of gender-based bullying. To this end, diverse machine learning techniques were tasked with classifying tweets by their gender-based bullying content. The data was bootstrapped, and different evaluation metrics for each model included accuracy, F1-score, precision, recall, and Area Under Curve (AUC). The Random Forest classification method with bootstrapping emerged as the most effective, achieving a 96.80% accuracy, F1-score of 0.9678, and AUC of 0.97. Among the neural network architectures, MLP with bootstrapping performed the best with a 95.70% accuracy, F1-score of 0.9569, and AUC of 0.96. Thus, these findings underscore the potential for enhanced safety protocols and improved content moderation on platforms like Twitter. Future research could benefit from exploring specific sentiment analysis coupled with users' prior activity to better understand the underlying causes of cyberbullying and provide targeted intervention.

INTRODUCTION

In recent years, cyberbullying, a form of bullying that occurs online, has emerged as a prevalent issue alongside the increased usage of the Internet and social media, especially among young people. Common forms of cyberbullying include sending threatening messages, spreading rumors online, posting hurtful comments on social media, and sharing a user's private information without their consent. A survey by Pew Research Center found that at least 59% of teens have experienced some type of cyberbullying (1). Additionally, the recent pandemic and subsequent greater dependence on the internet have led to a rise in cyberbullying, as shown in Karmakar and Das's study of tweets at the start of the COVID-19 pandemic (2). This study aims to distinguish tweets (posts on Twitter) as either non-bullying or gender-related cyberbullying, given the existing lack of investigation of this topic within the field. The Twitter platform was chosen because of its open nature, which enables rapid and widespread message sharing among a diverse audience.

In contrast to conventional bullying, cyberbullying's use of digital communication enables perpetrators to exercise greater discretion in their actions, amplifying the potential harm inflicted on victims. Moreover, online interactions can be anonymous, which can embolden individuals to engage in hurtful behaviors. A study examining the effects of online anonymity on offline behavior found that, while utilizing anonymous accounts, participants interacting with sexist tweets tended to express more sexist attitudes than those

using identifiable ones (3). Furthermore, women tend to experience more gender-based harassment than men: in the U.S., 4.3%–24.1% of men and 31.7%–33.9% of women experience gender-based harassment online (4). Creating safe online spaces could facilitate the mitigation of existing inequalities in the real world, including employment and economic mobility.

Content moderation is a crucial challenge for both social media and public forums, and it is an area of recent interest for machine learning (ML) and artificial intelligence (AI) research. Given the detrimental impact of cyberbullying, this project attempts to mitigate harm by accurately classifying tweets as one of two labels: gender-based bullying or not bullying. This was conducted via supervised learning, where various ML classification algorithms and Neural Network Architectures were executed on a dataset of 46,017 tweets to predict labels for the testing data. The algorithms included Naive Bayes, Support Vector Machines, Random Forest, Logistic Regression, K-Nearest Neighbors, Multi-Level Perceptron, Feedforward Neural Network, and Long Short-Term Memory. Different accuracy measures were then assessed and compared to those of a previous study for each algorithm. It was hypothesized that deep learning approaches, such as neural networks, would demonstrate higher precision, recall, and overall accuracy in classifying cyberbullying tweets when compared to traditional algorithms like Support Vector Machines and Naive Bayes, given that deep learning has been thought to outperform traditional classification methods at capturing patterns within text (5). The

results of this study could be useful in the automation of content moderation for technology companies.

Deep learning has become more popular in recent years. In simple terms, it is a program that learns to recognize patterns to classify data. It is given known data and typically the more data it has, the more accurate its predictions are. In 2012, Krizhevsky created AlexNet and won the ImageNet challenge by using deep learning for image recognition. This was a milestone for deep learning as AlexNet greatly outperformed other traditional classification models. The popularity of deep learning models has continued to grow, and deep learning has also been thought to outperform traditional classification methods at capturing patterns within text (5). Therefore, it is hypothesized that deep learning approaches, such as neural networks, will demonstrate higher precision, recall, and overall accuracy in classifying cyberbullying tweets when compared to traditional algorithms like Support Vector Machines and Naive Bayes.

Technical Background

Unlike our approach, the previous study by Al-garadi *et al.* (2016) utilized four specific features—network, activity, user, and content—to detect cyberbullying behavior (6). The study gathered 2.5 million geotagged tweets from within California, exclusively using publicly available content in adherence to Twitter's privacy policies. While these details might have improved classification accuracy, limiting the study to California restricts its geographic and linguistic scope.

The study utilized several machine learning algorithms, including Naive Bayes for probabilistic classification and Support Vector Machines (SVM) for decision boundary-based classification, among others.

While not needed for this study, Al-garadi *et al.* (2016) employed the Synthetic Minority Over-sampling Technique (SMOTE) to counteract class imbalance and maintain result quality. They found that random forest using SMOTE showed the best Area Under the ROC Curve (AUC of 0.943) and f-measure (0.936). The AUC ranges from 0 to 1 and measures the overall ability of the model to distinguish between the labels. The f-measure evaluates the model performance using precision and recall, which take into account false positives and negatives.

In another study, 16,000 tweets were labeled as racist, sexist, or neither, with the dataset being bootstrapped (7). They used ML classification algorithms like logistic regression, support vector machine, random forest, and naive Bayes classifier. However, they discovered that deep learning algorithms significantly outperformed these traditional methods. The study implemented a combination of neural networks for cyberbullying detection, including Convolutional Neural Networks (CNN), Long Short-Term Memory (LSTM), and Bidirectional LSTM (BLSTM). The detailed architecture of these models is illustrated in Figure 1. To address class imbalance in the dataset, the researchers applied oversampling to the bully data threefold, enabling them to achieve an F1-score of 0.94 on the Twitter dataset.

Although these past studies have provided valuable insights into general cyberbullying detection, they often overlook the specific nuances associated with gender-based cyberbullying. This study addresses this discrepancy by training models according to the unique features and patterns prevalent in gender-based cyberbullying tweets. Unlike broader cyberbullying datasets, which may encompass a wide range of harassment behaviors, gender-based cyberbullying datasets focus explicitly on instances of

harassment and discrimination targeting individuals based on their gender identity or expression. Figure 4 provides further insight into terms specific to gender-based cyberbullying.

By contextualizing cyberbullying research within the framework of gender-related issues, this paper not only contributes to the advancement of cyberbullying detection techniques but also highlights the importance of addressing gender-based discrimination and inequality in online spaces. There is an urgent need for a comprehensive reevaluation of platform policies to genuinely address the harms experienced by marginalized communities and promote both free expression and user safety.

METHODS

The following was conducted on Google Colab using Python version 3.10.

Dataset

This project focuses on language data, utilizing a dataset comprised of 46,017 Twitter tweets categorized into six classes: gender, age, race, religion, other, and not bullying; these categories were determined by identifying specific qualities of the victims that cyberbullies target. Each class contains roughly 8,000 tweets, ensuring a balanced and diverse dataset. Previous cyberbullying datasets maintained significant tweet class imbalances, adversely affecting model accuracy due to the limited representation of certain classes (8).

Dynamic query expansion (DQE) is a technique that enriches the initial search query with synonyms and related phrases, thereby enlarging the dataset. When applied to previously collected tweet datasets, DQE significantly increased the sample size across the classifications. Historically, this technique has been effective in detecting events like terrorist attacks and flu outbreaks (9, 10), making it equally valuable for identifying diverse cyberbullying instances, as shown in Figure 2.

The application of DQE facilitated the creation of a dataset superior in balance and size to those previously available. This improvement ensures that the models discussed in this paper are more reliable and accurate in bullying type prediction. As Wang *et al.* (2020) highlights, earlier attempts at fine-grained classification of cyberbullying were limited by a severe class imbalance; using DQE aids in developing a precise model for predicting gender-based bullying.

Prior to applying ML models, data preprocessing was conducted to refine the dataset. Due to the focus on gender-bullying, the data was narrowed down to extract only gender bullying and non-bullying tweets, which resulted in a subset of 15,918 tweets, 7,973 of those being gender bullying tweets and 7,945 being non-bullying tweets.

In order to ensure linguistic consistency and account for the unique characteristics of bullying behaviors in different languages, the tweets were sorted based on the English language using the langdetect library in Python. The library, which uses probability to identify language by comparing letter groups against known patterns, reduced the dataset from 46,017 to 11,436 tweets, thereby standardizing the language and increasing relevance to the research goals. As a result of the language filtration reducing the dataset size, bootstrapping was applied to generate a dataset of 20,000 tweets, improving the training process.

The data was then split into training and testing by using Python's `train_test_split` function, with 20% of the dataset becoming allocated

as testing data and 80% as training data. To extract significant features for classification, textual content underwent processing, including tokenization, lemmatization, and the removal of stop words and punctuation to refine the dataset. Tokenization is the initial step, in which a sentence is broken down into its constituent words. Lemmatization follows, transforming words into their base or root form; for example, “running” becomes “run.” Stop words, which include common words such as articles, prepositions, and conjunctions, were also removed as they carry limited meaningful information.

The function `process_lang_data` contained the preprocessing steps mentioned above, and `CountVectorizer` from `scikit-learn` was initialized on it. `CountVectorizer` operates by building a vocabulary of all the unique words encountered in the text data, with each word assigned a unique number. Afterward, for each tweet, `CountVectorizer` counts the frequency of occurrence for each word in the vocabulary, creating a feature vector, a numerical representation of this information.

This feature extraction process resulted in the creation of a feature matrix, denoted as `X_train`, containing 1,000 features derived from

the tweet content; these features are the 1,000 most common words that appear in the training dataset of gender-based cyberbullying tweets. These features play a crucial role in distinguishing between gender-based cyberbullying and non-bullying tweets.

As previously mentioned, the dataset was split into training and testing data. Then the tweets’ text was processed to extract features. Various ML Classification Algorithms and Neural Network Architectures mentioned below were then applied.

Deep Learning vs Non Deep Learning Algorithms

Deep learning methods, like neural networks, consist of interconnected layers of neurons that automatically learn complex patterns from data through iterative optimization processes. In contrast, non-deep learning methods, such as Support Vector Machine (SVM) and Random Forest, make decisions based on predefined rules or boundaries learned from the features of the input data without the need for extensive training on large datasets. Some of these models also have weights: these weights determine the importance or contribution of each feature (such as the presence of certain words) to the model’s predictions.

Name	Total	CB	Not CB	Age	Ethnicity	Gender	Religion	Other
Agrawal [30]	16050	5963	10087	0	13	2841	1922	187
Brettschneider [33]	4475	183	4292	49	29	34	0	71
Chatzakou [29]	1500	1278	222	17	100	115	10	1036
Davidson [31]	205	181	24	5	27	121	1	27
Waseem [34], [35]	12899	8900	3999	0	86	3339	0	5475
WISC [32]	4095	1078	3024	94	17	39	0	921
Collective Before DQE	39224	17583	21648	165	272	6489	1933	7717
Collective After DQE	69767	50468	19299	10010	12730	10277	9367	8084

Figure 1: Impact of DQE on Cyberbullying Class Balance.
This table comes from the J. Wang, K. Fu, and C. Tien-Lu study (8). The leftmost column represents various sources of tweet data and the topmost row represents the different types of bullying. Each number represents the number of tweets that are from a certain source and fall under a certain category: for instance, 13 tweets in the Agrawal dataset are ethnicity-based cyberbullying. This table highlights how DQE was utilized to create a more balanced distribution across the different classes. The term “Collective” refers to the collection of all the tweets from various sources; before DQE there were significant differences in the numbers of tweets belonging to each type of bullying, while afterward, there is more of a balance.

	tweet_text	cyberbullying_type
0	In other words #katandandre, your food was cra...	not_cyberbullying
1	Why is #aussietv so white? #MKR #theblock #ImA...	not_cyberbullying
2	@XochitlSuckkks a classy whore? Or more red ve...	not_cyberbullying
3	@Jason_Gio meh. :P thanks for the heads up, b...	not_cyberbullying
4	@RudhoeEnglish This is an ISIS account pretend...	not_cyberbullying
...
15913	Any females that really know me know I'm even ...	gender
15914	RT @_chrisdowns_: #QuestionsForMen This one's ...	gender
15915	Sucks to have the smile wiped off your own fac...	gender
15916	No. He said women choose to be gay, men don't...	gender
15917	RT @uberfeminist: #TwitterFeminism can't convi...	gender

15918 rows x 2 columns

Figure 2: Filtered dataset of gender-based bullying tweets.
This image is from the Python notebook in which all the analyses in the study were performed. Since this study’s focus is gender-based cyberbullying, other types of cyberbullying classifications have been filtered out. Each row pertains to a different tweet from the filtered dataset and the columns display the tweet content and the category of tweet (cyberbullying or gender-based bullying).

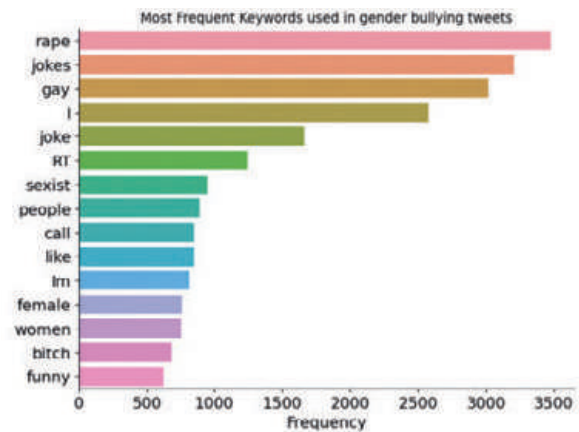


Figure 3: Most Frequent Keywords used in gender-based bullying tweets.
This chart provides insight into the intricacies of the classification algorithms because of their use of language processing. The chart features rows of words prevalent in gender-based cyberbullying tweets, with bars indicating each word’s frequency across the dataset. For instance, the word “jokes” appears about 3200 times across gender-based bullying tweets.

Logistic Regression

Logistic regression is used for modeling the relationship between one or more independent variables, represented by word frequencies, and a dependent variable. These word frequencies serve as the features, with distinct weights assigned to them. The dependent variable, with two possible outcomes, (gender-based bullying or not), is predicted using the logistic (sigmoid) function, which estimates the likelihood of a tweet being labeled as gender-based cyberbullying. The logistic function is applied on a linear combination of input features, their associated weights, and a bias term, and maps this real number to a probability between 0 and 1. The LogisticRegression model was imported from sklearn.linear_model.

$$z = W\chi + b \quad (1)$$

$$\sigma(z) = 1/(1+e^{-z}) \quad (2)$$

Naive Bayes

Naive Bayes is an algorithm that calculates the probabilities of different outcomes, such as whether a tweet is cyberbullying or not, based on the presence of specific features, including certain words, within the data. For instance, if a tweet contained the word “mean,” the algorithm would compute the probability of a tweet containing “mean,” assuming that it is a gender-based cyberbullying tweet. This algorithm operates under the assumption that the features are independent. When analyzing the features of test tweets, it computes the probability associated with each label to determine the most likely classification for the tweet. Ultimately, the label with the highest probability is assigned to classify the tweet. The MultinomialNB implementation was imported from the sklearn.naive_bayes Python module.

$$P(S|Features) = P(Features|S) \cdot P(S) / P(Features) \quad (3)$$

Support Vector Machines

Another classifier used was Support Vector Machines (SVM), which operates by identifying a hyperplane, which is a flat, multidimensional surface that divides a space into two parts. SVM searches for one that maximizes the margin between two

classes, with the most critical data points, known as ‘support,’ lying closest to this boundary. The model examines them closely, since it is crucial that they are classified accurately; these points are most important in determining the final orientation of the decision boundary. Once the hyperplane equation is defined, if substituting the new data point’s value yields a positive result, it signifies that the point belongs to one class; conversely, a negative result indicates it belongs to the other class. Importantly, the points on one side of the line belong to one class while the points on the other side of the line belong to the other class. The SVM implementation was imported from sklearn. All data sources, including training datasets, were acquired from Kaggle (11), ensuring transparency and reproducibility of the research.

Random Forest

Random Forest involves a series of decision trees, each randomly assigned a subset of the training data (tweets) and specific features, such as frequency of certain words in gender-based bullying tweets. This approach ensures variability among decision trees, reducing the model’s tendency to overfit to the training data, where the model learns to memorize the training data rather than generalize well to new, unseen data. After each individual tree makes its decision, they collectively vote, and the label that receives the majority votes determines the classification of each testing tweet. The RandomForestClassifier was imported from sklearn.ensemble, a component of the scikit-learn library.

K-Nearest Neighbors

K-Nearest Neighbors (KNN) locates a specified number of neighboring points, K, closest to a new point in terms of feature similarity. Here, KNeighborsClassifier was imported from the sklearn.neighbors library. The process can be thought of as identifying tweets that share many similar words. After neighboring points are identified, the test tweet is classified based on the most common label among these neighbors. This method effectively categorizes the new tweet based on the predominant characteristics of its closest counterparts.

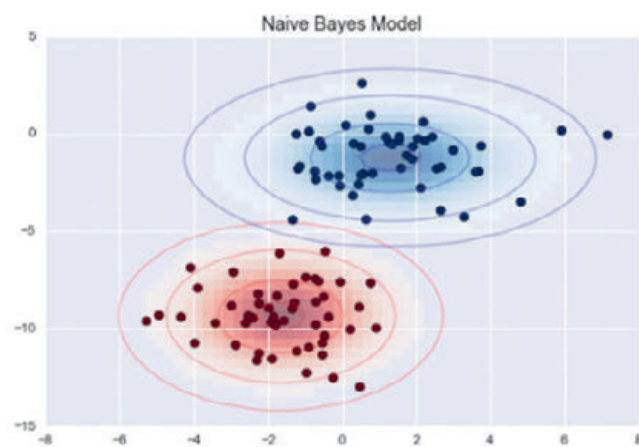


Figure 4: Naive Bayes Visual.

The red and blue regions represent two different labels and the black points are different data points corresponding to either one of the labels. The probability associated with each label would be used to compute the most likely label classification for a hypothetical new data point.

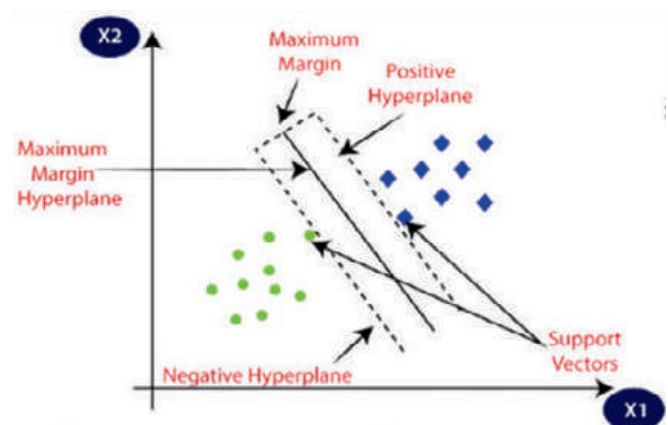


Figure 5: SVM Visual.

The green and blue dots represent two different labels, while the solid black line in the center represents the decision boundary or hyperplane. Additionally, the green and blue points closest to the boundary are the support vectors. As depicted, the maximum possible separation is achieved between the labels, and if substituting the value of a new data point into the hyperplane equation yields a positive value, it belongs to the blue class; otherwise, it belongs to the green class.

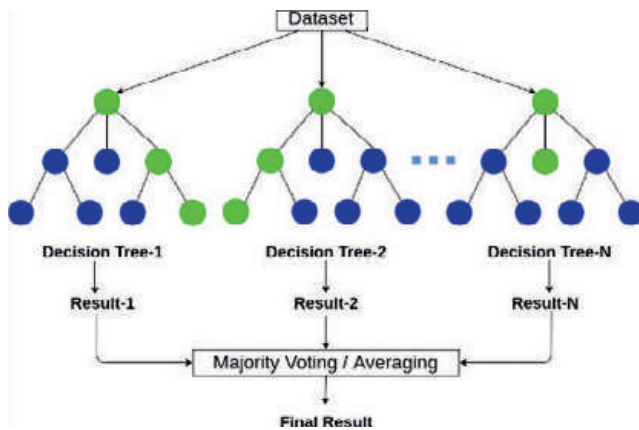


Figure 6: Random Forest Visual.

This example of the Random Forest algorithm involves three different decision trees. As depicted above, each tree receives a subset of the input dataset, before producing its individual classification result. Then finally, all the trees “vote,” meaning whichever label is the result of more trees is the final result.

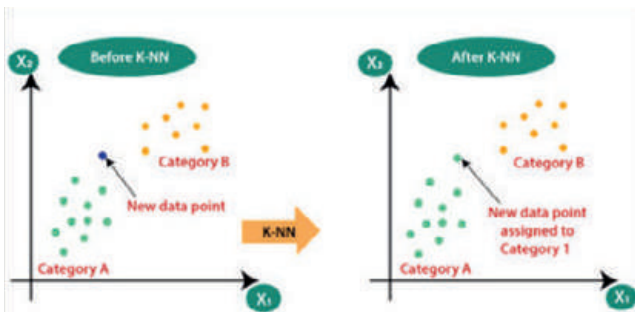


Figure 7: KNN Visual.

K in this context is the pre-selected number of nearest neighbors the model uses. Based on the K, the new data point is assigned the same label the majority of its nearest K neighbors have. In the above graphs, since Category A contains more of the new data point's neighbors, it is classified as Category A.

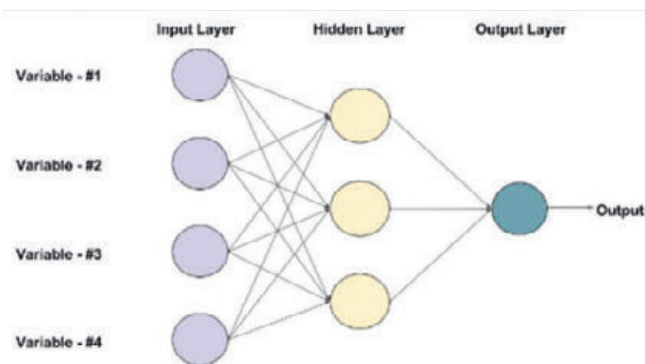


Figure 8: A Visual Example of FeedForward Neural Network

In this example, the input layer receives the raw data, with each neuron corresponding to a variable. The only hidden layer is composed of 3 neurons, and the 4 neurons from the input layer are weighted differently to derive the value of each neuron in the hidden layer. Finally, the hidden layer's neurons are used to compute the value of the output layer neuron.

Feedforward Neural Network

A feedforward neural network is structured with layers of neurons through which an input sequentially passes through; each neuron is assigned a weight, and its connections with the neurons in the next layer are also weighted. In general, the input layer processes information about the tweets such as word frequencies. The hidden layers are where the model aims to identify patterns in the tweet data, while the activation functions introduce another level of complexity, allowing the model to recognize more nuanced patterns in the data.

The feedforward neural network model used in this paper consists of several essential layers. Initially, an embedding layer converts integer-encoded words into dense vectors of fixed size, thereby reformatting the tweet content into a format that the network can process. Secondly, a global average pooling layer reduces dimensionality by focusing on the most significant information extracted from the words. After this lies two dense layers with 64 units (neurons) that each look at different aspects of the tweet information; 64 units was chosen to achieve a balance between computational efficiency and the model's capacity to learn complex patterns in the data. Each neuron adjusts its weights during the learning phase, reflecting the relative importance of various input aspects for predicting cyberbullying, indicating that certain words carry more weight than others in this context.

The neurons collaborate to interpret tweet patterns and meanings, with some focusing on identifying specific words or phrases indicative of cyberbullying, while others may target different elements. The Rectified Linear Unit (ReLU) activation function is a mathematical operation used within the neural network to capture more nuanced patterns in the data: neurons may activate or inactivate, depending on their input, which facilitates or impedes information flow, respectively. For example, a neuron specialized in detecting a particular word becomes inactive if that word is absent, to conserve computational resources. Finally, there is an output layer with a single neuron and sigmoid activation, which consolidates the inputs from the neurons from the last layer to make a prediction.

Multi-Layer Perception

The Multi-Layer Perceptron (MLP) is a type of feedforward neural network that is structured with interconnected layers of neurons, including the input layer, one or more hidden layers, and the output layer. The input layer accepts raw data as its input. Within each hidden layer, each neuron conducts weighted computations based on input received from the preceding layer of neurons. Finally, the output layer produces the model's predictions or results based on the computations in the hidden layers. This analysis makes use of two hidden layers, one with 500 neurons and another with 4 neurons, to capture complex input patterns, while balancing computational efficiency and preventing overfitting. The maximum number of iterations is set to 200, meaning the training process will continue until either the model performs consistently or the training data has run through the model 200 times. Here, MLPClassifier was imported from the `sklearn.neural_network` library.

Long Short-Term Memory

In addition to the standard elements found in traditional neural networks, Long Short-Term Memory (LSTM) networks incorporate

specialized memory cells capable of storing, modifying, or discarding information. These LSTMs are characterized by three crucial gates: the forget gate, which filters pertinent information and discards the rest, the input gate, which updates the memory cell with new

information, and the output gate, which leverages past memory and current information to determine the next hidden state and output. Given its ability to understand sequential text, this model was expected to be effective for processing a series of tweets.

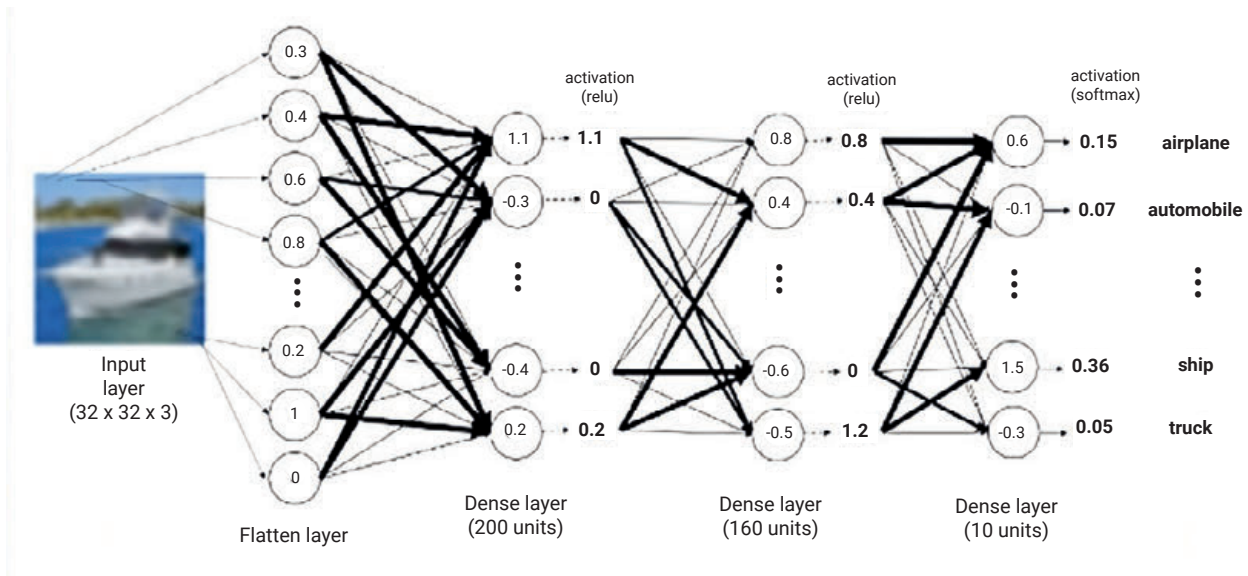


Figure 9: Example of MLP Visual.

The illustration depicts MLP used for image classification, where the initial input layer represents an image, which is then transformed into a one-dimensional array by the flatten layer to prepare for processing. The network's dense layers, consisting of 200 and 150 units respectively, employ ReLU activation to detect and learn from intricate patterns within the flattened image data. The final dense layer, with 10 units, uses a softmax activation function to categorize the image into one of several transportation classes, such as airplane or automobile, based on the learned patterns.

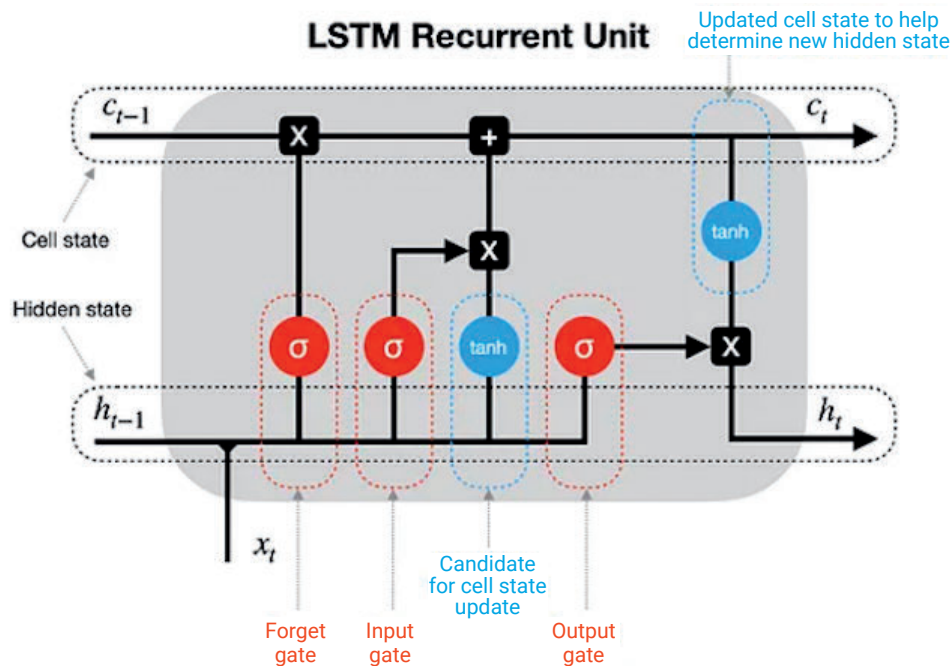


Figure 10: LSTM Neural Network Visual.

This visual depicts the different gates and their connections to each other and the cell and hidden states. The forget gate determines what information to discard using the sigmoid function (where 0 means fully forget and 1 means full remember). Similarly, the input gate uses the sigmoid function to decide what new information to store in the cell state, and the output gate determines what to output based on the current input and internal state. The candidate for cell state also applies some transformations to the input/previous hidden state.

Classification	Brief Summary	Hyperparameters
Logistic Regression	A logistic function is applied to a linear combination of input features (word frequencies), producing a probability between 0 and 1 used for classification.	Penalty: 'l2', C: 1.0, Solver: 'lbfgs', max_iter: 100
SVM	Identifies a decision boundary (hyperplane) that graphically maximizes separation between classifications for training data.	Kernel: RBF, Regularization parameter (C): 1.0
Naive Bayes	Calculates conditional probabilities for labels and features, assigning the most likely classification for a tweet.	N/A
Random Forest	Utilizes a series of decision trees each with a subset of data; the label with the most votes from the trees is assigned to the tweet.	Kernel: RBF, Bootstrapped trees: 250, Non-bootstrapped trees: 500
KNN	Finds the K closest neighboring points in feature space, classifying new points based on the majority label of these neighbors.	Bootstrapped: k=1, Non-bootstrapped: k=3

Table 1: Hyperparameters for Each Classification Method.

Logistic Regression, Random Forest, SVM, KNN have hyperparameters. Hyperparameters are model setup options, or values that are used to control a model's learning process prior to code execution. They control the model's complexity, speed, and generalization abilities.

Most models employed default hyperparameters as provided by sklearn to standardize across different models. Conversely, it was necessary to adjust specific hyperparameters, such as the value of K in KNN and the number of trees in Random Forest, to optimize performance.

NN Architecture	Brief Summary	Hyperparameters
Feedforward Neural Network	Processes input through layers, with an embedding layer for word conversion, dense layers for pattern analysis, and output layer for classification.	Vocabulary: 10000, Embedding: 16, Dense layers: 64 and 1 units, Learning rate: 0.001
MLP	A type of feedforward neural network with two hidden layers designed to process and predict through iterative training.	First hidden layer: 500, Second hidden layer: 4, Max iterations: 200
LSTM	A network with memory cells for sequential data, featuring gates to manage information flow for enhanced processing capability.	Vocabulary: 10000, Embedding: 16, LSTM layer: 64 units, Output layer: 1 unit, Learning rate: 0.001

Table 2: Hyperparameters for Each Neural Network Architecture.

Feedforward Neural Network, MLP, and LSTM all have hyperparameters. Hyperparameters are model setup options, or values that are used to control a model's learning process prior to code execution. They control the model's complexity, speed, and generalization abilities.

Hyperparameter Tuning

To find these optimal hyperparameters, models such as Random Forest, KNN, and MLP were manually tested with various values. For other models with longer run-times, such as feedforward neural networks, automated scripts that tested various hyperparameter values were executed. Due to a code environment limitation (time-out), it was impractical to run this same code to test all hyperparameter values, such as the size of the neural network, number of layers, or learning rate. Instead, a range of diverse values were tested as the hyperparameter values, and the most effective ones closely resembled the values identified for the feedforward neural network.

In Random Forest, the number of trees was adjusted to balance model complexity and the risk of overfitting. For the bootstrapped case, fewer trees were needed since it was likely the two classes were more distinct. For KNN, the choice of k impacts model complexity; a higher k value may increase the risk of overfitting, while a lower k is generally sufficient for distinct classes.

For MLP, the architecture was defined by the size, or number of neurons, in each layer, with complexity increasing with the number of neurons. The maximum number of iterations reflects the training duration, influencing the model performance for the Feedforward Neural Network and LSTM models; vocabulary size refers to the number of words in the tweets that are being tracked and compared. The dimensionality of the dense embedding vectors, size of the hidden layer, and number of hidden layers are all aspects of complexity. The learning rate is a parameter that controls how often the model updates its weights during training; an excessively large value might prevent convergence to ideal weights, whereas an excessively small value might slow or impede convergence.

To find these optimal hyperparameters, models such as Random Forest, KNN, and MLP were manually tested with various values. For other models with longer run-times, such as feedforward neural networks, automated scripts that tested various hyperparameter values were executed. Due to a code environment limitation (time-out), it was impractical to run this same code to test all hyperparameter values, such as the size of the neural network, number of layers, or learning rate. Instead, a range of diverse values were tested as the hyperparameter values, and the most effective ones closely resembled the values identified for the feedforward neural network.

RESULTS

Metrics for Model Evaluation

The metrics used are Accuracy, Precision, Recall, F1-score and the AUC.

Accuracy is expressed as a percentage and is defined as the number of correct predictions over the total number of predictions. Precision measures the number of correct predictions out of the total number of predictions made by the model, while Recall measures the number of bullying instances that were accurately predicted by the model. The inclusion of Recall as a metric is especially helpful in minimizing false classifications for this study. The F1-score is defined as the harmonic mean of precision and recall, and it is useful because it accounts for both false positive and false negative classifications.

$$\text{Precision} = \text{True Positives} / (\text{True Positives} + \text{False Positives}) \quad (4)$$

$$\text{Recall} = \text{True Positives} / (\text{True Positives} + \text{False Negatives}) \quad (5)$$

$$\text{F1 Score} = (2 \cdot \text{Precision} \cdot \text{Recall}) / (\text{Precision} + \text{Recall}) \quad (6)$$

Model Performance Without Bootstrapping

The two tables below model performance without bootstrapping

Classification Method	Accuracy	F1-score	Precision	Recall	AUC
Logistic Regression	89.8%	0.898	0.899	0.901	0.901
SVM	89.9%	0.899	0.900	0.902	0.902
Naive Bayes	85.1%	0.851	0.851	0.853	0.853
Random Forest	89.2%	0.892	0.891	0.893	0.893
KNN	82.9%	0.828	0.846	0.837	0.837

Table 3: Non-Bootstrapped ML Classification Algorithms and Metrics.
Each classification method is evaluated using the measures of accuracy, F1-score precision, recall, and AUC. Notably, SVM shows the highest accuracy (89.9%) and AUC (0.902).

NN Method	Accuracy	F1-score	Precision	Recall	AUC
MLP	88.2%	0.881	0.881	0.883	0.882
NN	72.3%	0.733	0.734	0.735	0.735
LSTM	71.2%	0.711	0.720	0.721	0.721

Table 4: Non-Bootstrapped Neural Network Algorithms and Metrics.
Each neural network architecture method is evaluated using the measures of accuracy, F1-score precision, recall, and AUC. Notably, MLP shows the highest accuracy (88.2%) and AUC (0.882).

Model Performance With Bootstrapping

The two tables below model performance with bootstrapping.

Classification Method	Accuracy	F1-score	Precision	Recall	AUC
Logistic Regression	92.5%	0.924	0.924	0.926	0.926
SVM	94.0%	0.940	0.939	0.942	0.942
Naive Bayes	86.1%	0.861	0.860	0.862	0.862
Random Forest	96.8%	0.968	0.968	0.968	0.968
KNN	93.7%	0.937	0.937	0.939	0.939

Table 5: Bootstrapped ML Classification Algorithms and Metrics.
Each classification method is evaluated using the measures of accuracy, F1-score, precision, recall, and AUC. Notably, Random Forest shows the highest accuracy (96.8%) and AUC (0.968).

NN Method	Accuracy	F1-score	Precision	Recall	AUC
MLP	95.7%	0.957	0.956	0.958	0.958
NN	74.13%	0.741	0.741	0.741	0.741
LSTM	73.3%	0.729	0.732	0.728	0.728

Table 6: Bootstrapped Neural Network Algorithms and Metrics.
Each neural network architecture method is evaluated using the measures of accuracy, F1-score precision, recall, and AUC. Notably, MLP shows the highest accuracy (95.7%) and AUC (0.958).

Random Forest Performance Visuals

ROC graphs and confusion matrices were both created for the models that performed the best with bootstrapping.

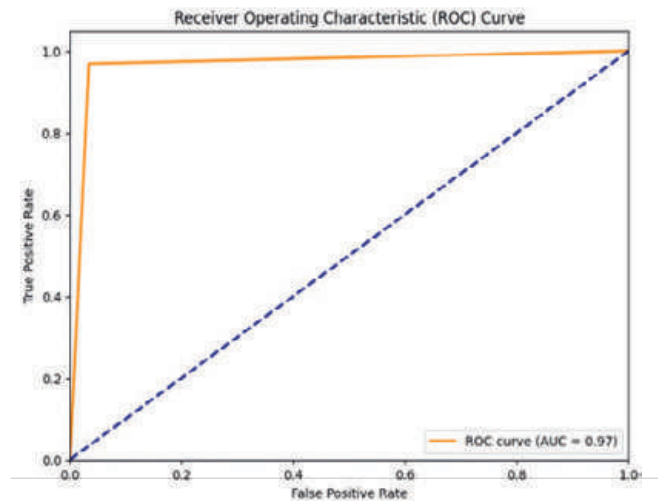


Figure 11: Random Forest Receiver Operating Characteristic (ROC) Curve.

An ROC curve shows how our model performs in the context of the False Positive and True Positive Rates. An Area Under the Curve (AUC) of 1 indicates that the model's prediction is 100% accurate. In this case, with our model, the AUC is 0.97, which indicates strong performance.

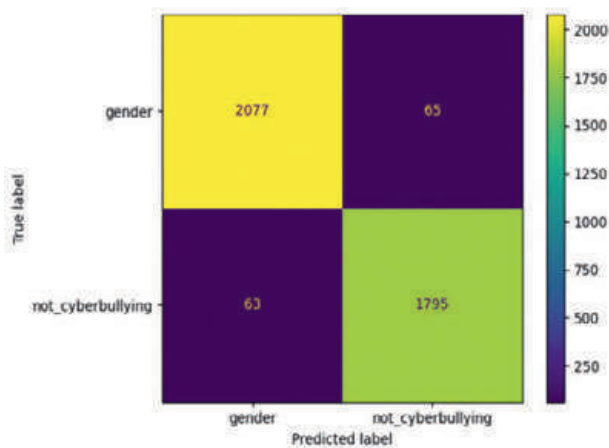


Figure 12: Random Forest Confusion Matrix.

2077 gender-bullying tweets and 1795 non-cyberbullying tweets were classified accurately using Random Forest. A false negative is when a cyberbullying tweet is classified as non-cyberbullying, whereas a false positive is when a non-cyberbullying tweet is classified as cyberbullying. It can be observed that Random Forest exhibited a balance between false positives and false negatives with 65 false negatives and 63 false positives. In the context of the diagram, lighter colors represent higher numbers while darker colors represent lower numbers. Ideally, the regions corresponding to false positives and negatives would be dark while the regions corresponding to accurate predictions would be light.

MLP Performance Visuals

ROC graphs and confusion matrices were both created for the models that performed the best with bootstrapping.

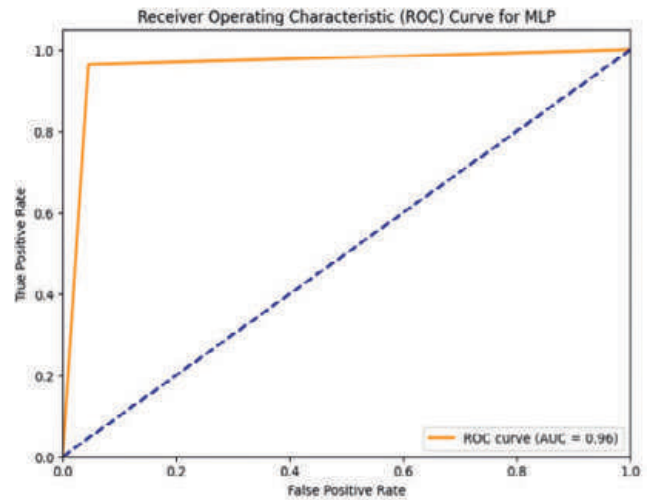


Figure 13: Multi-Layer Perceptron Neural Network (MLP) Receiver Operating Characteristic (ROC) Curve.

Just as in Figure 11, the ideal AUC would be 1 since that would mean all positives were true ones. Here the AUC is 0.96, which indicates the model's strong performance.

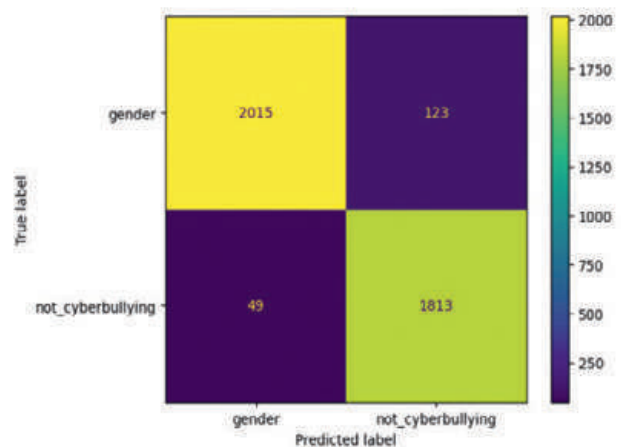


Figure 14: Multi-Layer Perceptron (MLP) Confusion Matrix.

2015 gender-bullying tweets and 1813 non-cyberbullying tweets were classified accurately. A false negative in this case is when a cyberbullying tweet is classified as non-cyberbullying, whereas a false positive is when a non-cyberbullying tweet is classified as cyberbullying. MLP showed a notable disparity, particularly with a higher count of false negatives (123). This implies that within MLP's classification, some instances of hateful comments were erroneously categorized as not cyberbullying. In the context of the diagram, lighter colors represent higher numbers while darker colors represent lower numbers. Ideally, the regions corresponding to false positives and negatives would be dark while the regions corresponding to accurate predictions would be light.

Random Forest Results

Substantial performance improvement occurred when bootstrapped data was utilized. The Random Forest model achieved an accuracy of 96.80% and an F1-score of 0.9678. Although previous studies did not emphasize gender-based bullying, Al-garadi *et al.* (2016) reported an AUC of 0.943 and an f-measure of 0.936. This indicates the effectiveness of Random Forest in accurately classifying tweets, particularly in the context of gender-based cyberbullying (7).

Survey of Machine Learning Classification

In the non-bootstrapped case, SVM performed the best with an 89.87% accuracy, F1-score of 0.8986 and AUC of 0.90. Among the Neural Network Architectures, MLP performed the best with an 88.16% accuracy, F1-score of 0.8813 and AUC of 0.88.

Every model demonstrated commendable performance with bootstrapping, each achieving an accuracy rate exceeding 85%. Among them, Naive Bayes had the lowest accuracy at 86.1%. Conversely, logistic regression proved to be significantly effective, boasting a high accuracy rate of 92.5%. The KNN model achieved an accuracy of 93.7%, while SVM outperformed it slightly with an accuracy of 94.0%. Substantial performance improvement occurred when bootstrapped data was utilized. The Random Forest model achieved an accuracy of 96.80% and an F1-score of 0.9678, making it the best performing model.

In the neural network architectures, a larger disparity of results was observed given that MLP had an accuracy of 95.70%, the Feedforward Neural Network of 74.12% and LSTM 73.3%.

DISCUSSION

The goal of this paper was to accurately predict instances of gender-based cyberbullying, coinciding with the rise of social media and internet usage. One significant aspect of this issue is the anonymity afforded by digital platforms, which emboldens perpetrators to engage in hurtful behaviors. Content moderation, with the assistance of machine learning and AI, assumes a pivotal role in addressing the problem of gender-based harassment online, with the end goal being to automate the identification of gender-based cyberbullying in tweets and enhance online safety. A previous study by Al-garadi *et al.* (2016) used specific features (network, activity, user, and content) to detect cyberbullying behavior, using publicly available tweets from California. However, given the fact that that study depended on the collection and storage of user's personal data, it could be vulnerable to breaches or potential malicious uses. Therefore, this study did not utilize any identifying information to aid in classification. After the data was split into training and testing data, the tweet text was filtered by the English language and processed to extract significant features. Subsequently, classification algorithms such as Logistic Regression, Naive Bayes, SVM, KNN, and Random Forest were applied, as well as neural network architectures such as a feedforward neural network, MLP, and LSTM. In the non-bootstrapped case, SVM performed the best with an 89.87% accuracy, F1-score of 0.8986 and AUC of 0.90. Among the Neural Network Architectures, MLP performed the best with an 88.16% accuracy, F1-score of 0.8813 and AUC of 0.88. However, with bootstrapping, the Random Forest classification method resulted in a 96.80% accuracy, F1-score of 0.9678, and AUC of 0.97. Using the MLP method with bootstrapping, a 95.70% accuracy was achieved with a F1-score of 0.9569 and AUC of 0.96.

Survey Of Machine Learning Classification

All models performed reasonably well, with each achieving an accuracy rate above 85%. Naive Bayes performed the worst, with an accuracy of 86.1%. A key characteristic of Naive Bayes and the reason for its lower performance is that it assumes independence of features. In this context, it assumes the presence of one word would not affect the presence of another; however, this is unlikely to be true since these words can combine to form stereotypes (eg: silly blonde). On the other hand, logistic regression is shown to be highly effective, given its high accuracy of 92.5%. However, a downside of this model is that logistic regression only handles linear relationships, the relationship here may not have been linear. KNN had an accuracy of 93.7%; inaccurate predictions might have arisen due to interspersed points belonging to different labels. SVM performed slightly better than Logistic Regression with an accuracy of 94.0%, likely due to its ability to handle high-dimensional data given the large amount of features and to find complex decision boundaries.

Survey Of Neural Network Architectures

It is worth noting that both the LSTM and the feedforward neural network exhibited lower accuracies compared to the other machine learning classification algorithms. Code that tested different hyperparameter values to select ideal hyperparameters was utilized for the neural network; despite this, it struggled to achieve the same level of accuracy as its counterparts due to overfitting. Additionally, LSTM took a long time to run and thus it was not feasible to test as many hyperparameters as for the other Neural Network models. Despite the potential power of more complex models like LSTM, a delicate balance has to be struck to strike, and in this case, it seems that simpler algorithms prevailed in terms of accuracy.

Limitations And Future Work

The reduction in dataset size due to English language filtering likely explains the poorer performance of the non-bootstrapped case. Additionally, Neural Network Architectures' complexity can lead to overfitting which is why the Feedforward Neural Network and LSTM didn't perform as well as the ML classification algorithms. Further studies could include further hyperparameter tuning and trying out other classification algorithms such as Gradient Boosting Algorithms. Additionally, an alternative language detection algorithm with higher accuracy may replace langdetect. Furthermore, techniques like augmentation, merging datasets, or synthetic data creation offer viable alternatives to bootstrapping for dataset expansion. Future research could explore specific sentiment analysis, including emotions like fear, anger, and sadness, coupled with an examination of users' prior activity to uncover the underlying causes of the issue and provide targeted intervention.

ACKNOWLEDGEMENTS

S.C. conceptualized and designed the study, conducted the experiments, and collected the data. S.C. also analyzed and interpreted the results and wrote the manuscript. Special thanks to Henry Austin for his training and mentorship.

CONFLICT OF INTEREST

Author declares that they have no conflicts of interest.

EDITORS

This article was reviewed by Archi Patel, Ethan Hung, Oliver Wang, Yiming Li; edited by Aniket Das, Derek Ren, Marie Yang; and laid out by Danny Zhu and Dashrit Pandher.

REFERENCES

1. M. Anderson, Teens and Tech Survey 2018 Dataset, Pew Research Center (2018). <https://www.pewresearch.org/internet/dataset/teens-and-tech-survey-2018/>
2. S. Karmakar, S. Das, "Understanding the Rise of Twitter-Based Cyberbullying Due to COVID-19 through Comprehensive Statistical Evaluation", in *Proceedings of the 54th Hawaii International Conference on System Sciences* (HICSS, 2021). doi: 10.2139/ssrn.3768839
3. J. Fox, C. Cruz, J. Y. Lee, Perpetuating online sexism offline: Anonymity, interactivity, and the effects of sexist hashtags on social media. *Comput. Hum. Behav.* **52**, 436–442 (2015). doi: 10.1016/j.chb.2015.06.024
4. E. Herry, K. L. Mulvey, Gender-based cyberbullying: Understanding expected bystander behavior online. *J. Soc. Issues.* **79**, 1210–1230 (2023). doi: 10.1111/josi.12503
5. W. Jooste, R. Haque, A. Way, Philipp Koehn: Neural Machine Translation. *Mach. Transl.* **35**, 289–299 (2021). doi: 10.1007/s10590-021-09277-x
6. M. A. Al-garadi, K. D. Varathan, S. D. Ravana, Cybercrime detection in online communications: The experimental case of cyberbullying detection in the Twitter network. *Comput. Hum. Behav.* **63**, 433–443 (2016). doi: 10.1016/j.chb.2016.05.051
7. S. Agrawal, A. Awekar, "Deep Learning for Detecting Cyberbullying Across Multiple Social Media Platforms", in *Proceedings of ECIR 2018* (Springer, Cham, 2018), pp. 141–153. doi: 10.1007/978-3-319-76941-7_11
8. J. Wang, K. Fu, C. Tien-Lu, "SOSNet: A Graph Convolutional Network Approach to Fine-Grained Cyberbullying Detection", in *Proceedings of the 2020 IEEE International Conference on Big Data* (IEEE, 2020), pp. 1699–1708. doi: 10.1109/BigData50022.2020.9378065.
9. R. P. Khandpur *et al.*, "Determining Relative Airport Threats from News and Social Media", in *Proceedings of the AAAI Conference on Artificial Intelligence* (AAAI, 2017), pp. 4701–4707. doi: 10.1609/aaai.v31i2.19097
10. L. Zhao *et al.*, Online flu epidemiological deep modeling on disease contact network. *Geoinformatica* **24**, 443–475 (2020). doi: 10.1007/s10707-019-00376-9

The Effect of a *Trpv4* Mutation on Skeletal Development in Mice

Derick Diaz¹, Lisette Nevarez¹, Daniel H. Cohn¹

¹Department of Molecular, Cell, and Developmental Biology, University of California, Los Angeles.

ABSTRACT

TRPV4 (Transient Receptor Potential Channel Vanilloid 4) is a tetrameric calcium-permeable nonselective cation channel. It plays a critical role in regulating responses from known activators of the channel including mechanical stimuli, high temperatures, natural and synthetic ligands, and hypo-osmotic solutions, providing an important biological function in cartilage cells (chondrocytes). Missense mutations in *TRPV4* cause a spectrum of skeletal dysplasias of increasing severity including brachyolmia, spondylometaphyseal dysplasia, Kozlowski type (SMDK), and metatropic dysplasia. Although the genetic bases of these diseases have been established, studies have yet to establish an animal model to study the mechanism by which the *TRPV4* mutation produces disease. To effectively produce a non-lethal skeletal phenotype that modeled a human disorder, a conditional knock-in mouse model was generated using the *Trpv4* p.R594H mutation, which produces the moderately severe SMDK human phenotype. Postnatal induction in chondrocytes at weaning, using *Acan-CreER* (Estrogen Receptor) and tamoxifen, produced mice with significantly shorter femora, humeri, hip bones, tibiae, tail lengths, and lumbar vertebral heights in comparison to wild-type (WT) mice. Midgestational induction of the same mutation in chondrocytes using *Col2a1-Cre* resulted in mice with significantly shorter femora, humeri, hip bones, tibiae, lumbar vertebral heights, body length, and tail lengths. Qualitative analysis revealed abnormal metaphyses, craniofacial features, widened and smaller vertebral bodies, and shorter long bones in mutant (Mut) mice. Overall, the *Trpv4* p.R594H mutation has been shown to shorten skeletal elements and produce abnormal skeletal development in Mut mice compared to wild-type mice. Thus, there is evidence of an effective animal model for a *TRPV4* human skeletal disorder, which advances our understanding of the effects of *TRPV4* mutations on skeletal development. Further studies using this mouse model could include tests of inhibitor treatments to prevent disease progression of the *TRPV4* skeletal disorders.

INTRODUCTION

Skeletal dysplasias are a heritable group of more than 450 detailed disorders that have generalized abnormalities in primarily bone and cartilage (1). Activating mutations in *TRPV4* have been found to cause a spectrum of skeletal dysplasia phenotypes (2). TRPV4 is a tetrameric, calcium-selective, gated ion channel that plays a role in chondrocyte differentiation and is selectively expressed in chondrocytes. However, it is also expressed at lower, but still biologically significant, levels in other cell types (3). Point mutations in *TRPV4* cause disorders consisting of mild to lethal dominantly inherited skeletal dysplasia phenotypes. These conditions, in order of increasing clinical severity, include familial digital arthropathy-brachydactyly, autosomal dominant brachyolmia, SMDK, non-lethal metatropic dysplasia, and the perinatal lethal form of metatropic dysplasia (3). Although current treatment methods such as physical therapy and surgery are appropriate, they are not curative (2).

Since *TRPV4* mutations cause disorders predominantly in the developing skeleton, a viable animal model system is needed to assess the phenotypic consequences of mutant TRPV4 in anatomically similar organisms, such as mice, to compare to human patients with *TRPV4* skeletal disorders. Although a milder *Trpv4* mutation has been studied, using a viable animal model

to study its more severe effects on skeletal growth has yet to be conducted. Therefore, to understand a severe mutation that can still be studied in a viable animal model, SMDK was chosen. SMDK is a moderately severe disorder characterized by pronounced short stature, excessive curvature of the upper spine, and short limbs. Radiographically, platyspondyly and broader vertebral bodies within the spine are observed, while metaphyseal irregularity and flaring are observed in the limbs of SMDK patients (5). Specifically, the R594H missense mutation was chosen, as it is the most common mutation found in SMDK patients. In previous studies, mutation analysis of six SMDK patients demonstrated heterozygosity for missense mutations in TRPV4 in all patients, with one mutation leading to an R594H substitution recurring in 4 patients (6). Since these skeletal dysplasias are caused by gain-of-function mutations in *TRPV4* (3), the SMDK disorder in humans was modeled using a transgenic mouse construct with CRE-recombinase (CRE).

CRE is a widely used scientific tool that recombines floxed alleles of transgenes and other genetic constructs, such as knock-in constructs, which would allow the activation of the mutant *Trpv4* and cause skeletal dysplasia in mice (7). Upon initial testing with CRISPR (Clustered Regularly Interspaced Short Palindromic Repeats) knock-in mice, it was observed that global activation of the mutation was consistently lethal. Therefore, subsequent

experiments employed conditional (tissue-specific) CRE activation, which would allow for isolation of the effects of the *Trpv4* mutation on skeletal development. Combining the CRISPR construct along with CRE activation, the conditional CRE model allowed control over where and when the mutation would be activated to affect only chondrocyte development.

The objective was to use a conditional knock-in mouse model to determine if the SMDK disorder observed in humans could be accurately recapitulated in mice. It was hypothesized that mice carrying the mutant p.R594H *Trpv4* allele would exhibit abnormal skeletal elements compared to their unaffected (WT) counterparts with wildtype *Trpv4*, thereby recapitulating the phenotype of a human TRPV4 skeletal disorder. After both WT and Mut *Trpv4* mice grew to about 7-8 weeks of age, they were both collected and radiographed to assess the effect of mutant *Trpv4* on the developing skeleton. By further understanding the disorder in a model system, the new information could be used to test inhibitors on mice with mutant *Trpv4*, with a longer-term goal of treating people with a TRPV4 skeletal disorder in a clinical setting.

MATERIALS/METHODS

Trpv4 Construct

The goal was to create a mouse model that replicates the skeletal dysplasia phenotype after activating the *Trpv4* mutation. To that end, two CRE transgenic mouse lines were created: 1) the *Acan-CreER* model in which the mutation was activated at P21, and 2) the *Col2a1-Cre* model in which the mutation was expressed after E9.5. To produce a *Trpv4* Mut mouse, with the Jackson Laboratories, an allele construct was designed using CRISPR technology (8). The construct replaced one of the wildtype *Trpv4* alleles with a modified allele that expressed WT *Trpv4*, but incorporated the p.R594H mutation that could only be expressed after induction with *Cre* recombinase. The mouse with the inserted *Trpv4* mutant construct was then bred with a mouse that had a selected *Cre*. In the presence of *Cre*, the section of the construct encoding WT *Trpv4* is removed, allowing the p.R594H mutation to be expressed instead. Thus, the combination of chondrocyte-specific *Cre* expression and the specific *Trpv4* mutant construct was generated to create a mouse model that could recapitulate the effects of heterozygosity only present in chondrocytes for a mutation seen in SMDK patients.

Cre-recombinase

Two transgenic *Cre* models were used to activate the mutation, one using the Aggrecan (*Acan*) promoter and the other using the type II collagen (*Col2a1*) promoter. Both models were selected for their specificity of expression in chondrocytes. The *Acan-CreER* model requires activation via tamoxifen, which was used to treat mice after 21 days of age at weaning. For this model, all mice were females due to the limited availability of male mice, and all protocols involving mice were IACUC approved. The *Col2a1-Cre* transgene is typically expressed at 9.5 days gestation (9) and does not require tamoxifen for activity, allowing the assessment of mutation effects earlier in development. Mice of both sexes were assessed for this mutant. For both models, the mice were collected at 7-8 weeks of age.

ImageJ Analysis

To assess skeletal phenotype, anteroposterior radiographs using a Faxitron model LX-60 cabinet X-ray machine were taken immediately after the collection and skeletal preparation of mice. Radiograph

screenshots were extracted and imported into the image analysis application, ImageJ. Size calibrations for the global scale, a scale allowing all skeletal element measurements from each mouse to be consistent, were determined from direct measurements of the mouse's body length (nose to beginning of tail in centimeters). From there, skeletal elements were measured using the line function, a function that created a line from one point to another and measured it using the global scale calibration. This was based on the X-ray annotation mouse atlas, an atlas separate from ImageJ used to locate standardized skeletal elements of a mouse (10). The skeletal elements measured included long bones, vertebral bodies, tail lengths, and body lengths. Using the radiographs, qualitative analysis, including observation of abnormal shapes of standard skeletal elements and the shortening or flatness of certain skeletal elements when compared to the unaffected mouse, was also performed to examine the skeletal structure of Mut mice compared to unaffected mice. Long bones, vertebral bodies, tail lengths, and body lengths previously mentioned were chosen to be measured to act as a standard representation of skeletal abnormalities commonly found in human SMDK patients.

Excel Statistical Analysis

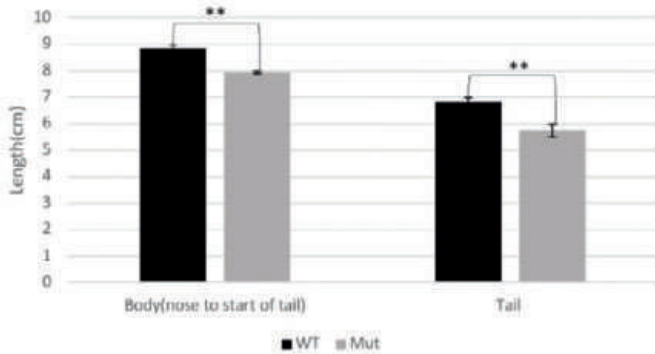
The measurements were grouped and compared according to same-sex and relative age for each mouse model. Using Microsoft Excel, average, standard deviation, standard error, variance, 2-sample variance test, and an unpaired student's t-test were calculated for each measured element to determine the significance of the data. For the *Acan-CreER* model in females, the two groups compared were unaffected mice (n=6) and tamoxifen-activated Mut mice (n=2). For the *Col2a1-Cre* model, the two groups compared were unaffected mice (n=6 for females, n=7 for males) and the Mut TRPV4 mice (n=3 for females, n=8 for males).

RESULTS

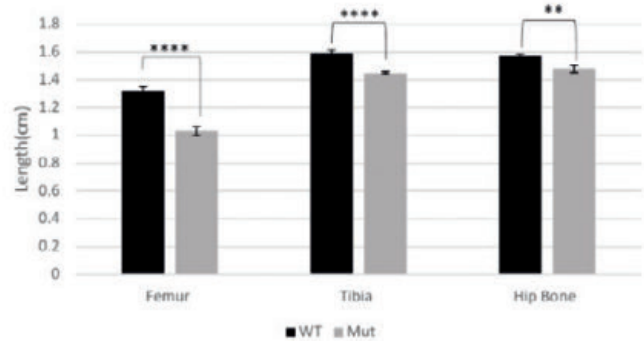
Reduced Skeletal Size in TRPV4 Mutant Female Mice: *Acan-CreER* Model

Radiographs of unaffected and Mut female mice in the *Acan-CreER* model were compared via body measurements in both a quantitative and qualitative manner. Comparison of unaffected (n=6) and tamoxifen-activated Mut mice (n=2) through an unpaired student's t-test demonstrated that Mut mice were significantly smaller in size than unaffected mice in terms of skeletal elements of interest (Figure 1). For body length (WT = 8.85cm, Mut = 7.95cm, $p < 0.01$), tail length, femora length (WT = 1.323cm, Mut = 1.032cm, $p < 0.0001$), tibiae length, hip bone length, lumbar vertebral body 1-6 (L1-L6) height (L6: WT = 0.275cm, Mut = 0.220cm, $p < 0.001$), sacral vertebral body (S1-S4) height (taken as one measurement), and caudal vertebral body (C1-C6) height, Mut mice were significantly smaller than unaffected mice (Figure 1A-1B, 1D-1E). However, for cranium width, L1-L4 width, and C1-C6 width, there was no significant difference between Mut and unaffected mice (Figure 1C, 1E). From the radiographs, there were qualitative differences between the Mut and affected mice (Figure 2). Mut mice were significantly and observably smaller in body size, having shorter long bones and shorter vertebral bodies (Figure 1, 2A-2C). Qualitative analysis of the metaphyses revealed abnormally shaped metaphyses in affected mice, similar to the flared metaphyses observed in human SMDK patients (Figure 2D).

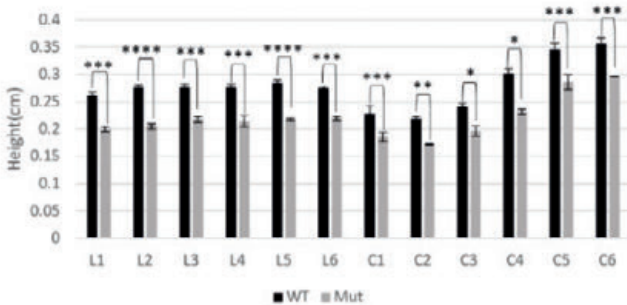
(A)



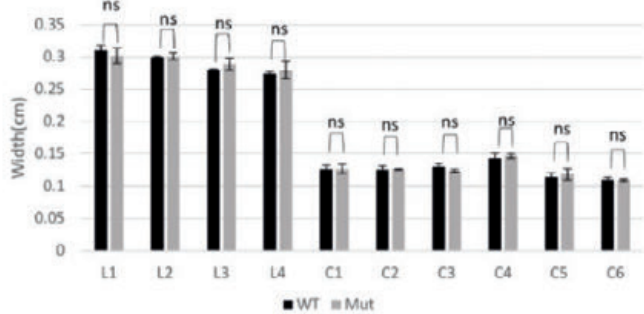
(B)



(C)



(D)



(E)

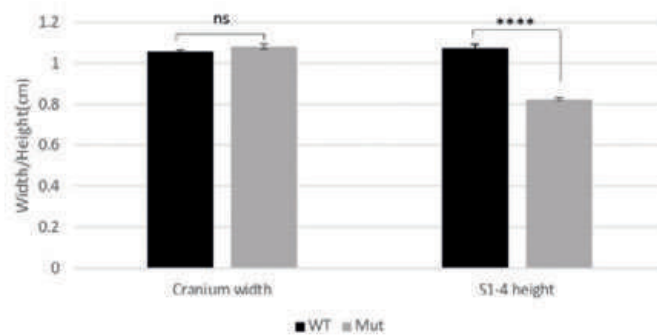


Figure 1: TRPV4 mutant female mice show significantly smaller skeletal elements compared to unaffected mice in the *Acan-CreER* model.

Acan-CreER female mice were radiographed and had various skeletal elements measured in centimeters using the image analysis application ImageJ. Measurements were recorded between unaffected mice with WT TRPV4 and Mut mice with Mut TRPV4 and then put through an unpaired student's t-test to determine the p-value for statistical significance (unaffected/WT n=6; Mut n=2; Data expressed as means \pm SE. Significance of the differences: ns= $p>0.05$; *= $p<0.05$; **= $p<0.01$; ***= $p<0.001$; ****= $p<0.0001$). (A) Average body and tail length in Mut mice were significantly smaller compared to unaffected mice ($p<0.01$). (B) Average long bone length was significantly smaller in Mut mice compared to unaffected mice ($p<0.0001$, $p<0.01$). (C) Average lumbar and caudal vertebral heights were significantly smaller in Mut mice compared to unaffected mice ($p<0.05$; $p<0.01$, $p<0.001$, $p<0.0001$). (D) Average lumbar and caudal vertebral bodies were not significantly different between Mut and unaffected mice ($p>0.05$). (E) Average cranium width was not significantly different between Mut and unaffected mice ($p>0.05$). Average sacral vertebral body 1-4 (taken as one measurement) height was significantly smaller in Mut mice compared to unaffected mice ($p<0.0001$).

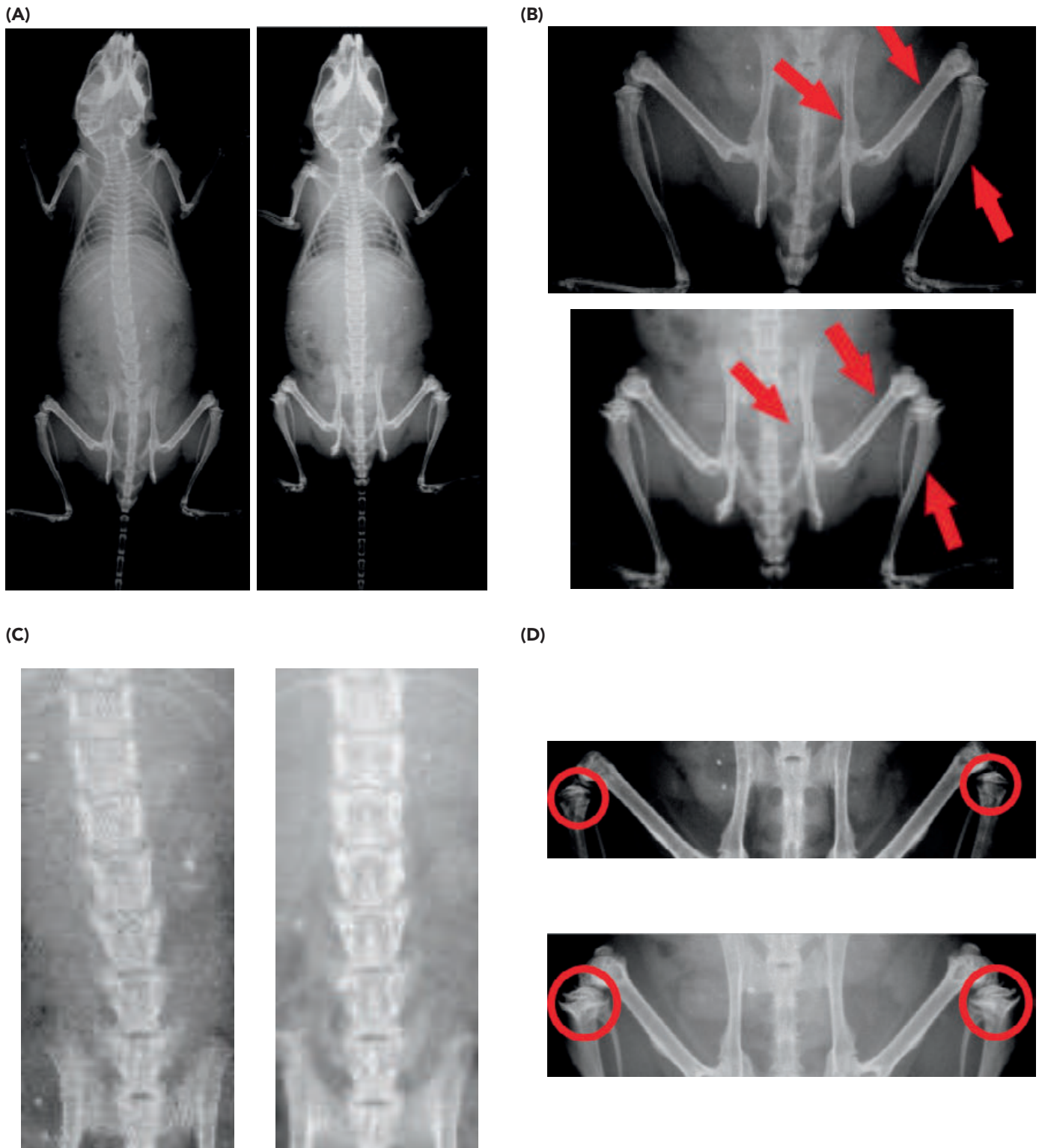


Figure 2: Radiographs of TRPV4 Mut female mice suggest moderate skeletal dysplasia compared to unaffected mice in the *Acan-CreER* model.

Acan-CreER female mice were radiographed in various areas to observe the effect of the TRPV4 mutation. Specifically, full body (A), long bones (B), vertebral bodies (C), and metaphyses (D) were compared. (A) WT (left) vs Mut (right): The Mut mouse was observably smaller in size than the unaffected mouse. (B) WT (top) vs Mut (bottom): Long bones (indicated by the red arrows) were observably shorter in the Mut mouse than the unaffected mouse. (C) WT (left) vs Mut (right): Lumbar vertebral bodies in Mut mouse were observably smaller compared to the unaffected mouse. (D) WT (top) vs Mut (bottom): Metaphyses (indicated by red circles) appear abnormal, appearing as an umbrella shape, compared to the unaffected mouse.

Smaller Skeletal Elements in TRPV4 Mutant Mice: *Col2a1-Cre* Model

Radiographs of unaffected and Mut female and male mice in the *Col2a1-Cre* model were compared via body measurements in both a quantitative and qualitative manner. An unpaired student's t-test revealed that Mut TRPV4 mice (n=3 for females, n=8 for males) were significantly smaller than unaffected mice (n=6 for females, n=7 for males) in both males and females (Figure 3, 4). In female mice, body length (WT = 8.55cm, Mut = 7.23cm, $p<0.0001$), tail length, femora (WT = 1.251cm, Mut = 1.084cm, $p<0.001$), tibiae, hip bones, L1-L6 height (L6: WT = 0.268cm, Mut = 0.194cm, $p<0.000001$), S1-4 height (as one measurement), and C1-C6 height, Mut mice were significantly smaller than unaffected mice (Figure 3A-3B, 3D-3E). Mut mice had significantly wider average caudal 2 (C2) and cranial width compared to unaffected mice (Figure 3C, 3E). For L1-L4 width, C1 width, and C3-C6 width, there was no significant difference between Mut and unaffected mice (Figure 3C). In male mice, Mut mice had significantly shorter average body lengths (WT = 8.72cm, Mut = 7.76cm, $p<0.001$), tail lengths, femora (WT = 1.181cm, Mut = 1.032cm, $p<0.001$), tibiae, hip bones, L1-L6 heights (L6: WT = 0.276cm, Mut = 0.212cm, $p<0.000001$), L4 widths, S1-4 heights (as one measurement), and C1-C6 heights compared to unaffected mice (Figure 4A-B, D-E). Mut mice had significantly wider average cranium widths, L1 widths, and C1-C2 widths than unaffected mice (Figure 4C, 4E). For L2-L3 width and C3-C6 width, there was no significant difference between Mut and unaffected mice (Figure 4C). From the radiographs, there were substantial qualitative differences between the Mut and unaffected mice (Figure 5, 6). Mut mice were significantly smaller, had a much wider, dome-shaped craniofacial structure, notably shorter long bones, and abnormal appearing vertebral bodies (Figure 5A-5D, 6A-6D), all of which are substantiated by quantitative measurements (Figure 3, 4). As observed for the *Acan-CreER* mice, qualitative analysis again showed metaphyseal abnormalities comparable to the flared metaphyses characterized in SMDK patients (Figure 5E, 6E).

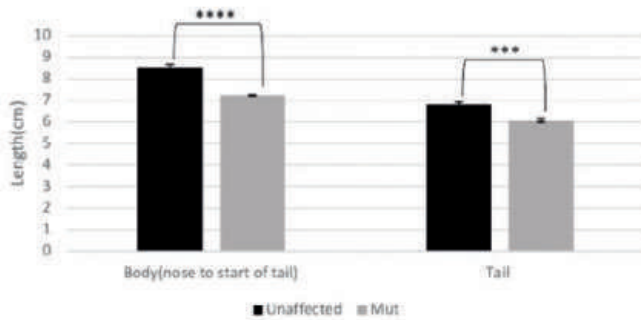
DISCUSSION

The goal of this study was to explore if both the *Acan-CreER* and *Col2a1-Cre* mouse models could accurately recapitulate the SMDK disorder seen in human patients. In the *Acan-CreER* model, with the exception of vertebral body width, postnatal expression of the p.R594H *Trpv4* mutation resulted in statistically significant (p -value less than 0.05) shortening of all skeletal elements measured within Mut mice. This data suggests that the p.R594H *Trpv4* mutation was able to successfully recapitulate the phenotypic effects of SMDK seen in human patients, even when the mutation was activated postnatally through the activation of CRE using tamoxifen. However, due to later activation of the mutation during development, the mutation was only allowed to take effect for about 3-4 weeks, not allowing the mutation sufficient time to have a more severe effect on the developing skeleton. Human subjects afflicted with SMDK vary in age, but in a clinical study of 6 patients with SMDK, ages ranged from 8 months to 9 years (6). This age range, compared to the age range of the mouse models, appears to be much wider and could account for the lack of some effects not seen in the measurements. In the *Col2a1-Cre* model, for both female and male mice, prenatal expression of the mutation resulted in significant shortening of all skeletal lengths/heights measured, including significant widening

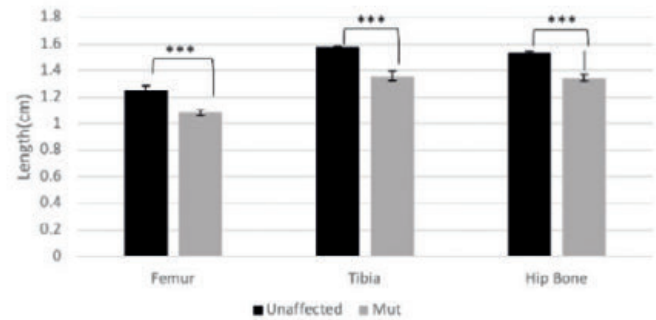
of some vertebral bodies. A possible explanation for the non-statistical significance in most of the vertebral body widths is that the mutation was not allowed enough time to take effect on the width of the vertebral bodies. Even in the *Col2a1-Cre* model, although the mutation was induced embryonically, the mice were still given only 7-8 weeks for the mutation to take effect when mouse development stopped around 12-24 weeks (11). Overall, data from both the male and female studies suggests that the R594H *Trpv4* mutation can successfully recapitulate the phenotypic effects of SMDK seen in patients, especially when the mutation is activated much earlier in prenatal development. A statistical analysis of the degree of severity when comparing the *Acan-CreER* Mut mice to the *Col2a1-Cre* Mut mice was never performed. However, qualitative analysis of radiographs suggests that when the mutation is activated much earlier in development (as in the *Col2a1-Cre* model), craniofacial abnormalities develop that are not observed in the *Acan-CreER* model. However, both prenatal and postnatal activation of the mutation show significant shortening of both the axial and appendicular skeleton. Thus, both models provide evidence that expression of the R594H *Trpv4* mutation effectively mirrors skeletal abnormalities consistent with those observed in the SMDK disorder in human patients.

Although this study was able to generate a successful model of recapitulating the SMDK disorder, several limitations were observed that influenced the results. First, radiographs produced by the Faxitron X-ray often had lighting and resolution issues that introduced difficulties for measuring certain areas of the body, such as the vertebral bodies, and specifically the individual sacral vertebral bodies. Although using ImageJ somewhat corrected the lighting issue (by manually adjusting the brightness and contrast features) when measuring, some lighting and resolution issues remained recurrent problems that made quantitative measurements less precise. An example of this problem was when S1-4 could only be used as one measurement, as in taking a single measurement starting from the beginning of S1 to the end of S4, since distinguishing the boundaries between each vertebral body was too difficult. Another limitation of this study was the sample size. With the exception of the *Col2a1-Cre* male mice sample size, the sample sizes for the *Col2a1-Cre* (n=3 Mut mice) and *Acan-CreER* (n=2 Mut mice) models lacked Mut mice compared to their unaffected counterpart groups due to genetic and breeding factors. Due to this, the *Acan-CreER* male mice could not be studied and could have possibly influenced the results of the mice studied. As mentioned previously, radiographs of SMDK patients demonstrate platyspondyly and broader vertebral bodies in the spine, as well as irregular metaphyses in the limbs. The data generated from both models suggest similar symptoms in R594H *Trpv4* Mut mice, revealing a phenotypic consistency between Mut mice and SMDK patients. Since the mutations that produce the TRPV4 skeletal disorders result in channel activation (3), it was predicted that inhibitors of the TRPV4 channel (12) could be used to treat mice expressing mutant *Trpv4* to ameliorate the severity of the skeletal phenotype. For example, a TRPV4 mutation that would normally cause neonatal lethality could be reduced to a milder phenotype, such as brachyolmia. It is speculated that models similar to those generated in this study could be used to recapitulate other TRPV4 disorders, such as metatropic dysplasia due to their similar phenotypic natures, and subsequently be used for inhibition studies. If the inhibitor leads to a significant reduction in phenotypic severity, clinical applications of eventually treating people with TRPV4 skeletal disorders would be possible.

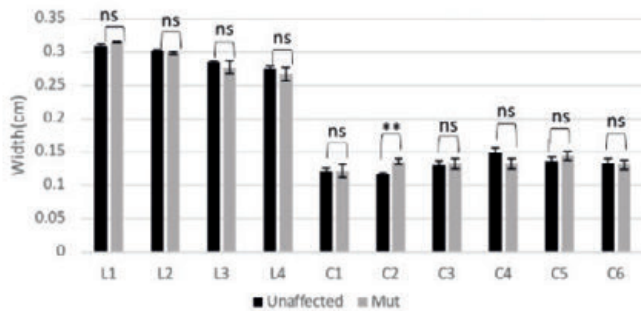
(A)



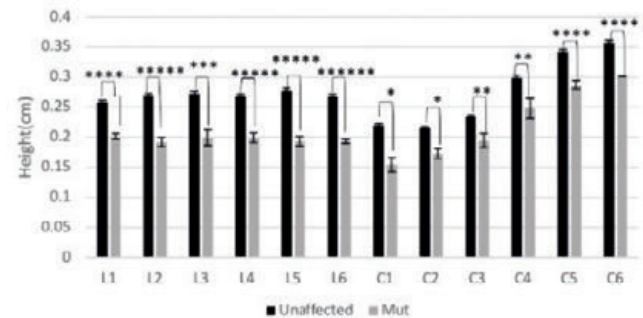
(B)



(C)



(D)



(E)

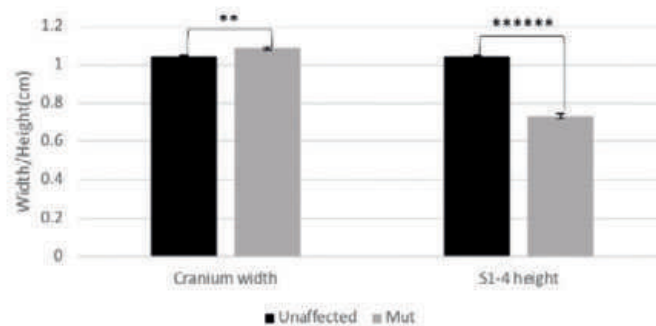
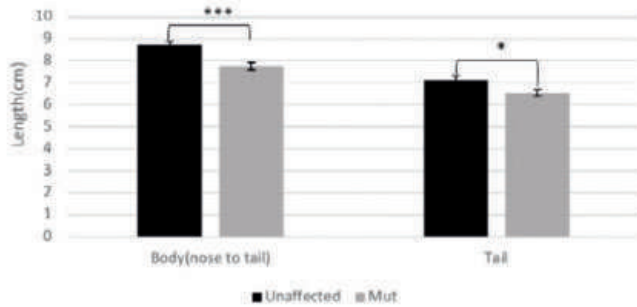


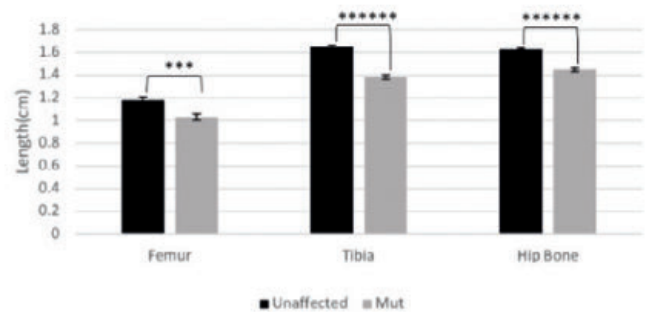
Figure 3: TRPV4 mutant female mice show significantly smaller skeletal elements compared to unaffected mice in the *Col2a1-Cre* model.

Col2a1-Cre female mice were radiographed and had various skeletal elements measured in centimeters using the image analysis application ImageJ. Measurements were recorded between unaffected mice with WT TRPV4 and Mut mice with Mut TRPV4. An unpaired student's t-test was then used to determine the p-value for statistical significance (unaffected/WT n=6; Mut n=3). (A) Average body and tail length in Mut mice were significantly smaller compared to unaffected mice ($p<0.0001$, $p<0.001$). (B) Average long bone length was significantly smaller in Mut mice compared to unaffected mice ($p<0.001$). (C) Average lumbar and caudal vertebral widths showed no statistically significant difference between Mut and unaffected mice for all lumbar vertebral bodies and caudal vertebral bodies with the exception of caudal vertebral body 2 (C2) ($p<0.05$). The average C2 width was significantly wider in Mut mice compared to unaffected mice ($p<0.01$). (D) Average lumbar and caudal vertebral body heights were significantly smaller in Mut mice compared to unaffected mice ($p<0.05$, $p<0.01$, $p<0.001$, $p<0.0001$, $p<0.00001$, $p<0.000001$). (E) Average cranium width was significantly wider in Mut mice compared to unaffected mice ($p<0.01$). Average sacral vertebral body height from 1-4 (taken as one measurement) was significantly smaller in Mut mice compared to unaffected mice ($p<0.000001$).

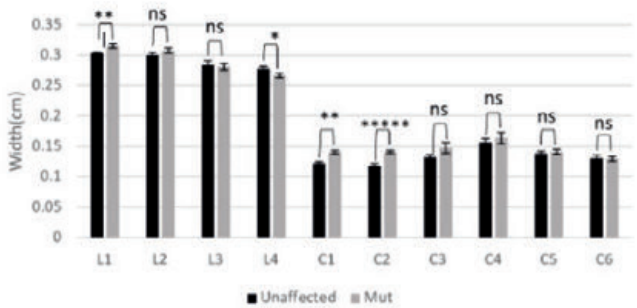
(A)



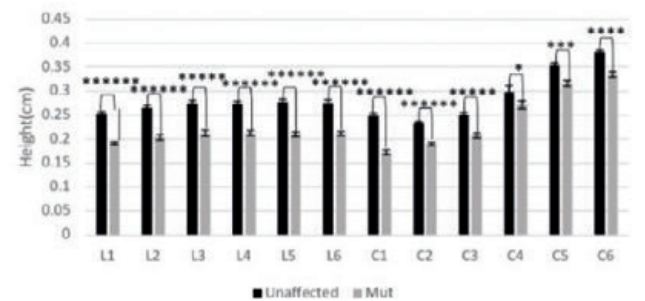
(B)



(C)



(D)



(E)

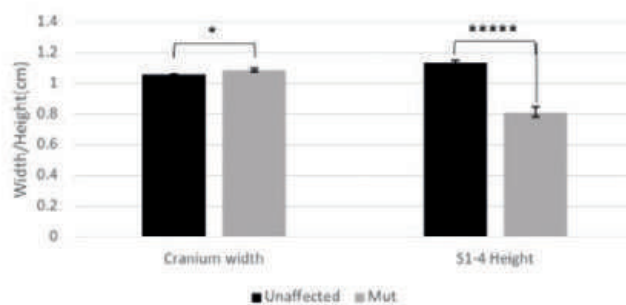


Figure 4: TRPV4 Mut male mice show significantly smaller skeletal elements compared to unaffected male mice in the *Col2a1-Cre* model.

The same procedure, as described in Figure 3 for *Col2a1-Cre* female mice, was done for *Col2a1-Cre* male mice (unaffected/WT n=6; Mut n=3). (A) Average body and tail length in Mut mice were significantly smaller compared to unaffected mice ($p<0.001$, $p<0.05$). (B) Average long bone length was significantly smaller in Mut mice compared to unaffected mice ($p<0.001$, $p<0.000001$). (C) Average lumbar and caudal vertebral widths showed no statistically significant difference between Mut and unaffected mice for all lumbar vertebral bodies and caudal vertebral bodies with the exception of Lumbar vertebral body 1 (L1), L4, C1, and C2 ($p>0.05$). The average L1, C1, and C2 widths were significantly wider in Mut mice compared to unaffected mice ($p<0.01$, $p<0.00001$). The average L4 width was significantly shorter in Mut mice compared to unaffected mice ($p<0.05$). (D) Average lumbar and caudal vertebral body heights were significantly smaller in Mut mice compared to unaffected mice ($p<0.05$, $p<0.001$, $p<0.0001$, $p<0.00001$, $p<0.000001$). (E) Average cranium width was significantly wider in Mut mice compared to unaffected mice ($p<0.05$). Average sacral vertebral body 1-4 (taken as one measurement) height was significantly smaller in Mut mice compared to unaffected mice ($p<0.00001$).



Figure 5: Radiographs of TRPV4 Mut female mice suggest moderate skeletal dysplasia compared to unaffected female mice in the *Col2a1-Cre* model. *Col2a1-Cre* female mice were radiographed in various areas to observe the effect of the TRPV4 mutation. Specifically, full body (A), craniofacial features (B), long bones (C), vertebral bodies (D), and metaphyses (E) were compared. **(A)** WT (left) vs Mut (right): The Mut mouse was observably smaller in size than the unaffected mouse. **(B)** WT (left) vs Mut (right): Mut mouse has a dome-shaped, wider head compared to the normal cranium shape seen in the unaffected mouse. **(C)** WT (top) vs Mut (bottom): Long bones (indicated by red arrows) are observably shorter in the Mut mouse compared to the unaffected mouse. **(D)** WT (left) vs Mut (right): Lumbar vertebral bodies in Mut mouse are observably smaller compared to the unaffected mouse. **(E)** WT (top) vs Mut (bottom): Metaphyses (indicated by the red circles) appear abnormal, appearing as an umbrella shape, compared to the unaffected mouse.

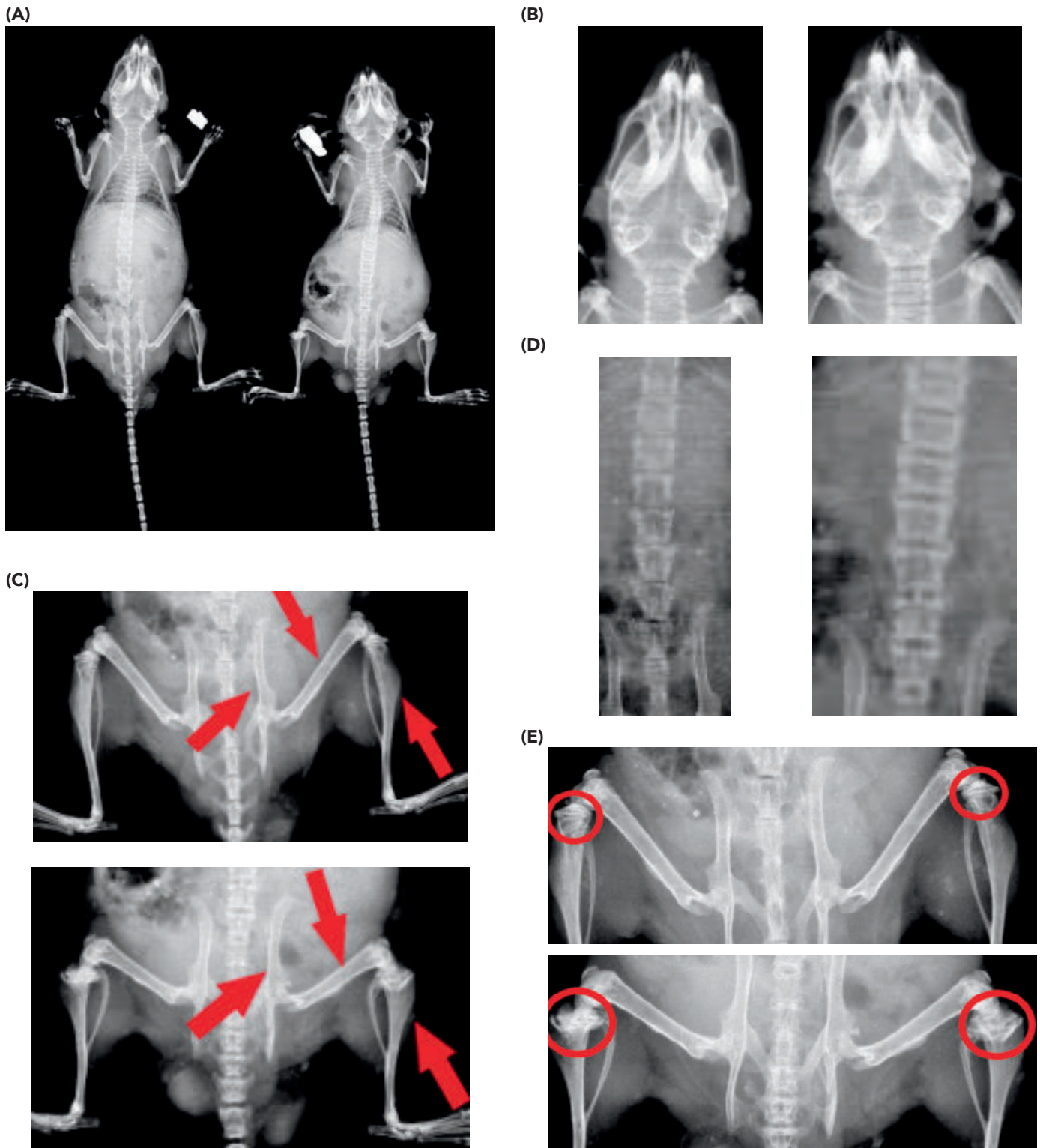


Figure 6: Radiographs of *TRPV4* Mut male mice suggest moderate skeletal dysplasia compared to unaffected male mice in the *Col2a1-Cre* model.

Col2a1-Cre male mice were radiographed in various areas to observe the effect of the *TRPV4* mutation. Specifically, full body (A), craniofacial features (B), long bones (C), vertebral bodies (D), and metaphyses (E) were compared. (A) WT (left) vs Mut (right): The Mut mouse is observably smaller in size than the unaffected mouse. (B) WT (left) vs Mut (right): Mut mouse has a dome-shaped, wider head compared to the normal cranium shape seen in the unaffected mouse. (C) WT (top) vs Mut (bottom): Long bones (indicated by arrows) are observably shorter in the Mut mouse compared to the unaffected mouse. (D) WT (left) vs Mut (right): Lumbar vertebral bodies in Mut mouse are observably smaller and wider compared to the unaffected mouse. (E) WT (top) vs Mut (bottom): Metaphyses (indicated by the red circles) appear abnormal, appearing as an umbrella shape, compared to the unaffected mouse.

ACKNOWLEDGMENTS

I would like to thank the Maximizing Access to Research Careers (MARC) program, as well as the Cohn Lab for funding and assistance during this study. There were no conflicts of interest to report for this study.

EDITORS

This article was reviewed by Caden Chow, Eliana Bohn, Joanna Rhim, and Mahek Shah, edited by Gia Boisselier and Kyle Nguyen-Ngo, and laid out by Truman Ma.

REFERENCES

1. D. Krakow, Skeletal dysplasias. *Clin Perinatol*. **42**(2):301-19 (2015).
2. B. A. McCray, A. Schindler, J. E. Hoover-Fong, C. J. Sumner, Autosomal Dominant TRPV4 Disorders. *GeneReviews* [Internet] (2020).
3. M. M. Weinstein, S. W. Thompson, Y. Chen, B. Lee, D. H. Cohn, Mice expressing mutant Trpv4 recapitulate the human TRPV4 disorders. *J Bone Miner Res*. **29**, 1815-1822 (2014).
4. H. A. Leddy *et al.*, Follistatin in chondrocytes: the link between TRPV4 channelopathies and skeletal malformations. *FASEB J*. **28**(6), 2525-37 (2014).
5. #184252 SPONDYLOMETAPHYSEAL DYSPLASIA, KOZLOWSKI TYPE; SMDK, Clinical Synopsis. <https://www.omim.org/clinicalSynopsis/184252>
6. D. Krakow *et al.*, Mutations in the gene encoding the calcium-permeable ion channel TRPV4 produce spondylometaphyseal dysplasia, Kozlowski type and metatropic dysplasia. *Am J Hum Genet*. **84**(3):307-15 (2009).
7. G. D. Van Duyne, Cre Recombinase. *Microbiol Spectr*. **3**(1):MDNA3-0014-2014 (2015).
8. V. T. Chu *et al.*, Efficient generation of Rosa26 knock-in mice using CRISPR/Cas9 in C57BL/6 zygotes. *BMC Biotechnol*. **16**:4 (2016).
9. K. Sakai *et al.*, Stage- and tissue-specific expression of a Col2a1-Cre fusion gene in transgenic mice. *Matrix Biol*. **19**(8):761-7 (2001).
10. J. Ruberte, A. Carretero, H. Cater, G. Gràcia, C. Lally, X Ray Annotation Mouse Atlas. *Doctor Herriot S.L* (2021).
11. K. Flurkey, J. M. Currer, D. E. Harrison, The mouse in biomedical research. *American College of Laboratory Animal Medicine series* (2007).
12. H. A. Leddy, A. L. McNulty, F. Guilak, W. Liedtke, Unraveling the mechanism by which TRPV4 mutations cause skeletal dysplasias. *Rare Dis*. **30**;2(1):e962971 (2014).

How Low Can the Uranus Flagship Fly?

Shaya Naimi¹, Julie Castillo-Rogez¹, Mark Hofstadter¹

¹NASA Jet Propulsion Laboratory.

ABSTRACT

In the early planning stages of a mission, scientists seek a tool that estimates the torque that a spacecraft experiences due to atmospheric drag as it flies through an atmosphere. If this torque is greater than the torque supplied by the spacecraft's Reaction Control Subsystem (RCS), it can interfere with the spacecraft's attitude control and communication. For the upcoming Uranus Flagship, this problem is especially relevant because flying deep into Uranus's atmosphere will allow the spacecraft to avoid collisions with dangerous ring particles and enable more accurate data collection. However, at low altitudes, the gas giant's atmosphere becomes dense enough to threaten attitude control. Using existing calculations from the Cassini-Huygens mission as a model, this study aims to determine how low a spacecraft similar in construction to Cassini can fly in Uranus's atmosphere while maintaining attitude and reaction control capabilities. To solve this problem, this study produced a software tool called the Preliminary Atmospheric Torque Calculation Tool (PATCaT) that provides a simple way to calculate atmospheric torque on any planet given an atmospheric density profile, atmospheric conditions, and parameters describing the spacecraft. PATCaT was developed by using the standard atmospheric torque equation to calculate the torque that a spacecraft experiences in a given atmosphere. Using PATCaT, the study concluded that there is a safe zone in between Uranus's innermost known ring and the altitude at which the spacecraft would no longer be able to overcome atmospheric torque and tumble out of control. In particular, a spacecraft may be able to fly as low as 184 km above the 1-bar level in Uranus's atmosphere. The insight gained from PATCaT can enable the Uranus Flagship and future missions to avoid dangerously low altitudes and use thrusters strong enough to overcome the expected torque on a spacecraft.

INTRODUCTION

This study is a contribution to the early planning stages of NASA's 2023 Uranus Flagship mission. This mission aimed to send a spacecraft deeper into the Uranus atmosphere than any other earlier spacecraft to uncover the mysteries of the origins and evolution of the ice giant. While flying at the lowest possible safe altitude on Uranus allows for more robust data collection, two main risks complicate flying at low altitudes. First, Uranus has rings with particles that could damage the spacecraft, so the spacecraft's trajectory is limited to regions where it will not encounter ring particles. The second obstacle, the focus of this paper, is that flying at low altitudes introduces torque on the spacecraft due to its center of mass and center of torque being misaligned relative to its direction of motion. It is essential that the spacecraft is capable of overcoming this torque using its Reaction Control Subsystem (RCS) and in order to maintain the necessary orientation for continuous communication with Earth. Ultimately, this study investigates the hypothesis that there is an altitude range in Uranus's atmosphere in which a spacecraft can be safely flown without risking ring particle collisions or loss of attitude control by determining, at varying altitudes, how much force will be required by the spacecraft's RCS thrusters to overcome the torque applied to the spacecraft due to atmospheric drag.

Previous work on a similar problem exists from the Cassini-

Huygens spacecraft, which launched in 1997. After completing its Titan flyby in 2017, Cassini was driven deep into Saturn's atmosphere to avoid collision with the potentially habitable moons in the vicinity. During this phase, Cassini orbited Saturn five times before making the catastrophic plunge into the planet's atmosphere. As it descended into lower altitudes, the spacecraft experienced atmospheric torque, tumbled out of control, and lost communication with Earth. Cassini's plunge yielded the most reliable data available at the time to model Saturn's atmosphere, enabling scientists to approximately reconstruct Saturn's atmospheric density profile (1). This study extends the standard atmospheric torque calculation and data from Andrade *et al.* (1) and Sarani *et al.*'s (2) studies on the Cassini mission to calculate atmospheric torque in Uranus's atmosphere.

As demonstrated by Cassini, the torque applied on a spacecraft due to high atmospheric density at low altitudes is not unique to the Uranus Flagship and applies to other missions. Thus, this study produced the Preliminary Atmospheric Torque Calculation Tool (PATCaT), a tool that can be used to perform such calculations on future missions by changing parameters related to the spacecraft and target planet from mission to mission. The simplicity of PATCaT characterizes it as a suitable estimation tool for the early planning stages of a mission as it allows the user to make estimations when the system has unknown properties and fine-tune the calculation as mission parameters become clear throughout the planning process.

METHODS

Atmospheric Torque Equation

PATCaT calculates atmospheric torque using the standard equation presented by Andrade *et al.*, making simplifying assumptions about the spacecraft's motion and the user's needs (1).

It is assumed that a spacecraft whose mass distribution is not uniform orbits a planet and has constant orientation relative to the planet it is orbiting (so its orientation relative to the “forward” direction of motion changes). The spacecraft experiences the highest atmospheric density of its orbit at perigee, the moment in its orbit where it is nearest to the planet. Since it is assumed that the spacecraft's center of mass is not aligned with the center of its cross-sectional area when projected onto the plane orthogonal to its velocity vector, the spacecraft experiences torque applied by atmospheric particles. Since atmospheric density is maximized at perigee, so is torque.

PATCaT's atmospheric torque computation is based on the standard formula for computing the torque applied on any object: the cross product of the lever arm (the vector between the pivot point and the point where the force is applied) and the force itself. PATCaT takes this equation and incorporates environment-induced factors on the spacecraft system, such as atmospheric drag and atmospheric density. This relationship also takes into account the spacecraft's orientation and properties, such as its center of mass, center of torque, and velocity. PATCaT uses the following equation presented by Andrade *et al.* (1).

$$T_{Atm} = \frac{1}{2} C_D \rho V^2 A_{proj} u_V \times (r_{CT} - r_{CM}) \quad (1)$$

T_{Atm} = atmospheric torque, Nm

C_D = coefficient of drag, dimensionless

ρ = atmospheric density, kg/m³

V = velocity of the spacecraft relative to the surface of the planet, m/s

A_{proj} = the cross-sectional surface area of the spacecraft, m²

u_V = a unit vector whose direction is aligned with the velocity of the spacecraft

r_{CT} = center of torque; the position of the center of the spacecraft's cross-sectional surface area relative to a predetermined origin, m

r_{CM} = the position of the spacecraft's center of mass, m

u_V points in the same direction as the force applied onto the spacecraft by atmospheric pressure (to a factor of ± 1 depending on the orientation of the spacecraft's coordinate system) since it is a unit vector in the direction of the spacecraft's velocity vector. And since $(r_{CT} - r_{CM})$ is the vector obtained by subtracting the spacecraft's center of mass (which acts as a pivot) from the center of torque (which acts as the point where the force is applied), sometimes referred to as center of pressure, it represents the distance between them. Thus, before considering the scalars in the equation, it is clear that the directions of the vectors align with those of the general torque formula.

Now, consider each quantity and how it individually impacts T_{Atm} . The dimensionless coefficient of drag is computed based on the aerodynamics and texture of the front-facing part of the spacecraft (relative to its direction of motion). Andrade *et al.* uses orbiting data of Earth-orbiting satellites to estimate C_D to be 2.1 ± 0.1 (1).

Consider ρ and V together as ρV , or the product of atmospheric density and velocity. The magnitude of force applied on the

spacecraft by atmospheric particles is proportional to the amount of mass the spacecraft encounters per unit time. During a fixed amount of time, the number of particles a spacecraft encounters is determined by the distance it covers and the density of particles over that distance. Therefore, the product ρV represents the mass that the spacecraft encounters.

The projected surface area represents the surface area of the spacecraft that comes in contact with atmospheric particles because it is facing forward relative to the spacecraft's internal coordinate frame. Since the spacecraft has constant orientation towards Earth, its orientation relative to the center of its orbit (the planet) is changing. In this computation, since the intended user of PATCaT desires to confirm that the spacecraft's thrusters have enough power to overcome the highest torque the spacecraft may experience at perigee, it suffices to consider the maximum value of A_{proj} , which simply depends on the shape of the spacecraft and its possible orientations at perigee.

Now consider $V u_V$, which represents the spacecraft's velocity vector as the product of the scalar velocity and its unit (direction) vector. This factor is directly proportional to T_{Atm} because the faster the spacecraft moves, the faster the particles are moving when they collide with it, carrying more momentum and applying more force.

Development of PATCaT

PATCaT is a simple Python tool that is available publicly on GitHub (3). The following is an overview of the code comprising PATCaT's calculations:

When the PATCaT program is run, it begins by collecting user-defined parameters: atmospheric density profile, planet's angular velocity, spacecraft's dimensions, spacecraft velocity,

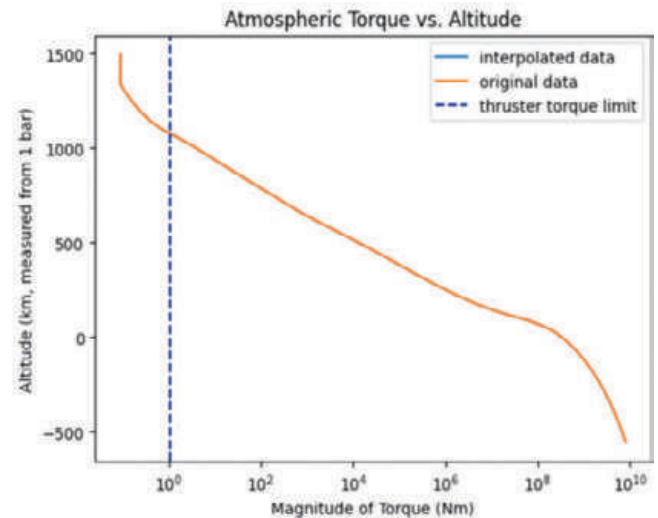


Figure 1: PATCaT plots the atmospheric torque expected at varying altitudes for a Cassini-like spacecraft in Saturn's atmosphere (solid line).

Magnitude of torque is plotted in Nm using a logarithmic scale along the x-axis because, given the large range of Saturn's atmospheric density profile, plotting using a linear scale would make the data appear compressed and difficult to read. In this figure, the dashed vertical line represents the maximum atmospheric torque that Cassini's thrusters can tolerate before the RCS fails (1 Nm). Thus, the intersection of the dashed and solid lines indicates the minimum altitude at which it is safe for a Cassini-like spacecraft to fly in Saturn's atmosphere (1077 km above the 1-bar level). Andrade *et al.* finds that loss of signal occurred at 1400 km above the 1-bar level (1). The difference between these values is discussed in the validation section.

spacecraft orientation, thruster force, thruster lever arm, wind speed, and drag coefficient. Using these parameters, the program computes the variables required to compute torque (Equation 1). Projected surface area is calculated by applying a three-axis rotation transformation to the spacecraft's dimensions to project its surface area onto the front-facing plane. The spacecraft's lever arm is computed similarly by applying three-axis rotation to the user-defined lever arm. Atmospheric density data is interpolated in order to generate additional data points spaced at smaller step sizes than those given, which is especially useful when working with a sparsely populated density profile. PATCaT implements cubic spline interpolation, which yields a polynomial that closely approximates atmospheric density at intermediate points based on the given atmospheric density profile. Finally, PATCaT uses these values to compute atmospheric torque (Equation 1).

RESULTS

The findings of this study indicate that, given the information currently available about the Uranus Flagship, there is a safe zone to fly in Uranus's atmosphere that avoids both collision with ring particles and intolerable atmospheric torque for the spacecraft.

According to PATCaT, a spacecraft of the approximate shape and size of Cassini can fly as low as 184 km above the 1-bar level (the altitude at which atmospheric pressure is 1 bar) in Uranus's atmosphere at a velocity of 14,868 m/s (Figure 3). The value 14,868 m/s is the estimated velocity after Uranus Orbit Insertion currently under consideration by Damon Landau, trajectory designer for the Uranus Flagship. Thus, the study concludes that at altitudes greater than 184 km above 1-bar, a spacecraft can safely handle the atmospheric torque it encounters.

The upper limit of the safe zone in Uranus's atmosphere is determined by the presence of ring particles. The 2017 Ice Giants Flagship Study, a paper that investigates the possibilities for exploration of the ice giant planets, finds that the hazard of

colliding with ring particles in Uranus's atmosphere disappears at approximately 2,500 km above the 1-bar level (5). Combining the lower and upper limits of safe altitudes yields the conclusion that the Uranus Flagship can fly within a range of over 2,000 km of atmosphere without risking ring particle collisions or loss of attitude control.

DISCUSSION

Model Assumptions

In this study, several assumptions have been made to simplify the calculation of atmospheric torque. While these assumptions reduce the rigor of PATCaT's calculations, they also reduce the burden to acquire exact parameters of the system and thus allow the user to experiment, given uncertain conditions in the early planning stages, ultimately making the tool useful during this phase.

One simplification is that the spacecraft is modeled as a rectangular prism. This allows the user to estimate torque without detailed information about the spacecraft's design. When the user inputs parameters describing the spacecraft's orientation, it is rotated as a rectangular prism.

Additionally, PATCaT assumes solid-body rotation of the planet and atmosphere. This is a notable assumption because the atmosphere of a planet does not rotate with the planet due to coupling between layers and friction, nor does it stand still relative to the planet's rotation. If desired, the user can specify either no rotation at all or an arbitrary wind speed. Introducing wind speed changes the effective velocity of the spacecraft, ultimately affecting the final result of the torque calculation because atmospheric torque is proportional to the square of velocity.

Also, PATCaT assumes that the dimensionless drag coefficient is 2.1. In practice, this number can be calculated more rigorously and depends on the aerodynamic design of the spacecraft and its speed.

Model Limitations Due to Spacecraft Design

Estimating the projected surface area of the spacecraft and its center of torque is a significant source of error in the calculation of atmospheric torque. According to Andrade *et al.*, it can account for up to 30% error (1). In the planning stages of a mission, the phase in which PATCaT may be implemented, this estimation accounts for significant error because PATCaT depends heavily on the design of the spacecraft, which is not known in the early planning stages.

When a spacecraft is in flight, although all properties of the spacecraft design are known well, unknown fuel usage makes it difficult to estimate the location of the spacecraft's center of mass relative to its center of torque and direction of motion. For example, in a monopropellant thruster system, where a spacecraft uses a single chemical for propulsion, fuel is stored in a pressurized tank and released periodically to propel the spacecraft. Thus, it grows difficult to determine how much fuel has been used at a given point in the mission, introducing errors in estimations of remaining fuel mass, which is necessary in order to locate the spacecraft's center of mass. In addition, the distribution of the fuel throughout the fuel tank, especially when fuel is low, is often unknown, providing another source of error in estimating the center of mass of the entire spacecraft.

Validation on Cassini: Saturn and Titan

PATCaT's calculations were validated on two existing atmospheric reconstructions from the Cassini mission on Saturn and Titan (1, 2). These two flights were selected to validate this study because PATCaT is intended for use on the Uranus Flagship mission, and

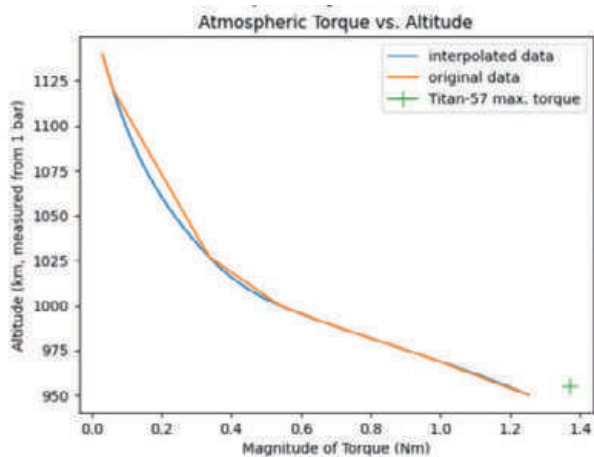


Figure 2: PATCaT plots the atmospheric torque expected at varying altitudes for a Cassini-like spacecraft in Titan's atmosphere (solid line).

In this figure, the point plotted with a cross at 1.37 Nm represents the maximum torque that Cassini experienced in Titan's atmosphere according to Sarani *et al.* (2). Sarani *et al.* finds that Cassini experienced this maximum torque at 955 km above the 1-bar level while PATCaT estimates the torque applied at 955 km to be 1.325 Nm. The difference between these values is discussed in the validation section.

the spacecraft used in the Uranus Flagship is expected to have similar dimensions, thruster capabilities, and reaction control system to the Cassini-Huygens spacecraft, according to trajectory designer Damon Landau. Atmospheric reconstruction data from Cassini's flights in Saturn and Titan's atmospheres were obtained directly for this study from Andrade *et al.* and Sarani *et al.*, respectively (1, 2). In order to smooth these atmospheric density profiles and provide data points at finer distance step sizes than the ones provided by the density profiles, PATCaT used a standard cubic spline interpolation, as detailed above, to generate more data points that were consistent with the existing data. The resulting interpolated data appears almost identical to the original data, due to the accuracy of the interpolation (Figure 1).

According to PATCaT, in the moments leading up to the "Final Plunge," Cassini should have tumbled out of control at 1077 km above the 1-bar level (Figure 1). Andrade *et al.* indicates that loss of signal occurred at 1400 km (1). The difference between these two values can be attributed to several sources of error.

The error between PATCaT's estimation of Cassini's altitude at loss of signal and the altitude computed by Andrade *et al.* could be attributed to the difference between the atmospheric density profile used by PATCaT and Andrade *et al.*'s reconstructed profile. PATCaT reads from Saturn's atmospheric density profile provided by the Langley Research Center because it covers a larger range of altitudes on Saturn, which differs from the data points in Andrade *et al.*'s reconstruction (1).

Another source of error is inaccuracy in the estimation of the force that the thrusters can provide. Cassini uses a blow-down monopropellant system, where fuel is expelled from the pressurized fuel tank when thruster force is desired (1). The force that the thrusters can provide depends directly on the pressure in the fuel tank, which is difficult to estimate because, as fuel is depleted, pressure in the tank naturally decreases and is replenished using helium or nitrogen. Error may also result from the estimation of projected surface area as discussed in the previous section and the velocity of the spacecraft being largely unknown.

Validation of PATCaT on Cassini's Titan-57 orbit also yielded results with less than 50% error (Figure 2). This error was calculated by comparing the torque calculated by Sarani *et al.* with the torque calculated by PATCaT (2). As with Saturn, the main sources of error were the atmospheric density profile utilized and the unknown velocity of the spacecraft.

Further Reduction of Sources of Error

While PATCaT's rough estimate offers sufficient accuracy for the early planning stages of a mission, in the future, sources of error can be reduced in several ways. In general, as more information about the spacecraft is revealed or determined throughout the planning process of a mission, using more accurate parameters such as exact dimensions, orbit insertion velocity, and orientation can improve the accuracy of PATCaT's results. In addition, obtaining a more accurate atmospheric density profile of the desired planet can increase the accuracy of the result. However, for certain planets, especially the planets that are furthest away from Earth such as Uranus, accurate atmospheric density profiles are not available due to a lack of research on those planets' atmospheres.

Another area in which accuracy can be improved is in PATCaT's modeling and calculations of the cross-sectional area of the spacecraft. PATCaT takes a simplistic approach by modeling the spacecraft as a rectangular prism. There also exists a rigorous approach to this problem, which involves projecting the exact design of the spacecraft onto the plane of motion, but this is unrealistic given the information available in

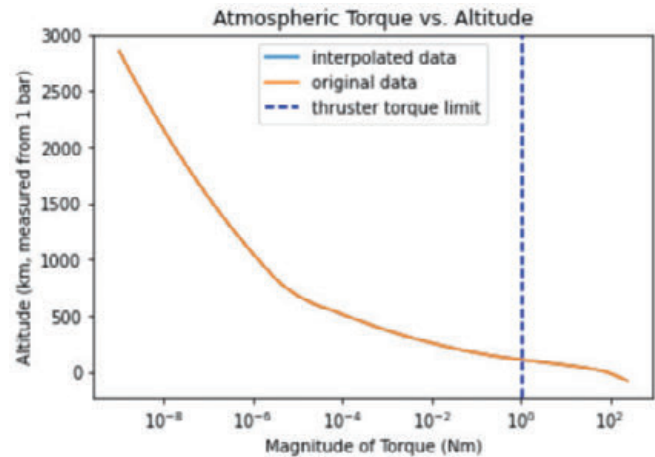


Figure 3: PATCaT plots the atmospheric torque expected at varying altitudes for a Cassini-like spacecraft in Uranus's atmosphere (solid line).

Magnitude of torque is plotted in Nm using a logarithmic scale along the x-axis because given the large range of Uranus's atmospheric density profile, plotting using a linear scale would make the data appear compressed and difficult to read. The dashed vertical line represents the maximum atmospheric torque that Cassini's thrusters can tolerate before the RCS fails (1 Nm). Thus, the intersection of the dashed and solid lines indicates the minimum altitude at which it is safe for a Cassini-like spacecraft to fly in Uranus's atmosphere (184 km above the 1-bar level).

a mission's early stage. However, future work could aim to take a new approach that balances rigor with simplicity by modeling the spacecraft as a collection of several rectangular prisms that approximate its shape.

CONCLUSION AND FUTURE DIRECTIONS

This study aims to answer the question: "How low can a spacecraft fly in Uranus's atmosphere?" PATCaT answers the question by offering insights into the safe zones of this gas giant's atmosphere to the 2023 Uranus Flagship team. Using the results from this tool, the trajectory design team can now constrict the mission's trajectory appropriately to avoid overwhelming the spacecraft's Reaction Control Subsystem and safely maintain attitude control throughout the tour of Uranus. Because of PATCaT's iterability and simplicity, the Mission Design and Navigation can fine-tune this constriction as more information about the capabilities of the Reaction Control Subsystem becomes available.

PATCaT has the potential to benefit any future mission that plans to fly a spacecraft into an atmosphere of significant density. Despite its limitations in accuracy, PATCaT provides insight into how much torque a spacecraft is expected to experience at various altitudes in a given planet's atmosphere, which may be utilized in the planning stages of a mission to more clearly understand the limitations of the mission and ensure that the spacecraft is capable of overcoming the torque it expects to experience. While the ability to rigorously perform these same calculations has already been developed, existing methods require knowing the exact design of the spacecraft and mission parameters, which is unrealistic during the early stages of planning a mission. PATCaT's simplicity makes it suitable for these stages because scientists often only seek an approximation of the mission's constrictions in

order to inform important decisions related to trajectory design and navigation.

ACKNOWLEDGEMENTS

Thank you to Mark Hofstadter, my mentor, for his great enthusiasm for planetary science and his patient guidance through the project. Thank you to Damon Landau for providing the expected velocity of the Uranus Flagship spacecraft at Uranus Orbit Insertion, Dylan Wilbur for providing assistance in using Jupyter, and Damon Landau and Reza Karimi for their insights on navigation and providing key information for developing the tool. This project was funded by Caltech's SURF program.

EDITORS

This article was reviewed by Isaac Ramos Reina, Joyce Goh, Nathan Joshua, and Sai Charan Petchetti; edited by Vivasvaan Aditya Raj, Lee Zucker-Murray, and Satviki Chaturvedi; and laid out by Christy Ma.

REFERENCES

1. L.G. Andrade, "Skimming through Saturn's Atmosphere: The Climax of the Cassini Grand Finale Mission." *AIAA Guidance Navigation, and Control Conference*, **AIAA 2018-2111**, 1-21 (2018). <https://doi.org/10.2514/6.2018-2111>
2. S. Sarani, "Titan Atmospheric Density Reconstruction Using Cassini Guidance, Navigation, and Control Data," *AIAA Guidance, Navigation, and Control Conference*, **AIAA 2009-5763**, 1-23 (2009). <https://doi.org/10.2514/6.2009-5763>
3. S. Naimi, PATCaT, Version 1, GitHub (2023). <https://github.com/shayanaimi/PATCaT>
4. T.A. Burke, "Cassini at Saturn Proximal Orbits – Attitude Control Challenges," *AIAA Guidance, Navigation, and Control Conference*, **AIAA 2013-4710**, 1-20 (2013). <https://doi.org/10.2514/6.2013-4710>
5. M. Hofstadter *et al.*, Uranus and Neptune missions: A study in advance of the next Planetary Science Decadal Survey. *Planet. Space Sci.* **177**, e104680 (2019). doi: 10.1016/j.pss.2019.06.004

Neural Lineage Reconstruction to Study Neural Networks in *Drosophila*

Jessica Goeij¹, Volker Hartenstein¹

¹Department of Molecular, Cell, and Developmental Biology, University of California, Los Angeles.

ABSTRACT

Neural lineages are defined as groupings of neurons formed by individual, genetically specified neuroblasts. Lineages are distinguishable at later developmental stages in *Drosophila melanogaster* via the progression of their axon tracts towards the neuropil, the network of fine processes (such as growth cones and filopodia) at the center of the embryonic brain. It is speculated that lineages interact with each other in a preferential and predictable manner, and vary in factors such as axon length and growth cone size. This study aims to distinguish between lineages at early developmental stages and gain a better understanding of lineage phenotype and interaction and thus neural circuit development as a whole. Transmission electron microscopy was used to image the *Drosophila* embryonic brain and generate 3D reconstructions of neural lineages in mid-late stage embryos. Lineages reconstructed include the antennal lobe (AL) lineage, the mushroom body (MB) lineage, as well as lineages that have yet to be traced in the posteromedial region of the brain. The AL and MB lineages were chosen for reconstruction because of their known interactions with each other in the larval brain, and the untraced lineages from the posteromedial region were chosen because of their potential for identification. These reconstructions confirmed that lineage phenotype varies most notably in axon length and growth cone size, neurons interact with each other in a preferential manner, and that neurons belonging to the AL and MB lineages do not interact with one another at the E14 stage. These findings provide insight into how the interaction of neurons of specific lineages during neuronal development shape the neural circuits of the differentiated brain.

INTRODUCTION

Drosophila melanogaster is a useful tool to model developmental questions in neuroscience (1-2), but the current lack of understanding in the formation of its neural lineages prevents its effective use as such. Neural stem cells, called neuroblasts, of the *Drosophila melanogaster* brain divide in a stem cell-like manner to form stereotyped sets of neurons called lineages (3). Neurons of a given lineage project their axons in a cohesive tract towards the neuropil, a network of neuronal processes (i.e., axons and dendrites) at the center of the embryonic brain. The pathway taken by each lineage-associated tract has a characteristic entry point and trajectory. Based on the trajectory of their axon tract, lineages can be identified and followed from larval to adult stages (4).

Axon tracts of *Drosophila melanogaster* begin to emerge in the mid-late stage embryonic brain (4) (Figure 1). Ongoing research reveals that tracts in the embryonic brain can be identified with corresponding tracts in the larva (5-6), allowing for this study's identification of different lineages from embryonic stage 12 (E12) onward and analysis of the characteristics of lineages in the developing brain (4). Such characterization has not yet been achieved for *Drosophila*. Previous studies, primarily *in vitro*, for some neuron populations in the *Drosophila* optic lobe have shown that growth cones at the tips of advancing axons form filopodia whose dynamic activity is correlated with different stages of

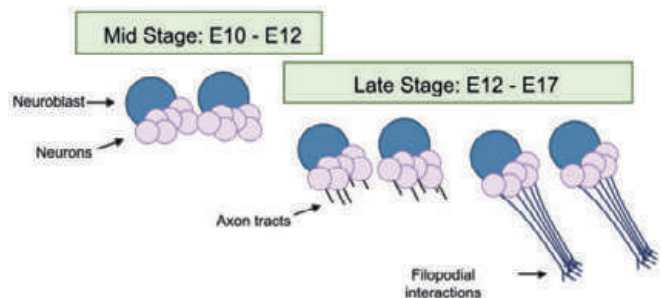


Figure 1: Schematic representation of axon growth across different stages of neural development.

Neural stem cells (called neuroblasts) divide in a pattern-like manner to form neurons, which occur in the early-mid stages (E10-E12) of embryonic development. As such, axon tracts at this stage do not yet exist. Neurons begin to project axon tracts and eventually form bundles during the later stages (E12-E17) of embryonic development.

axonogenesis and synapse formation (7), which demonstrates the potential for growth cone and filopodial phenotype/behavior as valuable markers for understanding neuronal development. The study's analysis will address the following questions:

Filopodia and Connectivity

Neurons have stereotyped synaptic connections and appear to preferentially connect with specific neurons while avoiding forming connections with others (7). Connections of the *Drosophila* larval brain (“connectome”) have recently been fully described using a serial electron microscopy (EM) stack of an early first larval instar (L1) brain (8). The connectome provides an “end point” of connectivity, or the final product of embryonic brain development. However, it is uncertain how these connections arise and at what stage they become visible (8). This study hypothesized that connections between neurons are established at an early stage (before the larval stage) through direct contact with filopodia, when neurons are physically very close to each other (8). These filopodial connections dictate patterns of branching and synaptic connections. As more neurons form and branch, neuropil volume increases and neurons are pushed away from one another while maintaining connections (9), which subsequently lengthens the connection between originally nearby neurons (Figure 1) (4). This study aimed to evaluate this hypothesis by examining two specific sets of neurons that are known to form connections with each other in the larval brain: the mushroom body (MB) and antennal lobe (AL) neurons (10).

Relationship Between Growth Cones and Lineages: Comparing Lineages

Growth cones, which exist at the tip of the axon tract and are where filopodia are located, dictate the direction in and depth at which an axon progresses (11). It is hypothesized that neurons of different lineages have varying structural properties, such as variations in growth cone size (Figure 2A). This study aimed to determine the extent to which growth cones differ in size/shape depending on their lineage.

Relationship Between Filopodial Properties and Lineages: Within Lineages

Based on the proliferation pattern of neuroblasts, neurons are born at different time points over a span of approximately 5 hours (4). Currently, two hypotheses exist regarding axon development (Figure 2B). The first hypothesis is that axons of a lineage develop simultaneously, causing all neurons at a specific developmental stage to have axon tracts of similar lengths (12). The second hypothesis is that axon development is staggered, so that neurons at a specific developmental stage have axon tracts that vary in length. In this hypothesis, longer axon tracts would belong to neurons that are more mature (i.e., arise earlier) while shorter axon tracts would belong to neurons that are less mature (arise later) (13, 14).

The study produced a 3D model of neurons at stage E14, which was chosen because it is a mid-late stage of development where axon tracts begin to arise. Doing so accomplishes three main goals. First, it would be possible to identify lineages at the earliest possible stage, allowing for the establishment of links between corresponding neuroblasts and a more accurate characterization of lineage phenotypes at prior stages. Second, it would be possible to determine the way in which synaptic connections are formed. Seeing interaction between neurons in the mid stage embryonic brain would provide evidence for the idea that synaptic connections are pre-established, while seeing a lack of interaction between neurons in the mid-stage embryonic brain would provide evidence for the idea that synaptic connections are formed. Lastly,

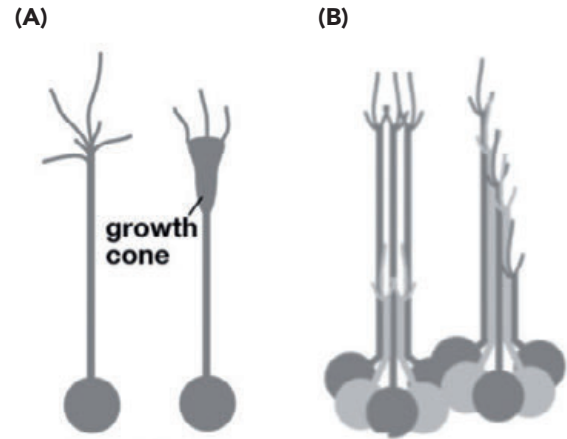


Figure 2: Schematic representation of hypotheses regarding growth cone size/shape and axon projection.

(A) Different hypotheses regarding growth cone size/shape. The first hypothesis is that growth cones are relatively smaller/seemingly non-existent, as showcased by the neuron on the left. The second hypothesis is that growth cones are larger with a distinctive shape, as showcased by the neuron on the right. **(B)** Different hypotheses regarding axon development. The left lineage represents the hypothesis that axon tracts arise simultaneously, and the right lineage represents the hypothesis that axon tracts arise in a staggered manner.

with the reconstruction of more neurons in the future, a better understanding of the structure of neuronal lineages in terms of their axon lengths, growth cone size, and filopodia patterning will be achieved.

MATERIALS AND METHODS

Imaging

Drosophila melanogaster E14 embryonic brains were first embedded externally following standard protocol (15). In the first osmication step, the samples were treated with 2% osmium tetroxide and 1.5% potassium hexacyanoferrate in darkness at room temperature for 30 minutes. The samples were then treated with 1% thiocarbohydrazide (TCH) in water at 60°C for 10 minutes in an enhancement step. Lastly, the samples were treated with 2% osmium tetroxide and 1.5% potassium hexacyanoferrate in darkness at room temperature for 30 minutes again in a second osmication step.

Following the second osmication step, the samples were rinsed with water and dehydrated using ethanol. The samples were consecutively treated with a 1:2 ratio of resin and ethanol, a 2:1 ratio of resin and ethanol, and overnight using pure resin. The samples were then placed between a Teflon-coated slide and an Aclar coverslip with 200-mm spacers and polymerized at 60°C, trimmed and cut into 70 nm sections, mounted onto 3View sample pins, and trimmed at the ultra-microtome utilizing a glass knife at right angles. An electromagnetic (EM) beam was then used to image the samples.

Lineage Classification

Neurons were identified and categorized into the MB and AL lineages by matching the position of the MB and AL lineages in the brain from the literature with the observed position of neurons

from our sample. This project focused on the left hemisphere of the brain, divided into the following regions: anterior posterior, anterior medial, central lateral, central medial, posterior lateral, and posterior medial. Neurons located in the posterior medial region of the brain were also categorized into classes A-D based on their axon lengths, axon bundling, and interactions with the neuropil.

Generating 3D Models

Two types of 3D models were generated: the approximate 3D models, and the detailed 3D models. In order to create the approximate 3D models, the locations of cell bodies were identified within the EM stack on Fiji ImageJ. Markers were placed at the location of the cell body and axon tract at each slice, becoming the cell body and axon tract in the approximate 3D model. The approximate 3D models display the general location of the cell body and direction of the axon tract. Phenotypic characteristics (parallel growth, axon length, growth cone size/shape, filopodia locations and interactions) were evaluated both qualitatively and quantitatively. Quantitative analysis of the distance between the neuropil and cell bodies were done on Fiji ImageJ using a coordinate system, Euclidean distance, and standard measurements. Growth cone length was analyzed using the 3D renderings of neurons and standard measuring tools in Fiji ImageJ. Qualitative analysis was done by examining the relative parallel growth of axons and axon lengths. Neurons were then color-coded based on axon length.

In order to create the detailed 3D models, markers and dots were followed to show the location of the cell body and axons, respectively. With these markers and dots as guidance, the shape of the neuron on each image was outlined, and subsequently combined using Fiji ImageJ to generate the 3D structures. Neurons were then color-coded based on axon length.

Distance Measurements and Ratio Calculations

The approximate 3D coordinates were determined for the center of the neuropil and the center of each neuronal cell body (CB) by measuring the width and height of each object within Fiji ImageJ and geometrically determining the center. The distance between the neuropil and cell body for a sample of neurons located in the posterior medial region of the embryonic brain were determined using Euclidean distance. All coordinates and distances are measured in micrometers (μm). Statistical analysis was done using (1) a Wilcoxon rank sum test and corrected using a Benjamini-Hochberg correction for the neuronal depth calculations and (2) a C1-way ANOVA for the growth cone width calculations. Scripts for figure generation and statistical testing were run in RStudio.

RESULTS

No Interaction Was Seen Between AL and MB Neurons, and Mostly Distal Filopodia Were Found

To aid in interpretation, a single neuron is provided (Figure 3). Although AL and MB lineage neurons are known to form connections in the larval brain, at this stage there were no interactions between neurons belonging to the AL lineage and neurons belonging to the MB lineage, meaning that they have no direct contact (Figure 3). Additionally, it was observed that the majority of neurons (90%) belonging to the AL and MB lineages had more distal filopodia than interstitial filopodia (Figure 4, Table 1 and 2).

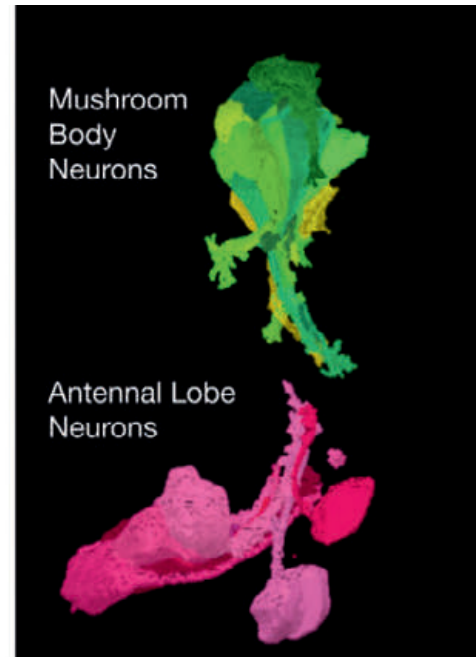


Figure 3: Detailed reconstruction of neurons belonging to MB and AL lineages.

Representation of neurons belonging to the MB and AL lineages. The neurons in green shades belong to the MB lineage, and the neurons in pink shades belong to the AL lineage. At this stage of development, neurons belonging to the MB and AL lineages do not come into physical contact or form connections with each other.

Variations in Axon Lengths Were Found, with No Correlation to Neuronal Positioning

The approximate reconstruction of the neuropil and neurons belonging to lineages revealed variations in neuronal axon length and interactions with the neuropil that segregated the neurons into four classes (Figure 5A). To aid in this interpretation, a single neuron was provided (Figure 5B). Class A neurons had very short axon tracts and did not form bundles. This class of neurons is not long enough to reach the neuropil. Class B neurons had short axon tracts but were long enough to form bundles. This class of neurons was also not long enough to reach the neuropil. Class C neurons had long axon tracts of sufficient length to form bundles. This class of neurons was long enough to reach the neuropil; however, their axon tracts ended right as they reached the neuropil. Class D neurons had long axon tracts that were both of sufficient length to form bundles, and to reach to and extend through the neuropil. In the study's current sample of neurons ($n=26$), there appears to be no statistically significant ($p>0.05$) relationship between the class that a neuron belongs to, and the distance between the cell body and the neuropil, and thus the position in the brain (Figure 6).

Variations Exist in Growth Cone Size and Shape, and Preferential Interactions Were Seen

Variations were seen in growth cone shape and size. The lineages classified into class C of neurons had significantly wider growth cones ($p=0.00617$) by approximately 260% compared to the lineages classified into class D of neurons (Figure 7A). Lastly,

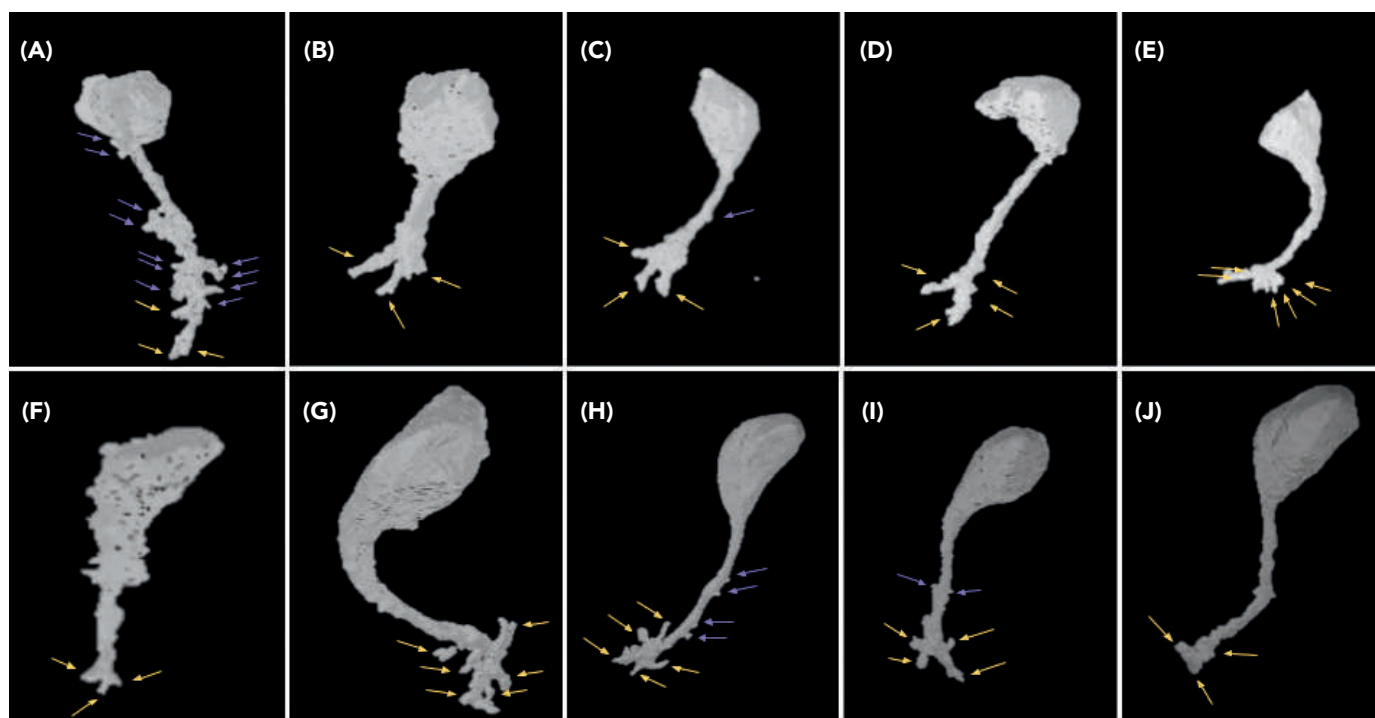


Figure 4: Individual detailed reconstruction of AL and MB lineage neurons

Interstitial filopodia are shown by purple arrows, and distal filopodia are shown by yellow arrows. Neurons with varying physical characteristics, including axon width/length and cell body shape, were chosen to be represented. The sample of neurons chosen is representative of the total sample of reconstructed neurons. **(A)** 3D reconstruction of the 7 la 12c neuron, belonging to the AL lineage, which has more interstitial filopodia than distal filopodia. It also has a large number of filopodia as a whole. **(B)** 3D reconstruction of the 11 bamv3a neuron, belonging to the AL lineage, which has more distal filopodia and no interstitial filopodia. **(C)** 3D reconstruction of the 2 bamv3a neuron, belonging to the AL lineage, which has more distal filopodia than interstitial filopodia. **(D)** 3D reconstruction of the 1 bamv3 neuron, belonging to the AL lineage, which has more distal filopodia and no interstitial filopodia. **(E)** 3D reconstruction of the 3 lc a neuron, belonging to the AL lineage, which has more distal filopodia than interstitial filopodia. **(F)** 3D reconstruction of the MBc 2 R 9 PM23n neuron, belonging to the MB lineage, which has more distal filopodia than interstitial filopodia. **(G)** 3D reconstruction of the MBc 9 9PM20n neuron, belonging to the MB lineage, which has more distal filopodia than interstitial filopodia. **(H)** 3D reconstruction of the MBc 6 8PM32n neuron, belonging to the MB lineage, which has more distal filopodia than interstitial filopodia. **(I)** 3D reconstruction of the Dpmp1 b 3 8PM22n neuron, belonging to the MB lineage, which has more distal filopodia than interstitial filopodia. **(J)** 3D reconstruction of the Dpmp1 b 4 r 8pm20n neuron, belonging to the MB lineage, which has more distal filopodia than interstitial filopodia. Most aforementioned neurons. **(B-J)** have more distal filopodia than interstitial filopodia.

Name of Neuron	Distal	Interstitial
7 la12 c	3	12
11 bamv3a	3	0
2 bamv3a	4	1
1 bamv3	2	0
3 lc a	6	0

Table 1:

A count of distal and interstitial filopodia from a sample of neurons belonging to the AL lineage in Figure 3.

Name of Neuron	Distal	Interstitial
MBc 2 R 9 PM23n	3	0
MBc 9 9PM20n	6	0
MBc 6 8PM32n	5	4
Dpmp1 b 3 8PM22n	4	2
Dpmp1 b 4 r 8pm20n	2	0

Table 2:

A count of distal and interstitial filopodia from a sample of neurons belonging to the MB lineage in Figure 4.

interactions were seen between certain neurons and bundling of certain neurons, which is defined as the selective groupings of some neurons and the selective avoidance of other neurons. Specifically, neurons belonging to class C and D clearly appeared to belong to a lineage based on how their axons grew in close proximity and in parallel to one another (Figure 7A). To aid in this interpretation, a single neuron was provided (Figure 7B).

DISCUSSION

Prior studies have primarily focused on the adult *Drosophila* brain (1, 2, 16), and thus there is a need for models that focus on the embryonic *Drosophila* brain to answer development-specific research questions. By identifying patterns in the phenotypic characteristics (axon length, growth cone size, and filopodia

interactions with other neurons) of neurons in the brain of the mid-late stage *Drosophila* embryo, this project allowed for a clearer characterization of neural lineages at successive previous stages and identification of phenotypic markers for the recognition of specific lineages throughout different developmental stages.

It was concluded that there are four different classes of neurons that differ in their length and interactions with the neuropil: class A having no axon tracts, class B having short axon tracts and bundling present, class C having long axon tracts that form bundles but barely reach the neuropil, and class D having long axon tracts that form bundles and run through the neuropil. Among specific classes of neurons, the close interactions and parallel axon growth at stage E14 are clear evidence of bundling and lineage formation. Variation in axon tract lengths provides evidence that axons start development at different times (13, 14). At this stage, there does not appear to be any relationship between the class a neuron belongs to and its distance from the neuropil and depth into the brain. Furthermore, it was concluded that there are variations in growth cone size/shape based on neuron class, and that the majority of mushroom body and antennal lobe filopodia are distal, rather than interstitial. These findings may contribute to the understanding of the mechanisms of neural circuit (network of synaptic connections) formation, as this will provide information

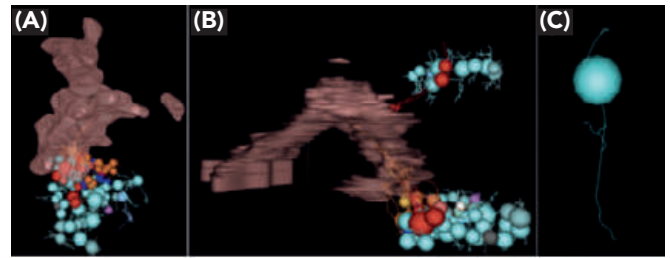


Figure 5: Approximate reconstruction of the neuropil and neural lineages.

(A) Representation of the neuropil, which is the pink structure, and neurons surrounding the neuropil. Neurons are color-coded according to the class they belong to. Cyan neurons belong to the first class, dark blue neurons belong to the second class, red neurons belong to the third class, and orange neurons belong to the fourth class. At this angle, the dorsal side faces outwards. (B) Representation of the neuropil, which is the pink structure, and neurons surrounding the neuropil. Neurons are color-coded according to the class they belong to. Cyan neurons belong to the first class, dark blue neurons belong to the second class, red neurons belong to the third class, and orange neurons belong to the fourth class. At this angle, the dorsal side faces upwards. (C) Representation of a single neuron. The sphere is representative of the cell body, and the line is representative of the axon tract.

The Distance Between the Neuropil and Cell Body Across Different Neuronal Classes

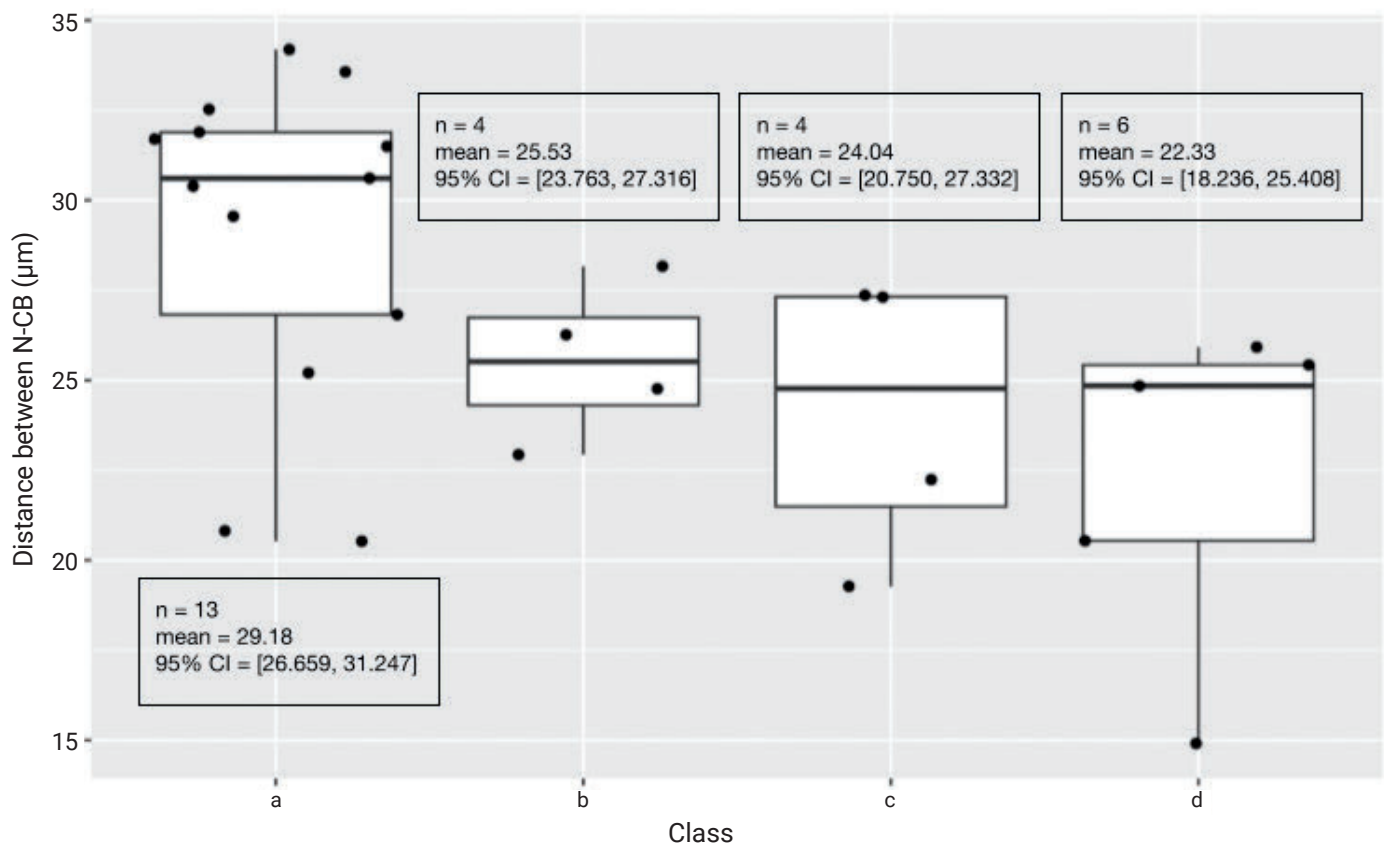


Figure 6: Relative positioning of neurons within the brain.

Boxplot of the distances between the cell body of neurons ($n=26$) and the neuropil (CB-N), measured in micrometers, for each class. Analysis was done using a Wilcoxon rank-sum test and a Benjamini-Hochberg correction ($p>0.05$ for classes A-D), and a 95% confidence interval (CI) is given.

on how axons are guided and neurons ultimately interact with one another. Additionally, the lack of physical interactions found between the antennal lobe and mushroom body neurons at E14 suggests that these connections will form at a later stage.

The current study lacks a large sample size for neurons in each specific class, given time constraints. In addition, the study is limited in the approximations made in determining the center of the neuropil, which is irregularly-shaped. More neurons should be analyzed in order to reach a more concrete conclusion. Therefore, the future of this project will focus on 3D rendering neurons at earlier stages (stage E13 and prior). Lineage identification has been more successful in the later embryonic stages (17) and in the larval brain (18-20). As such, much is known about the phenotypic characteristics and interactions between lineages at the later embryo and larval stages of development (13, 14, 16, 17). However, given that axon tracts have yet to form at the early-mid embryonic brain, less is known about lineages at these early stages. With this knowledge about the later embryo and larval stages, phenotypic characteristics found during this project will be used to draw connections between later and earlier embryonic stages. Overall, this project provided valuable insight on the phenotypic characteristics of neural lineages in the mid-late stage *Drosophila* embryo brain, which will aid in the overall understanding of the formation of neural circuits and the tracing of neural lineages at earlier developmental stages.

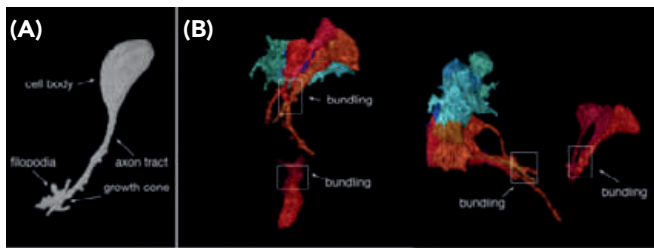


Figure 7: Approximate reconstruction of the neuropil and neural lineages.

(A) Representation of neurons that are color-coded according to the class they belong to. Cyan neurons belong to class A, dark blue neurons belong to class B, red neurons belong to class C, and orange neurons belong to class D. Neurons belonging to class C were found to have significantly wider growth cones ($p=0.00617$) in comparison to neurons belonging to class D. (B) Representation of a single neuron. The spherical structure at the top is representative of the cell body, the descending rod is representative of the axon tract, and the structure at the bottom is representative of the growth cone and filopodia.

ACKNOWLEDGMENTS

I would like to thank my faculty mentor, Volker Hartenstein, for his support and mentorship throughout this project. Additionally, I would like to acknowledge Aydin Karatas for his help in this project in creating the boxplots and running statistical analysis. I would also like to thank the rest of the Hartenstein Lab for all of the work that they do.

EDITORS

This article was reviewed by Daniel Bielin, Marissa Li, Miki Matsuoka, and Zoe Yeh, edited by Paul Zhang and Zachary Lamm, and laid out by Zenya Bian.

REFERENCES

1. Y. Lee *et al.* Conservation and divergence of related neuronal lineages in the *Drosophila* central brain. *eLife*, **9**, e53518 (2020).
2. S. Y. Takemura *et al.* A connectome of a learning and memory center in the adult *Drosophila* brain. *eLife*, **6**, e26975. (2017). doi: 10.7554/eLife.26975.
3. P. Kandimalla *et al.* Lineages to circuits: the developmental and evolutionary architecture of information channels into the central complex. *J Comp Physiol A* **209**, 679–720 (2023). doi: 10.1007/s00359-023-01616-y
4. S.R. Spindler, V. Hartenstein. The *Drosophila* neural lineages: a model system to study brain development and circuitry. *Dev Genes Evol* **220**, 1–10. (2010). doi: 10.1007/s00427-010-0323-7.
5. Y.J. Lee *et al.*, Conservation and divergence of related neuronal lineages in the *Drosophila* central brain. *eLife*, **9**, e53518. (2020). doi: 10.7554/eLife.53518
6. G.S. Marques *et al.*, Fate transitions in *Drosophila* neural lineages: a single cell road map to mature neurons. *bioRxiv*. (2021).
7. R. Grosskortenhaus, *et al.*, Regulation of temporal identity transitions in *Drosophila* neuroblasts. *Dev Cell*, **8**(2), 193–202. (2005) doi: 10.1016/j.devcel.2004.11.019.
8. K. Ito, & M. Ito. Whole-brain neural network analysis (connectomics) using cell lineage-based neuron-labeling method. *Microscopy* **63** Suppl 1, i8 (2014). doi: 10.1093/jmicro/dfu088.
9. M. Winding *et al.* The connectome of an insect brain. *Science* **379**(6636), eadd9330 (2023). doi: 10.1126/science.add9330.
10. K.M. Kollins & R.W. Davenport. Branching Morphogenesis in Vertebrate Neurons. *Madame Curie Bioscience Database* (2007). doi: 10.1016/bs.mcb.2014.12.012.
11. T. Saumweber *et al.* Functional architecture of reward learning in mushroom body extrinsic neurons of larval *Drosophila*. *Nat Commun* **9**, 1104 (2018). doi: 10.1038/s41467-018-03130-1.
12. P.R. Gordon-Weeks. Microtubules and growth cone function. *J. Neurobiol.* **58**, 70–83 (2004). doi: 10.1002/neu.10266.
13. W.A. Tyler *et al.* Neural precursor lineages specify distinct neocortical pyramidal neuron types. *J Neurosci* **35**(15), 6142–6152 (2015). doi: 10.1523/JNEUROSCI.0335-15.2015.
14. T. Erclik *et al.* Integration of temporal and spatial patterning generates neural diversity. *Nature* **541**(7637), 365–370 (2017). doi: 10.1038/nature20794.
15. J.T. Paridaen *et al.* Analysis of primary cilia in the developing mouse brain. *Methods in cell biology* **127**, 93–129 (2015). doi: 10.1016/bs.mcb.2014.12.012.
16. L.K. Scheffer *et al.* A connectome and analysis of the adult *Drosophila* central brain. *eLife* **9**, e57443 (2020). doi: 10.7554/eLife.57443.
17. B. Zhou *et al.* Temporal patterns of broad isoform expression during the development of neuronal lineages in *Drosophila*. *Neural Dev* **4**, 39 (2009). doi: 10.1186/1749-8104-4-39.
18. V. Hartenstein *et al.* Lineage-associated tracts defining the anatomy of the *Drosophila* first instar larval brain. *Dev Biol* **406**(1), 14–39 (2015). doi: 10.1016/j.ydbio.2015.06.021.
19. W. Pereanu & V. Hartenstein. Neural Lineages of the *Drosophila* Brain: A Three-Dimensional Digital Atlas of the Pattern of Lineage Location and Projection at the Late Larval Stage. *J Neurosci* **26** (20), 5534–5553 (2006). doi: 10.1523/JNEUROSCI.4708-05.2006.
20. N.S. Michki *et al.* The molecular landscape of neural differentiation in the developing *Drosophila* brain revealed by targeted scRNA-seq and multi-informatic analysis. *Cell Rep* **35**(4) (2021). doi: 10.1016/j.celrep.2021.109039.

Dopamine Signaling Mediates Skin Penetration by *Strongyloides stercoralis*

Aracely Garcia Romero¹, Ruhi Patel², Elissa A. Hallem²

¹Department of Molecular, Cell, and Developmental Biology, University of California, Los Angeles. ²Department of Microbiology, Immunology, and Molecular Genetics, University of California, Los Angeles.

ABSTRACT

Strongyloides stercoralis is a skin-penetrating gastrointestinal parasitic nematode that is prevalent worldwide and primarily infects humans living in under-resourced and neglected tropical and subtropical regions of the world. Skin penetration is critical to parasitism; however, the mechanisms underlying the process are poorly understood and uncharacterized as there are no prior research studies available. This paper investigates the role of dopamine signaling during skin penetration in *Strongyloides stercoralis*. The effect of silencing the dopaminergic neurons on skin penetration behavior was examined using *ex vivo* skin penetration assays. To silence the dopaminergic neurons, a construct was generated in which a promoter specific for the dopaminergic neurons was used to drive expression of the histamine-gated chloride channel HisCl1. Exposing nematodes expressing this construct to exogenous histamine results in silencing of the dopaminergic neurons. Silencing the dopaminergic neurons severely impaired skin-penetration behavior: the proportion of time spent attempting penetration was reduced by approximately 4-fold and the time to initiation of penetration was significantly delayed by approximately 3-fold. Additionally, silencing the dopaminergic neurons inhibited skin penetration in 20% of the larvae. The results suggest that dopamine signaling plays an essential role in skin-penetration behavior and provides a deeper understanding of the mechanisms by which skin-penetrating nematodes invade human hosts.

INTRODUCTION

Strongyloides stercoralis is a skin-penetrating gastrointestinal parasitic nematode that infects nearly two billion people worldwide, with infections primarily affecting those in under-resourced tropical and subtropical areas (1, 2). *S. stercoralis* infection can lead to strongyloidiasis, a neglected tropical disease affecting over 600 million people across the world that can cause abdominal pain, diarrhea, hives, and death in immunocompromised individuals (2). Skin-penetrating nematodes also cause extensive morbidity in livestock and pets (3). *S. stercoralis* infects host organisms during the developmentally arrested infective third-larval stage (iL3). At this developmental stage of *S. stercoralis*, iL3s penetrate through the skin of the host to establish an infection (3). Although skin penetration is essential to parasitism, the exact behaviors that iL3s engage in while penetrating skin are not well understood, likely because assays to closely examine these behaviors did not previously exist and no current research has expanded on this further. Furthermore, the neural mechanisms that underlie skin-penetration behaviors have not been investigated. It is unclear whether the sensory neurons of *S. stercoralis* drive skin penetration in response to specific mechanical properties of the skin surface.

Caenorhabditis elegans, a well-studied and free-living nematode, is morphologically and genetically similar to *S. stercoralis*; thus, studies in *C. elegans* provide a good starting point for investigating the role of homologous genes and neurons in

parasite-specific behaviors in *S. stercoralis* (4). Some behaviors, such as texture-sensing in the environment, and their underlying neural mechanisms have been studied in *C. elegans*. When *C. elegans* encounter a bacterial lawn, their speed of locomotion slows, and mechanosensory texture-sensing neurons drive this slowing response (5). Dopamine signaling in *C. elegans* is necessary for sensation of the texture of the surrounding environment. Dopamine is also required for *C. elegans* to discern and discriminate between features of the tangible environment, a behavior known as spatial pattern selectivity (6). *C. elegans* uses this behavior to select a preferred surface, one with the highest texture density, as elucidated by previous research where *C. elegans* were exposed to different textured chambers. Underlying these behaviors are the mechanosensory dopaminergic neurons, which integrate spatial information and behaviors (6). Thus, dopamine appears to be important for the ability of *C. elegans* to sense and respond to the surrounding environment.

As further evidence that dopamine is a critical and conserved regulator of the nervous system across different animals, critical components of the dopamine biosynthesis pathway have homologs in different species (5). In *C. elegans*, the gene *cat-2* encodes a tyrosine hydroxylase that is a critical component of the pathway for dopamine biosynthesis (7) (Figure 1). Additionally, the *C. elegans* gene *dat-1* encodes a transporter that recycles dopamine from the synaptic cleft (8). The *S. stercoralis* homologs of the *C. elegans* *cat-2* and *dat-1* genes were identified. Thus, key components of the pathways that synthesize dopamine and

regulate the bioavailability of the neurotransmitter are conserved in *Strongyloides* species.

Of the mechanosensory neurons of *C. elegans*, the dopaminergic neurons cephalic sensillum (CEP), anterior deirid sensillum (ADE), and posterior deirid sensillum (PDE) have been extensively studied for their critical role in modulating the detection of mechanical stimuli (9). Specifically, these neurons are implicated in the sensation of harsh touch and texture (10). These neurons sense the mechanical properties of bacterial food and can be triggered via touches to the nose and with specific excitation by a bacterial food source. Further research on the dopaminergic neurons in *C. elegans* and *S. stercoralis*, is required to expand this understanding in different biological contexts such as in the human-infective hookworm, *Ancylostoma duodenale*.

This study tests whether the dopaminergic neurons of *S. stercoralis* modulate skin-penetration behavior. It is hypothesized that the *S. stercoralis* dopaminergic neurons modulate skin-penetration behavior in response to the sensation of skin surface texture. To test whether dopaminergic neurons regulate skin-penetration behavior, the dopaminergic neurons are chemogenetically silenced using the histamine-gated chloride channel *HisCl1* (11). In nematodes that express these constructs specifically in the dopaminergic neurons, exposure to exogenous histamine silences the dopaminergic neurons (Figure 2). In support of this hypothesis, it was found that silencing the dopaminergic neurons impaired the ability of *S. stercoralis* iL3s to penetrate the skin. These results enhance the understanding of the mechanisms that drive skin penetration by *S. stercoralis* and other skin-penetrating nematodes and may inform the development of therapies that prevent infection.

METHODS

Maintenance of *S. Stercoralis*

S. stercoralis was cultured by serial passage through *Meriones unguiculatus* (Mongolian gerbils) using protocols approved by the UCLA Office of Animal Research Oversight (Protocol ARC-2011-060), which adheres to the standards of the Association for Assessment and Accreditation of Laboratory Animal Care (AAALAC) and the Guide for the Care and Use of Laboratory Animals. The strain of *S. stercoralis* that was used for these studies was a generous gift from Dr. James Lok at the University of Pennsylvania School of Veterinary Medicine. An infective dose of 2000 iL3s was used for each gerbil, with a total sample size of 8. Feces were collected from infected gerbils from days 14-44 post-inoculation by placing animals on wire racks, over a damp techboard, overnight. The collected feces were mixed with approximately 3 times the amount of autoclaved charcoal and plated on damp Whatman filter paper in 10 cm Petri dishes. Fecal-charcoal plates were placed at 20°C for the first 2 days and then at 23°C for a maximum of 7 days until used for collection of iL3s. *S. stercoralis* iL3s used in these studies were collected from 7-day-old plates.

DNA Constructs for Silencing the *S. Stercoralis* Dopaminergic Neurons

To silence the dopaminergic neurons, constructs were generated in which a promoter specific for the dopaminergic neurons is used to drive expression of the histamine-gated chloride channel *HisCl1* (11,12). The plasmid pAGR02 was first generated using the bioinformatics software, Geneious Prime. pAGR02 comprises the following elements: the *Ss-dat-1* promoter, which corresponds

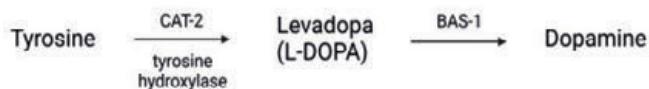


Figure 1: Schematic of the dopamine biosynthetic pathway.

The *cat-2* gene encodes a tyrosine hydroxylase required for dopamine biosynthesis. Levodopa (L-DOPA) is required to catalyze this sequential reaction, with *bas-1* being a critical aromatic amino acid decarboxylase that mediates the conversion of L-DOPA to dopamine. Figure was adapted from Chase and Koelle, 2007 (7). Figure made with Biorender.

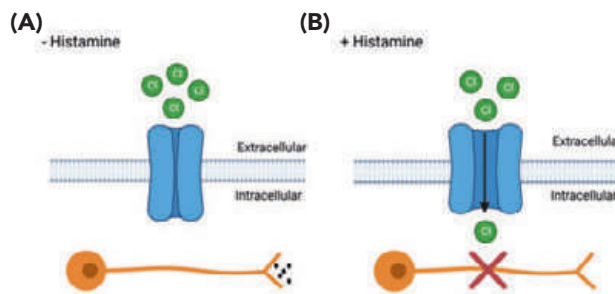


Figure 2: Schematic of the histamine-gated chloride channel HisCl1

(A) HisCl1 is not activated in the absence of histamine (top), and therefore neuronal activity is not inhibited (bottom). (B) HisCl1 is activated by the addition of exogenous histamine (top), leading to an influx of chloride ions and inhibition of neuronal activity (bottom). Transgenic iL3s were treated with 1 mL of either 50 mM histamine solution or the corresponding vehicle-only control (double-distilled water mixed with buffered saline). iL3s are soaked in exogenous histamine solution for 3-4 hours prior to assays. Figure made with Biorender.

to nucleotides 145032-147610 of SSTP_contig0000014; the coding sequence for the histamine-gated chloride channel HisCl1 (12); the self-cleaving peptide P2A; and the coding sequence for the fluorophore mScarlet. This fluorophore was selected as previously established constructs in the lab have utilized mScarlet. Given that mScarlet is a fluorophore, expression of mScarlet was used to identify and separate transgenic nematodes from non-transgenics under a fluorescent microscope since it marks which nematodes express the construct. P2A induces ribosome skipping, which is necessary to produce two separate proteins (HisCl1 and mScarlet) from the initial bicistronic transcript. P2A allows for the expression of multiple proteins with a single promoter. In the absence of P2A, the HisCl1 protein might not be able to silence neurons effectively because of misfolding due to fusion with the mScarlet protein. All coding sequences were previously codon-optimized to maximize expression in *S. stercoralis*. The *Ss-dat-1* promoter was amplified from *S. stercoralis* genomic DNA using the primers RP15 and RP16 and cloned upstream of the *Str-HisCl1::P2A::Str-mScarlet* cassette in pRP09 using the restriction enzymes HindIII (New England Biolabs #R0104) and AgeI (New England Biolabs, #R3552). The sequences of the primers RP15 (5' TCAAGCTTTTATATATATTTTATTTTATTTCAATTAATATA 3') and RP16 (5' ATACCGGTTTGATTTTAAATCTTTTATTAATGATTC 3') were synthesized by Integrated DNA Technologies.

The construct pAGR02 was microinjected into 146 *S. stercoralis* free-living females at a concentration of 80 ng/ μ L over 6 non-

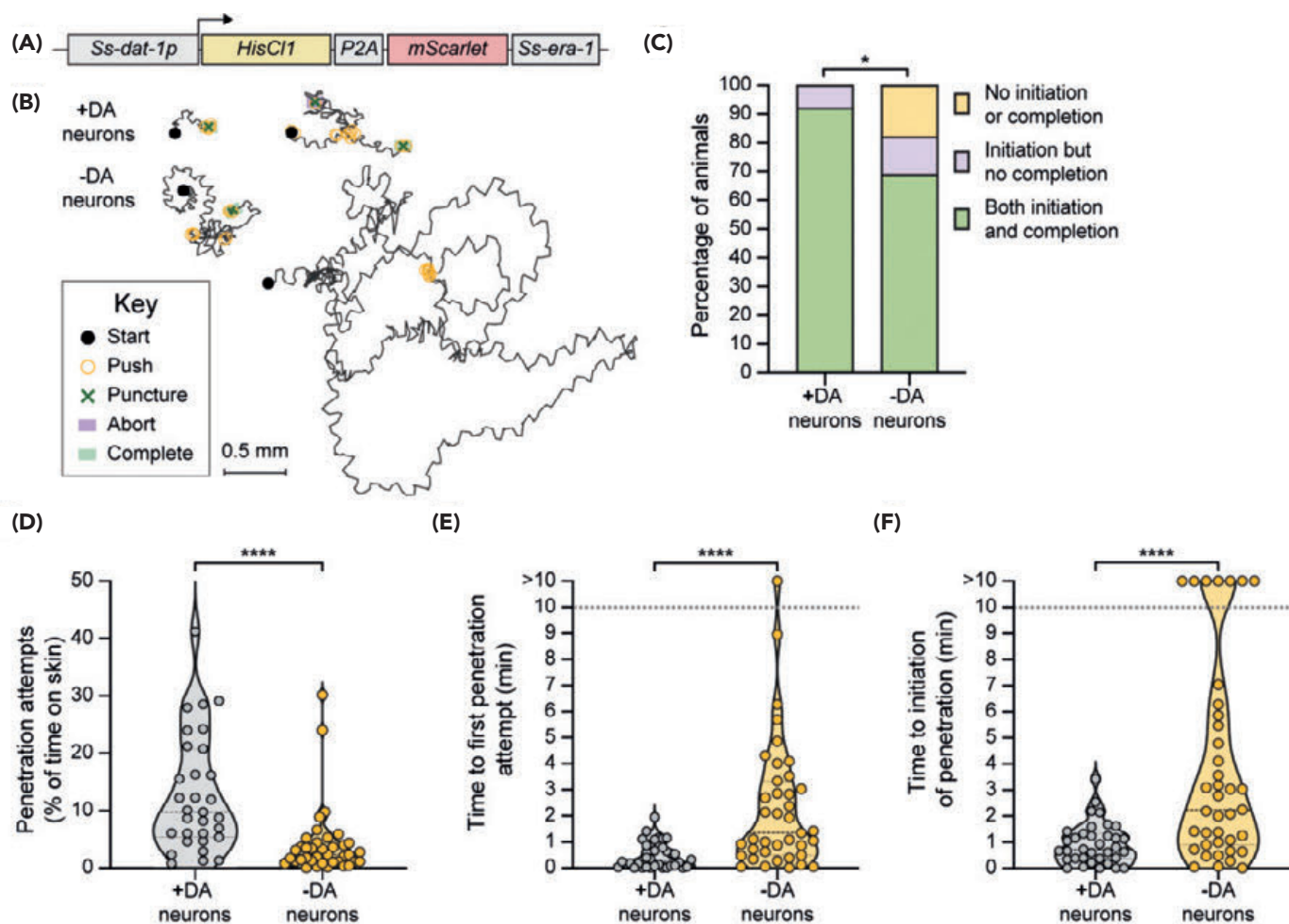


Figure 3: Silencing of the dopaminergic neurons delays or inhibits skin penetration.

(A) Schematic of the transgene used for chemogenetic silencing of the dopaminergic (DA) neurons of *S. stercoralis*. **(B)** Tracks show the behaviors of two representative mock-treated (+DA neurons, top two tracks) or histamine-treated (-DA neurons, bottom two tracks) iL3s on rat skin. **(C)** Bar graph shows the percentage of mock-treated (+DA neurons) and histamine-treated (-DA neurons) iL3s that either initiated and completed skin penetration, initiated but did not complete skin penetration, or neither initiated nor completed skin penetration. **(D)** Violin plot depicts the percentage of time on skin that mock-treated (+DA neurons) and histamine-treated (-DA neurons) iL3s spent attempting skin penetration. **(E)** Violin plot depicts the time taken by mock-treated (+DA neurons) and histamine-treated (-DA neurons) iL3s to attempt penetration for the first time following placement on skin. **(F)** Violin plot depicts the time taken by mock-treated (+DA neurons) and histamine-treated (-DA neurons) iL3s to initiate penetration. For D-F, dots depict individual worms, dashed lines indicate the median, and dotted lines indicate the interquartile range. In D-F, the dotted line at $y = 10$ indicates the time at which the assay ended.

consecutive days with a 1 to 2-week gap in between each round. This concentration has been previously shown to produce effective neuronal silencing (12). *S. stercoralis* transgenic iL3s, which were identified based on the fluorescence signal of mScarlet, were isolated from the next generation and used in single-worm behavioral assays.

Skin Penetration Behavioral Assays

To observe the behaviors of skin penetration, an *ex vivo* skin penetration assay was used. Skin was obtained from 6 euthanized rats and then shaved and waxed to remove the fur. For the skinning process, an incision was made in the epidermis in the dorsal area of the rat, close to the neck reaching through to the hypodermis. The dorsal region was selected as it is not susceptible to puncturing other regions of the rat while making an incision. This incision was continuously cut underneath the

hypodermis around the rat until the skin could be peeled off and separated from underlying organs. The skin used was from the dorsal and lateral areas of the rat. Skin on the ventral surface was excluded as a precautionary measure to avoid potentially puncturing the intestines while skinning the region.

For the behavioral assays, a piece of skin, measuring 1 cm x 1 cm, was placed on top of a single CellCrown 12-well plastic insert. Both the skin and the insert were placed inside a single well of a 6-well plate filled with saline solution composed of 50 mM disodium phosphate, 22 mM monopotassium phosphate, and 70 mM sodium chloride dissolved in water. Using 2 mg/mL DiI, a fluorescent lipophilic dye, iL3s were stained for 15 minutes before placing them on the surface of the rat skin. The staining duration was selected based on prior observations and optimization; prolonged staining can lead to lethargic worms. Staining for under 15 minutes does not completely dye the iL3s. Lethargy is deduced

based on the mobility of the worm: a worm is considered lethargic if immobile on the surface of the skin. Together, the removal of fur and the staining of iL3s ensured that the worms were visible on the epidermal surface. For silencing neurons, a histamine solution was made by diluting 1 M histamine, previously dissolved in double-distilled water, in buffered saline to a final working concentration of 50 mM. Nematodes were imaged on the skin for a 10-minute period using a Basler ace (acA5472-17 μ m) camera at 4 frames per second. These settings were chosen to clearly visualize the worms under the microscope and video-capture the behaviors performed on the skin. The images were analyzed *post hoc* using Fiji version 2.9.0/1.53t. The position of worms was tracked manually using the Trackmate plugin in Fiji and the behaviors were scored by eye. The behaviors of 31–39 worms were tracked and analyzed over 6 different trials.

Statistical Analysis

A chi-squared test was used to determine if there was a significant difference in the distribution of larvae among the 3 stages—completed penetration, initiated but did not complete penetration, or did not initiate penetration—between the histamine-treated and control iL3s (Figure 3C). Mann-Whitney *U* tests were used to detect statistical differences between histamine-treated and control worms (Figure 3D–F). In all of these figures, * indicates a p-value of <0.05 and **** indicates a p-value of <0.0001. The test family was the t-test with the statistical test being the Wilcoxon-Mann-Whitney test. A priori power analysis using the G*Power 3.1 software was conducted to estimate the minimum sample size needed, considering a two-tailed test with a normal parent distribution. The effect size was set at 1.05, the alpha error at 0.05, the power at 0.08, and the allocation ratio at 1.

RESULTS

This study tested whether silencing the dopaminergic neurons of *S. stercoralis* altered behavior on rat skin using an *ex vivo* skin penetration assay. Figure 3 shows the schematic of the construct that was used for silencing the dopaminergic neurons. To determine whether silencing of the dopaminergic neurons affected skin penetration, skin penetration assays were done to compare the behaviors of transgenic iL3s treated either with or without histamine. *S. stercoralis* iL3s normally push down on the rat skin with their heads and make a penetration attempt by puncturing the skin (insert their heads into the skin) prior to penetration (full entry into the skin). Silencing the dopaminergic neurons inhibited skin-penetration behavior, with differences in pushing and puncturing between the two groups of worms (Figure 3B). Exactly 18% of the iL3 with silenced dopaminergic neurons did not initiate penetration, as compared with 0% of the control iL3s (Figure 3C). The iL3s with silenced dopaminergic neurons spent $2.33 \pm 30.22\%$ (median \pm interquartile range) of the time on the skin surface attempting penetration; this metric was 9.76 ± 40.53 (median \pm interquartile range) for control iL3s (Figure 3D). On average, the first penetration attempt of iL3s with silenced dopaminergic neurons was about 5-fold later than control iL3s (Figure 3E). Similarly, the time to initiation of penetration in iL3s with silenced dopaminergic neurons differed by about 3-fold relative to control iL3s (Figure 3F). Collectively, this data shows that the dopaminergic neurons play a crucial role in regulating the decision of iL3s to penetrate host skin.

DISCUSSION

The results from this study indicate that skin-penetration behaviors are modulated in part by dopamine signaling. Specifically, chemogenetically silencing the dopaminergic neurons impairs the ability of iL3s to penetrate host skin (Figure 3C–D). In addition, the data suggest that dopaminergic neurons modulate both the time to the first penetration attempt and the initiation of penetration (Figures 3E–F). When dopaminergic neurons are silenced, iL3s may not be able to sense the texture of the skin surface, which could cause them to fail to initiate skin-penetration behaviors despite being on host skin conducive to penetration (6).

One limitation of this study is that the histamine treatment itself might be causing a delay in skin penetration. To exclude this possibility, future skin penetration assays with non-transgenic nematodes that are treated with histamine will be conducted. The behavior of these worms will be compared with that of the transgenic worms treated with histamine.

The dopaminergic neurons may be modulating skin penetration by releasing either the neurotransmitter dopamine or unknown neuropeptides. Therefore, as a future direction, a model whereby the dopaminergic neurons in *S. stercoralis* sense the texture of the skin surface and release dopamine that communicates with downstream dopamine receptors to drive the initiation of skin penetration can be used to further examine the role of the DA neurons in skin penetration. To test this model, a Clustered Regularly Interspaced Short Palindromic Repeats (CRISPR) approach will be used to inactivate the *cat-2* gene to determine the extent to which the dopaminergic neurons of *S. stercoralis* modulate skin penetration in a future study. CRISPR/Cas9-mediated targeted gene disruptions have been successfully achieved in *S. stercoralis* (13). CRISPR/Cas-9 mediated inactivation of *cat-2*, an enzyme that is essential for dopamine biosynthesis (14), followed by skin penetration assays would help distinguish these possibilities. CRISPR will also be used to inactivate the *trp-4* gene, which encodes the pore-forming subunit of mechanotransduction channels (15), to elucidate the mechanoreceptor(s) in neurons that might sense skin texture and promote skin-penetration behaviors. As a long-term future direction, calcium imaging will be used to better explore and understand how the dopaminergic neurons drive skin penetration. Using these approaches, the underlying goal of the CRISPR/Cas9 and calcium imaging approach is to explore whether the dopaminergic neurons sense skin texture to promote skin-penetration behaviors.

Previous studies have not evaluated the mechanisms that drive the process of skin penetration (16). This study elucidates the understanding of parasitic behaviors on host skin and the mechanisms that underlie these behaviors; this is essential to identify new strategies to prevent infection by skin-penetrating parasitic nematodes. For example, the identification of mechanoreceptors that drive skin penetration would enable the design of drugs that target these receptors. These drugs could be applied in the form of topical creams that prevent skin penetration by *S. stercoralis* and thereby prevent infection (17).

ACKNOWLEDGEMENTS

This work is funded in part by a National Institutes of Health (NIH) / National Institute of General Medical Sciences training grant NIH MARC T34GM008563 to A.G.R., National Institutes

of Health / National Institute of Allergy and Infectious Diseases NIAID F32AI174816 to R.P., and National Institutes of Health / National Institute of Allergy and Infectious Diseases R01AI175183 to E.A.H. The authors declare that they have no conflict of interest.

EDITORS

This article was reviewed by Agamroop Kaur, Ryan Wong, Saanika Joshi, Viraj Nigam, Wasila Sun; edited by Chahak Gupta, Charlotte Chen, Chloe Nelson-Torakawa; and laid out by Christy Ma.

REFERENCES

1. M. Riaz *et al.*, Prevalence, risk factors, challenges, and the currently available diagnostic tools for the determination of helminths infections in human. *Eur. J. Inflam.*, **18**, (2020). doi: 10.1177/2058739220959915.
2. D. Buonfrate *et al.*, The Global Prevalence of *Strongyloides stercoralis* Infection. *Pathogens* (Basel, Switzerland), **9**(6), 468. (2020). doi: 10.3390/pathogens9060468.
3. S. M. Thamsborg, J. Ketzis, Y. Horii, J. B. Mathews, *Strongyloides* spp. infections of veterinary importance. *Parasitology*, **144**(3), 274–284. (2017). doi: 10.1017/S0031182016001116.
4. J. B. Lok, *Strongyloides stercoralis*: A model for translational research on parasitic nematode biology. In WormBook: The Online Review of *C. elegans* Biology [Internet]. WormBook. (2007). <https://www.ncbi.nlm.nih.gov/books/NBK19663/>.
5. T. Hills, P. J. Brockie, A. V. Maricq, Dopamine and Glutamate Control Area-Restricted Search Behavior in *Caenorhabditis elegans*. *J. Neurosci.*, **24**(5), 1217–1225. (2004). doi: 10.1523/JNEUROSCI.1569-03.2004.
6. B. Han *et al.*, Dopamine signaling tunes spatial pattern selectivity in *C. elegans*. *ELife*, **6**, e22896. (2017). doi: 10.7554/eLife.22896.
7. D. L. Chase, M. R. Koelle, Biogenic amine neurotransmitters in *C. elegans*. WormBook. (2007). doi: 10.1895/wormbook.1.132.1.
8. L. Carvelli, R. D. Blakely, L. J. DeFelice, Dopamine transporter/syntaxin 1A interactions regulate transporter channel activity and dopaminergic synaptic transmission. *PNAS*, **105**(37), 14192–14197. (2008). doi: 10.1073/pnas.0802214105.
9. A. Fok *et al.*, High-fidelity encoding of mechanostimuli by tactile food-sensing neurons requires an ensemble of ion channels. *Cell Reports*, **42**, 112452 (2023). doi: 10.1016/j.celrep.2023.112452.
10. M. B. Goodman, P. Sengupta, How *Caenorhabditis elegans* Senses Mechanical Stress, Temperature, and Other Physical Stimuli. *Genetics*, **212**, 25–51 (2019). doi: 10.1534/genetics.118.300241.
11. N. Pokala, Q. Liu, A. Gordus, C. I. Bargmann, Inducible and titratable silencing of *Caenorhabditis elegans* neurons in vivo with histamine-gated chloride channels. *PNAS*, **111**(7), 2770–2775. (2014). doi: 10.1073/pnas.1400615111.
12. A. S. Bryant, F. Ruiz, J. Ha Lee, E. A. Hallem, The neural basis of heat seeking in a human-infective parasitic worm. *Curr Biol*, **32**(10), 2206–2221.e6. (2022). doi: 10.1016/j.cub.2022.04.010.
13. P. Mendez, B. Walsh, E. A. Hallem, Using newly optimized genetic tools to probe *Strongyloides* sensory behaviors. *Mol Biochem Parasitol*, **250**, 111491. (2022). doi: 10.1016/j.molbiopara.2022.111491.
14. R. Lints, S. W. Emmons. Patterning of dopaminergic neurotransmitter identity among *Caenorhabditis elegans* ray sensory neurons by a TGF β family signaling pathway and a Hox gene. *Development (Cambridge, England)*, **126**(24), 5819–5831. (1999). doi: 10.1242/dev.126.24.5819.
15. L. Kang, J. Gao, W. R. Schafer, Zhixiong Xie, X. Z. Shawn Zu, *C. elegans* TRP family protein TRP-4 is a pore-forming subunit of a native mechanotransduction channel. *Neuron*, **67**(3), 381–391. (2010). doi: /10.1016/j.neuron.2010.06.032.
16. J. H. McKerrow *et al.*, *Strongyloides stercoralis*: identification of a protease that facilitates penetration of skin by the infective larvae. *Exp Parasitol*, **70**(2), 134–143. (1990). doi: 10.1016/0014-4894(90)90094-s.
17. C. R. McClure, R. Patel, E. A. Hallem, Invade or die: behaviours and biochemical mechanisms that drive skin penetration in *Strongyloides* and other skin-penetrating nematodes. *Philos Trans R Soc Lond B Biol Sci*, **379**(1894), 20220434. (2024). doi: 10.1098/rstb.2022.0434.

2023-2024 USJ STAFF

LEADERSHIP



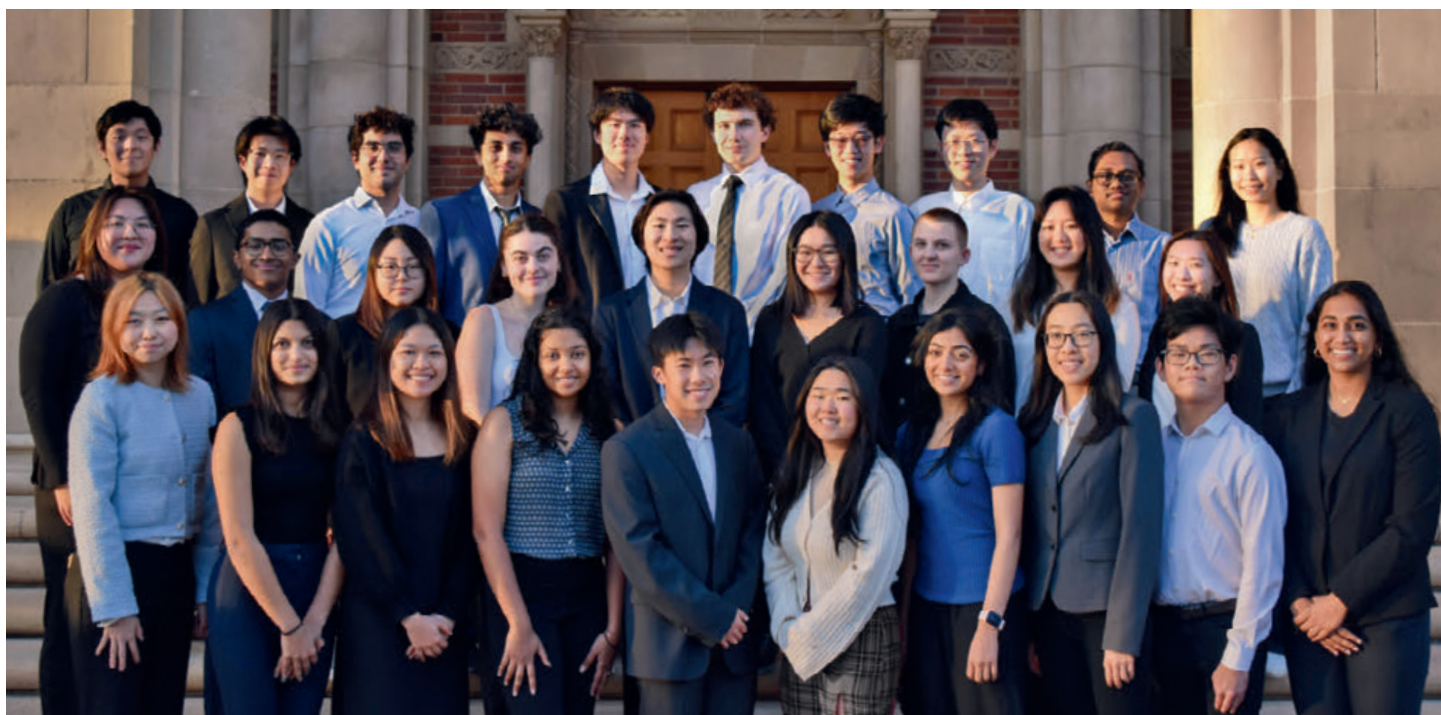
(From left to right) Top row: Ahmad Ismail, Emily Lin, Sohan Talluri. Second row: Dashrit Pandher, Elise Tran, Caroline Sha.

ASST. EDITORS



(From left to right) Top row: Brendan Sam, Jordan Lin, Timothy Liu. Second row: Malvika Iyer, Nyah Zhang, Chelsea Lai, Rachel Ma. Third row: Raphael Low, Ying yin (Lina) Zhu, Isabel Angres. Fourth row: Melody Jiang, Nhi Pham.

REVIEW BOARD



(From left to right) Top row: Jordan Lin, Ryan Wong, Issac Ramos Reina, Daniel Bielin, Viraj Nigam, David Mastro, Oliver Wang, Yiming Li, Sai Charan Petchetti, Rachel Ma. Second row: Nyah Zhang, Nathan Joshua, Joanna Rhim, Cecilia McCormick, Ethan Hung, Zoe Yeh, Eliana Bohn, Marissa Li, Melody Jiang. Third row: Caroline Sha, Raina Bandekar, Joyce Goh, Mahek Shah, Caden Chow, Jessica Goeji, Saanika Joshi, Wasila Sun, Raphael Low, Malvika Iyer. Not pictured: Agamroop Kaur, Archi Patel, Miki Mat-suoka, Summer Kelso.

EDITORIAL BOARD



(From left to right) Top row: Sohan Talluri, Brynn Beatty, Andrew Wang, Aniket Das, Zachary Lamm, Derek Ren, Kyle Nguyen-Ngo, Lily Zello. Second row: Brendan Sam, Charlotte Chen, Vivasvaan Aditya Raj, Lee Zucker-Murray, Marie Yang, Paul Zhang, Satviki Chaturvedi, Timothy Liu. Third row: Isabel Angres, Gia Boisselier, Ruthy Shin, Chloe Nelson-Torakawa, Tanisha Lakhanpal, Siddhika Naik, Ying yin (Lina) Zhu, Nhi Pham. Not pictured: Chahak Gupta.

LAYOUT BOARD



(From left to right) Top row: Ahmad Ismail, Chelsea Lai, and Dashrit Pandher. Bottom row: Zenya Bian, Danny Zhu, Christy Ma, and Truman Ma.



(From left to right) Top row: Dashrit Pandher, Sohan Talluri, Daniel Bielin, Yiming Li, Viraj Nigam, Andrew Wang, Aniket Das, Zachary Lamm, Derek Ren, David Mastro, Oliver Wang, Jordan Lin, Ahmad Ismail. Second row: Sai Charan Petchetti, Nyah Zhang, Danny Zhu, Issac Ramos Reina, Brynn Beatty, Kyle Nguyen-Ngo, Lily Zello, Ryan Wong, Truman Ma, Zenya Bian, Rachel Ma, Eliana Bohn, Marissa Li. Third row: Elise Tran, Joanna Rhim, Brendan Sam, Charlotte Chen, Vivasvaan Aditya Raj, Lee Zucker-Murray, Marie Yang, Paul Zhang, Satviki Chaturvedi, Timothy Liu, Ethan Hung, Cecilia McCormick. Fourth row: Joyce Goh, Nathan Joshua, Raina Bandekar, Isabel Angres, Gia Bois-selier, Ruthy Shin, Malvika Iyer, Wasila Sun, Zoe Yeh, Chelsea Lai, Caroline Sha, Dr. Jorge Avila. Fifth row: Christy Ma, Mahek Shah, Melody Jiang, Chloe Nelson-Torakawa, Tanisha Lakhanpal, Jessica Goeji, Siddhika Naik, Ying yin (Lina) Zhu, Nhi Pham, Caden Chow, Saanika Joshi, Raphael Low.

The UCLA Undergraduate Science Journal is a peer-reviewed publication registered with the Library of Congress, featuring top-quality research performed by undergraduates in all STEM fields, including life sciences, engineering, statistics, physics, mathematics, computer science, and more. We aim to provide a multidisciplinary platform that allows students to publish their research and engage with the larger research community at UCLA and also involves students with the peer review process. Submitted manuscripts undergo a rigorous review and publication process run completely by undergraduates.

USJ accepts manuscript submissions and staff applications annually in the fall.

Correspondence should be addressed to Dr. Jorge A. Avila, Life Sciences 2121, 621 Charles E. Young Dr. S. Los Angeles, CA 90095 or the UCLA Undergraduate Science Journal at usj@ucla.edu.

We acknowledge the generous support of the Undergraduate Research Center – Sciences and of the UCLA Clinical and Translational Science Institute (CTSI) grant UL1TR001881 to publish this journal.



